University of Alberta

Calorimeter Optimization and Heavy Higgs Reconstruction in ATLAS

By

Dugan Clive O'Neil ©

A thesis

submitted to the Faculty of Graduate Studies and Research

in partial fulfilment of the requirements for the degree of Master of Science

Department of Physics

Edmonton, Alberta

Fall 1996

National Library of Canada

Acquisitions and Bibliographic Services Branch

395 Wellington Street
Ottawa, Ontario
K1A 0N4

Bibliothèque nationale du Canada

Direction des acquisitions et des services bibliographiques

395, rue Wellington
Ottawa (Ontario)
K1A 0N4

Your file Votre référence

Our file Notre référence

The author has granted an irrevocable non-exclusive licence allowing the National Library of Canada to reproduce, loan, distribute or sell copies of his/her thesis by any means and in any form or format, making this thesis available to interested persons.

L'auteur a accordé une licence irrévocable et non exclusive permettant à la Bibliothèque nationale du Canada de reproduire, prêter, distribuer ou vendre des copies de sa thèse de quelque manière et sous quelque forme que ce soit pour mettre des exemplaires de cette thèse à la disposition des personnes intéressées.

The author retains ownership of the copyright in his/her thesis. Neither the thesis nor substantial extracts from it may be printed or otherwise reproduced without his/her permission.

L'auteur conserve la propriété du droit d'auteur qui protège sa thèse. Ni la thèse ni des extraits substantiels de celle-ci ne doivent être imprimés ou autrement reproduits sans son autorisation.

ISBN 0-612-18306-8

Canada

UNIVERSITY OF ALBERTA
LIBRARY RELEASE FORM

NAME OF AUTHOR: Dugan Clive O'Neil

TITLE OF THESIS: Calorimeter Optimization and Heavy Higgs Reconstruction in ATLAS

DEGREE: Master of Science

YEAR THE DEGREE GRANTED: 1996

Permission is hereby granted to the University of Alberta library to reproduce single copies of this thesis and to lend or sell such copies for private, scholarly or scientific research purposes only.

The author reserves all other publication and other rights in association with the copyright in this thesis, and except as hereinbefore provided, neither the thesis nor any substantial portion therof may be printed or otherwise reproduced in any material form whatever without the author's prior written permission.

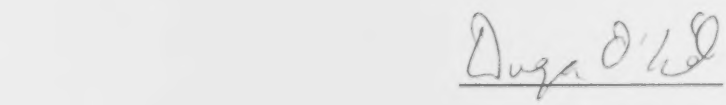

Dugan Clive O'Neil
Department of Physics
University of Alberta
Edmonton, Alberta
T6G 2J1

Sept 3/96

UNIVERSITY OF ALBERTA

FACULTY OF GRADUATE STUDIES AND RESEARCH

The undersigned certify that they have read, and recommend to the Faculty of Graduate Studies and Research for acceptance, a thesis entitled "Calorimeter Optimization and Heavy Higgs Reconstruction in ATLAS " submitted by Dugan Clive O'Neil in partial fulfilment of the requirements for the degree of Master of Science

Associate Professor J.L. Pinfold , Supervisor

Assistant Professor D.M. Gingrich

Associate Professor M. Freeman

Professor W.W. Armstrong

Aug. 28/96

Abstract

ATLAS (A Toroidal LHC ApparatuS) is a general purpose experiment to be built for the LHC (Large Hadron Collider) in CERN, Geneva. This thesis examines, in detail, two aspects of calorimeter simulation for ATLAS. These two aspects are the optimization of the calorimeter design for the detection of jets in the presence of pile-up and the development of analysis techniques to recognize and reconstruct jets in simulated heavy Higgs events. Results are presented for simulations using the technical proposal version of the ATLAS end-cap geometry. Design changes are introduced and tested in this geometry and the effect of these changes on energy resolution is measured. Next, a detailed comparison of two jet finding techniques is presented. Each of these techniques are new to ATLAS analysis and are presented in the context of a heavy (600 GeV/c^2) Higgs boson search.

Acknowledgements

I would like to acknowledge my supervisor, Dr. Jim Pinfold for guiding my research at U of A and the staff of the Centre for Subatomic Research for their support in this work.

I would also like to thank Rob Davis and Pierre Savard for their help and collaboration in the jet simulation work contained here.

Thanks to Alick Macpherson for his thorough proofreading of this thesis and for being an excellent collaborator in the heavy Higgs section of this thesis.

I would like to acknowledge the crew in P146 → Philip "Cold-Coke" Kayal, Anthony "my salmon are bigger" Faust, Alick "cluster-boy" Macpherson, Bryan "the intimidator" Caron, Rob "Sys-Op" Davis and Trevor "Stair-Master" Nickle for making U of A a fun place to work.

Finally, I would like to thank my wife Melanie for accepting the position of "physics widow" for the last few months as I finished this thesis.

Contents

1 Introduction 1

1.1 The Standard Model 2

1.2 Spontaneous Symmetry Breaking 6

1.3 The Higgs Mechanism 8

1.4 LHC 11

1.4.1 Physics Interests 11

1.4.2 Design 14

1.5 ATLAS 17

2 The Design of ATLAS 22

2.1 Calorimetry, Jets and Energy Resolution 23

2.2 Inner Detector 26

2.3 Muon System 28

2.4 EM Calorimetry 30

2.5 Hadronic Calorimetry 32

2.5.1 Barrel 33

2.5.2 End-Cap 34

2.6 Forward Calorimetry 39

2.7 Trigger and DAQ 41

3 End-Cap Simulation and Optimization **43**

3.1 Introduction 43

3.2 ATLAS Software 44

3.3 Effects of Pile-up with Different End-Cap Configurations 46

3.3.1 What is Pile-up? 47

3.3.2 Calibration 50

3.3.3 Reconstruction 52

3.3.4 Results 54

3.3.5 Conclusions 55

3.4 Study of Changing Granularities in the Hadronic End-Cap 60

3.4.1 Introduction 60

3.4.2 Results 61

3.4.3 Conclusions 67

3.5 Study of Plate Thickness Changes in the Presence of Pile-up 72

3.5.1 Introduction 72

3.5.2 Results 73

3.5.3 Conclusions 79

3.6 Conclusions - End-Cap Simulation and Optimization 79

4 The Search for the Heavy Higgs Boson **80**

4.1 Introduction 80

4.2 Jet Finding 83

4.2.1 Cones 84

4.2.2 K_T Clustering 85

4.3 Muon Reconstruction 87

4.4 The Monte Carlo Production 90

4.4.1 Filter Selection Study 90

4.4.2 The Full-Simulation Production 97

4.5 Results - Full Simulation Reconstruction 100

4.5.1 Reconstruction of Higgs Using Profile Analysis 100

4.5.2 Reconstruction of Higgs Using K_T Clustering Analysis 105

4.5.3 Conclusions - Full Simulation Reconstruction 108

4.6 Results - Particle Level 111

4.6.1 Profile Analysis, Including Effects of Energy Resolution 114

4.6.2 K_T Clustering Analysis, Including Effects of Energy Resolution . 121

5 General Conclusions **129**

Bibliography **131**

A Jet Simulation Study **135**

A.1 abstract 137

A.2 Introduction 138

A.3 Generation of the Data Sample 139

A.4 Jet Reconstruction and Calibration Procedure 142

A.5 Energy Resolution Results 144

A.5.1 Exterior Contributions to the Energy Resolution 144

A.5.2 Jet Energy Resolution of the Endcap Calorimeter 149

A.5.3 Behaviour of the Calibration Constants 154

A.5.4 Investigation of Hadronic Code Differences 157

A.6 Energy Resolution of Jets in the Presence of Pileup Noise 163

A.6.1 Pileup Inclusion Method 164

A.6.2 Energy Resolution in the Presence of Pileup Noise 165

A.6.3 Jet Scale in the Presence of Pileup Noise 170

A.7 Discussion 173

A.8 Conclusions 177

List of Tables

1.1 Fermions of the Standard Model 5

1.2 LHC parameters 16

1.3 ATLAS radiation table 21

3.1 PYTHIA mbias processes 48

3.2 Example end-cap calibration constants 53

3.3 Z-dependent energy cut in the end-cap 62

4.1 Jet Definitions. 100

4.2 Jet-Jet profile results 106

4.3 K_T clustering results 110

4.4 Particle level jet-jet profile results, no smearing 116

4.5 Particle level jet-jet profile results, 50% smearing 117

4.6 Particle level jet-jet profile results, 150% smearing 118

4.7 Particle level K_T clustering results, no smearing 123

4.8 Particle level K_T clustering results, 50% smearing 124

4.9 Particle level K_T clustering results, 150% smearing 125

A.1 Minimum bias data cards 140

A.2 Sampling and constant terms measured by fitting the energy resolution of jets in the whole endcap calorimeter with a two term equation in this note and CAL-083. 151

A.3 A comparison of the energy resolution results for 40 GeV E_T jets centered at $\eta = 2.3$ reconstructed in the whole endcap calorimeter volume for two different sets of GEANT cuts. The cuts are described in the text. 154

List of Figures

1.1 Potentials for spontaneous Symmetry Breaking 7

1.2 Feynman diagrams for Higgs production at the LHC 12

1.3 Cross-sections of many interesting physics processes at the LHC. 13

1.4 The injector complex and the LHC ring 14

1.5 Cross-section of an LHC dipole magnet 15

1.6 The distribution of detectors around the LHC ring 18

1.7 The proposed ATLAS detector 19

2.1 Layout of the ATLAS inner detector 27

2.2 The ATLAS Muon Spectrometer (radius is approximately 11 metres). . 29

2.3 Scheme of an absorber plate 31

2.4 An EM shower in an accordion calorimeter 31

2.5 Principle of the tile hadronic calorimeter 35

2.6 Cross-sections of the hadronic end-cap 36

2.7 Position of the hadronic end-cap in ATLAS 37

2.8 Detailed structure of the readout cell 38

2.9 Front face of the EM FCAL module 40

2.10 Design of the ATLAS trigger system 41

3.1 Software flow diagram 45

3.2 A shaping function 49

3.3 Signal and shaped pile-up 51

3.4 Energy resolution with pile-up, 1 div 56

3.5 Energy resolution, different configs. 57

3.6 Energy resolution, different configs., E_T cut 58

3.7 Energy resolution, 5 configs. 59

3.8 Energy resolution, different granularities 63

3.9 Energy resolution, granularities, 0 GeV E_T cut 64

3.10 Energy resolution, granularities, 1.5 GeV E_T cut 65

3.11 Energy resolution, granularities, combined plot 66

3.12 Energy resolution, granularities, no E_T cut 68

3.13 Energy resolution, granularities, 0 GeV E_T cut 69

3.14 Energy resolution, granularities, 1.5 GeV E_T cut 70

3.15 Energy resolution, granularities, combined plot 71

3.16 Thin/Thick plate comparison 74

3.17 Results from CAL-NO-083 75

3.18 Energy resolution, thicknesses,no cuts 76

3.19 Energy resolution, granularities, 0 GeV E_T cut 77

3.20 Energy resolution, granularities, Z-dep.E_T cut 78

4.1 Feynman diagrams of $qq \rightarrow qqZZ$ 82

4.2 Z reconstruction from muons 89

4.3 P_T of Z from Higgs 92

4.4 P_T distribution of Z from Z + jets 93

4.5 η distributions of forward tag quarks from $qq \rightarrow Hqq \rightarrow ZZqq$ signal . . 95

4.6 η distributions of quark or gluon jet candidates from Z + jets background 96

4.7 P_T distributions of forward jet candidates from signal events 98

4.8 P_T distributions of forward jet candidates from background events 99

4.9 Diagram of jet-jet pair 101

4.10 Profile Z, Higgs invariant mass 104

4.11 Invariant mass of Z and Higgs particles as reconstructed from two jets using K_T clustering technique. 109

4.12 Full simulation vs. particle-level Z reconstruction 113

4.13 Efficiency of profile analysis vs. energy resolution 119

4.14 Z mass reconstruction vs. resolution 120

4.15 Performance vs. Higgs mass 122

4.16 Efficiency of clustering analysis vs. energy resolution 127

4.17 Z mass reconstruction vs. resolution, K_T clustering 128

A.1 Hadronic end-cap cross-section 141

A.2 Energy lost in inner tracking 147

A.3 Contribution of energy loss in tracking to resolution 148

A.4 Resolution of jets with identical initial particle content 150

A.5 Resolution comparison of GCALOR and G-FLUKA 152

A.6 Energy resolution curves for dijets reconstructed in three different cone sizes using GEANT-FLUKA (top) and GCALOR (bottom). 153

A.7 Calibration constants versus jet energy 155

A.8 Calibration constants versus cone size 156

A.9 Spectra of $E^{true} - E^{recon}$ for 80 GeV E_T jets using the whole endcap calorimeter and three different cone sizes. The value for E^{true} used was taken to be the vertex energy directed within the same cone size that was used in the reconstruction. 158

A.10 Spectra of $E^{true} - E^{recon}$ for 80 GeV E_T jets using the whole endcap calorimeter and three different cone sizes. The value for E^{true} used was taken to be the vertex energy directed within a cone of size $\Delta R = 0.7$ for all reconstruction cone sizes. 159

A.11 Energy in tails of distribution 160

A.12 Energy resolution for pions in the endcap calorimeter using Gheisha (circles), GCALOR (squares), and GEANT-FLUKA (triangles). 161

A.13 e/π ratios for the endcap calorimeter using Gheisha (circles), GCALOR (squares), and GEANT-FLUKA (triangles). 162

A.14 High luminosity pileup, 2 GeV E_T integrated cut 166

A.15 High luminosity pileup, two different cuts 167

A.16 Resolution vs. size of integrated layer cut 168

A.17 Low luminosity pileup 169

A.18 Resolution for different granularities 171

A.19 Spectra of $E^{true} - E^{recon}$ in a ΔR= 0.5 cone for 40 GeV E_T (201.5 GeV) jets combined with high luminosity pileup. The spectra after several different values of transverse energy tower cuts are shown. 172

A.20 Jet scale factor, with high luminosity pileup 174

A.21 Jet scale factor for several cone sizes 175

CHAPTER 1

Introduction

When judging the performance of a detector that has yet to be built, two important and distinct types of tests must be performed at the simulation level. The first type establishes that the detector can satisfy the primary performance requirements assigned to it under a simulation of experimental conditions. In the case of calorimetry, such requirements demand that particle showers and jets of particles be detected with an acceptable energy resolution. The second type of testing is more specific and involves the simulation and reconstruction of physics signals the device was designed to detect. This thesis studies aspects of both of these detector design requirements and, in the process, attempts to make an orderly progression from the optimization of detector components to the use of those components to reconstruct an interesting physics signal.

In order that the reader is familiar with the background material necessary for this work, a general introduction to several particle physics issues is given. The first area discussed is the Standard Model of particle physics, and specific attention is given to spontaneous symmetry breaking and the Higgs mechanism. Next, brief descriptions of the Large Hadron Collider and the ATLAS detector are given in order to provide the setting in which the results presented here may eventually be applied.

The second chapter is devoted to a detailed description of the layout of the ATLAS detector. Particular emphasis is placed on hadronic calorimetry, an essential part of the research presented in later sections.

Once the layout of the ATLAS detector has been thoroughly described, the third chapter presents results of three different simulation studies performed to test the first of the detector design requirements; namely to ensure that the detector meets its primary design requirements. Specifically, this chapter is designed to thoroughly explore the performance and design of the ATLAS end-cap calorimeter. Simulations were performed using the ATLAS technical proposal end-cap geometry and include the effects of pile-up, an important concern in the end-cap region.

After the first aspect of detector design has been tested and the adequate performance of its primary tasks has been verified, it is desirable to test the second aspect of its design with a simulation of an interesting physics signal. The fourth chapter presents the results of a heavy Higgs reconstruction in a fully simulated ATLAS detector. These results are compared with particle level results for two different jet finding techniques, neither of which have been in use in previous ATLAS efforts. A full description of each of these techniques is provided in this chapter.

Finally, the fifth chapter summarizes the conclusions of the work performed here and discusses its relevance to ATLAS physics issues.

1.1 The Standard Model

The Standard Model of particle physics is the most successful model of the fundamental particles and their interactions yet developed. The success of this model is due to its attempt to reveal the relationship between matter and forces in terms of particles and underlying symmetry [1].

The current Standard Model is built on the successes of three previous theories. The first is Quantum Electrodynamics (QED), the theory which describes the

electromagnetic (EM) interaction with great accuracy and precision. The success of QED has led to its use as a model for the theories that have followed. The next theory in the Standard Model progression is the theory of electroweak interactions first proposed by Glashow, Weinberg and Salam in the late 1960's and referred to as the Glashow-Weinberg-Salam model [2] [3] [4]. This model incorporates the successful model of QED and provides a description of the weak force in terms of the exchange of massive vector bosons [5]. The fact that the masses of these vector bosons were successfully predicted from the theory before the particles were discovered is considered one of the major triumphs of the model. In the Standard Model, masses of these bosons are generated by the Higgs mechanism, the verification of which is one of the central themes in this thesis. The third theory which makes up the Standard Model is Quantum Chromodynamics (QCD). This is the quantum field theory describing the interactions of quarks through the strong "colour" field [5].

The fact that the Standard Model is made up from three gauge theories means that it is built up from three gauge symmetries. These symmetries correspond to the three fundamental forces relevant to particle physics, namely the strong, the weak, and the electromagnetic force. The Standard Model gauge group is the product group $SU(3) \times SU(2) \times U(1)$, with the $SU(3)$, $SU(2)$, and $U(1)$ component groups being associated with the colour, weak, and hypercharge symmetries. The corresponding gauge bosons are the massless gluons of QCD, the massive W^+,W^- and Z of the weak interaction, and the massless photon of electromagnetism.

The spin - 1/2, or fermion, content of the model is divided into two parts, both of which appear to come in three families. The two parts which make up the fermion content of the model are known as the quarks and the leptons. Leptons are fermions that interact under the weak, but not the strong interactions, while the quarks are fermions that interact under the strong and electroweak interactions [6].

The observed fermion content of the model (leptons and quarks) is listed below in Table 1.1.

The predictions of the Standard Model have been tested and verified to unprecedented precision by experiments at the Large Electron Positron Collider (LEP) [7], SLAC and many other laboratories. However, there are several incomplete aspects of the Standard Model, such as: the origin of mass is unverified, the interactions are not unified, an explanation for why there are only three families does not exist; there are many (19) free parameters in the model* [8]; gravitation is absent from the model; the mass scale is not "natural" (ie. radiative corrections to the Higgs mass suffer from large divergences requiring two quantities of order $\sim 10^{32}$ almost cancel to produce a result of 10^4, this fortuitous cancellation is considered "unnatural" [8] [10].) ; and it provides no dark matter candidate. These incomplete aspects of the model imply that the Standard Model is only an effective theory. That is, the Standard Model is a low energy approximation to an underlying theory.

One of the most important unanswered questions of the model is the origin of mass. It is widely believed that this question can be answered by invoking the Higgs mechanism which requires the onset of spontaneous symmetry breaking of the local gauge symmetry, and provides a mass generation mechanism for both of the SU(2) weak gauge bosons and the observed massive quarks and leptons. It also predicts the existence of a massive scalar particle known as the Higgs boson. The best experimental verification of the existence of the Higgs Mechanism would be the discovery of its physically detectable manifestation, the Higgs boson. Understandably, the discovery of this particle is perhaps the single most important quest in particle physics today.

*There are 19 parameters if ν's are massless, they are: 3 coupling constants, 2 parameters of the Higgs potential, 9 fermion masses, 3 mixing angles and 1 phase in the Kobayashi-Maskawa matrix, and the vacuum parameter of QCD

	MASS (GeV/c^2)	Q	Family	Hypercharge
QUARKS				
d	0.008	-1/3	1	1/3
u	0.004	+2/3	1	1/3
s	0.15	-1/3	2	4/3
c	1.2	+2/3	2	1/3
b	4.7	-1/3	3	1/3
t	170	+2/3	3	1/3
LEPTONS				
e	0.0005	-1	1	0
ν_e	0	0	1	0
μ	0.105	-1	2	0
ν_μ	0	0	2	0
τ	1.8	-1	3	0
ν_τ	0	0	3	0

Table 1.1: The fermions of the Standard Model.

1.2 Spontaneous Symmetry Breaking

Spontaneous symmetry breaking occurs when the Lagrangian of a system retains its invariance under the symmetry group, but the vacuum state (ground state of the system) does not exhibit the same invariance - the symmetry is hidden, as the vacuum state breaks the symmetry [6]. To understand how this is achieved, we consider the case of a single complex scalar field, $\phi(x)$, and the $U(1)$ phase rotation invariant Lagrangian given by Equation 1.1,

$$L(\phi, \phi^\dagger, \partial_\mu\phi, \partial_\mu\phi^\dagger) = \partial_\mu\phi^\dagger\partial^\mu\phi - V(\phi^\dagger\phi) \tag{1.1}$$

with $V(\phi\phi^\dagger) = \mu^2|\phi|^2 + \Lambda|\phi|^4$. For this system, the Euler-Lagrange equation implies that the vacuum state must satisfy

$$\phi_0(\mu^2 + 2\Lambda|\phi_0|^2) = 0 \tag{1.2}$$

This condition offers two possibilities; either both μ^2 (mass^2) and Λ (coupling strength) are positive, or μ^2 is negative while Λ remains positive (Λ cannot be negative as the potential must be bounded below). The former case implies that there is only one solution, that of conventional vacuum with $\phi_0 = 0$, while the latter case permits a second solution;

$$|\phi_0|^2 = -\frac{\mu^2}{2\Lambda} \equiv \frac{v^2}{2} \qquad \phi_0 \equiv < \phi > \frac{1}{\sqrt{2}} v e^{i\zeta} \tag{1.3}$$

The second solution implies that the true vacuum corresponds to a non-zero vacuum expectation value (vev) for ϕ. The spontaneous symmetry breaking potential is the famous "Mexican Hat" potential, with the vev ($< \phi >$) being a circle of minima of radius $\frac{v}{\sqrt{2}}$ centred on the origin. Figure 1.1 shows a 2-D slice of the potential $V(\phi^\dagger\phi)$ for both solutions to the spontaneous symmetry breaking condition.

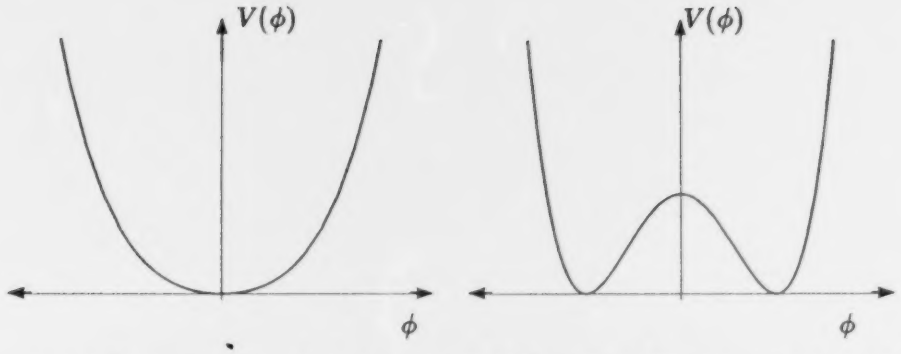

Figure 1.1: Two versions of the simple $U(1)$ invariant Higgs potentials: (a) The conventional vacuum Higgs potential with $< \phi >= 0$, (b) a 2-d slice of the spontaneous symmetry breaking Higgs potential with $< \phi > \neq 0$.

There is, however, a problem with the second solution to Equation 1.1. The problem is that the scalar field has an unphysical negative mass. However, this situation can be remedied by means of a field redefinition of ϕ, where ϕ is expanded around its vev. The form of this expansion is

$$\phi(x) = \frac{1}{\sqrt{2}}(\rho(x) + v)e^{i[\theta + \frac{\xi(x)}{v}]} \tag{1.4}$$

with $\rho(x)$ and $\xi(x)$ being real fields. In this expansion, the introduction of $\rho(x)$ takes into account oscillations about the Mexican Hat minimum at $x = v/\sqrt{2}$ while $\xi(x)$ parametrises motion around the minimum (ie. the minimum is really a flat circle). The effect of this field redefinition on the Lagrangian is to cause it to dramatically alter its form;

$$L = \frac{1}{2}\partial_\mu\rho\partial^\mu\rho + \frac{1}{2}\frac{(\rho+v)^2}{v^2}\partial_\mu\xi\partial^\mu\xi + \mu^2\rho^2 - \Lambda v\rho^3 - \frac{\Lambda}{4}\rho^4 - \frac{\mu^2 v^2}{4} \tag{1.5}$$

The justification for the field redefinition now becomes apparent. Equation 1.5 is the Lagrangian for two real scalar fields, one of which $(\rho(x))$ has a positive mass while

the other ($\xi(x)$) is massless. Both are physically acceptable fields. Further, this Lagrangian does not explicitly exhibit the original invariance under phase rotations (due to the expansion of ϕ around its vev), yet, by its very construction, the Lagrangian still possesses the underlying internal symmetry of the gauge group. Because of this, the symmetry has been spontaneously broken, and resulting in the appearance of a massless field (Nambu-Goldstone boson), which is free to move along the minima of the "Mexican Hat" potential.

1.3 The Higgs Mechanism

The exact mechanism by which the masses of the vector bosons and fermions of the Standard Model are generated remains unverified [10]. However, it is widely believed that the Higgs Mechanism is the key to explaining this mass generation.

The Higgs mechanism is the application of spontaneous symmetry breaking to a local gauge group. Again consider the complex scalar field, but this time require it to be invariant under local gauge transformation, as well as having the "Mexican Hat" potential. The Lagrangian of Equation 1.1 now becomes

$$L = \frac{-1}{4} F_{\mu\nu} F^{\mu\nu} + (D_\mu \phi)^\dagger D^\mu \phi - \mu^2 |\phi|^2 - \Lambda |\phi|^4 \tag{1.6}$$

where $F_{\mu\nu}$ is the field strength and the covariant derivative, D_μ, is given by

$$D_\mu \phi_i(x) = [\partial_\mu + igQ_i A_\mu(x)]\phi_i(x) \tag{1.7}$$

As before, we can expand ϕ around its vacuum expectation value in order to recover the physical scalar fields, but the expansion is a little more complicated due to local nature of the required gauge invariance. In this case, the second term of the Lagragian

presented in Equation 1.6 becomes

$$\begin{aligned}(D_\mu\phi)^\dagger D^\mu\phi &= \frac{1}{2}\partial_\mu\rho\partial^\mu\rho + \frac{1}{2}\frac{(\rho+v)^2}{v^2}(\partial_\mu\xi)^\dagger\partial^\mu\xi \\ &\quad -g\frac{(\rho+v)^2}{v}A^\mu\partial_\mu\xi + \frac{1}{2}g^2(\rho+v)^2A^\mu A_\mu\end{aligned} \tag{1.8}$$

Again the field redefinition generates mass, but this time for a vector gauge field. An additional term is also generated which does not correspond to a standard interaction. However, this can be remedied by means of a redefinition of the gauge field, allowing the introduction of a massive field $B_\mu(x)$ defined by

$$B_\mu(x) = A_\mu(x) + \frac{1}{gv}\partial_\mu\xi(x) \tag{1.9}$$

which restores the Lagrangian to the form:

$$\begin{aligned}L &= \frac{-1}{4}B_{\mu\nu}B^{\mu\nu} + \frac{1}{2}m_B^2B^\mu B_\mu + \frac{\lambda^2}{2}(\rho^2+2\rho v)B^\mu B_\mu \\ &\quad +\frac{1}{2}\partial_\mu\rho\partial^\mu\rho - \frac{1}{2}m_\rho^2\rho^2 - \frac{\Lambda}{4}\rho^4 - \Lambda v\rho^3\end{aligned} \tag{1.10}$$

One of the physical fields introduced in the symmetry breaking process ($\xi(x)$) has disappeared. Once all trace of the Nambu-Goldstone boson field $\xi(x)$ has been removed, instead of a massless gauge field the theory contains a massive vector gauge field $B_\mu(x)$ of mass $m_B = gv$, as well as a massive scalar, $\rho(x)$ of mass $m_\rho = \sqrt{-2\mu^2}$. What has happened is that the spontaneous symmetry breaking has caused the original massless gauge field to absorb the Nambu-Goldstone boson $\xi(x)$. Colloquially, the massless vector boson has "eaten" the scalar field $\xi(x)$, and in doing so has become the massive vector gauge field. This allows the calculation of the W and Z vector boson masses, given by the following formulae:

$$m_{W^\pm}^2 = \frac{g_2^2v^2}{4},\ m_{Z^0} = (g_1^2+g_2^2)\frac{v^2}{4} = \frac{m_W^2}{\cos^2\theta_W} \tag{1.11}$$

where g_1 and g_2 are coupling constants and θ_W is the Weinberg, or weak mixing angle.

So, by means of spontaneous breaking of a local gauge symmetry (aka The Higgs mechanism), gauge bosons can be given mass. Beyond giving masses to the gauge bosons, the Higgs mechanism is remarkable in that it can be simultaneously used to generate masses for the fermions in the theory [10]. Introduction of this Higgs SU(2) doublet allows Yukawa-like terms of the form

$$\sqrt{\frac{1}{2}} g_f v(\overline{f_L} f_R + \overline{f_R} f_L) \tag{1.12}$$

to be written, with the mass of the fermion being given by $g_f v/\sqrt{2}$.

With this generating mechanism, the Standard Model predicts the existence of a Higgs boson (the physical manifestation of the Higgs mechanism) but does not predict its mass, because very little of the Standard Model we have observed depends directly on this mass. However, by imposing certain requirements of internal consistency on the theory, the range of possibilities may be narrowed [6]. Two examples of these requirements are triviality (a trivial theory would be non-interacting at low energies) and unitarity (the probability of scattering from a particular state to another grows with energy and can be greater than one) [10]. The upper bound on the mass obtained by imposing these constraints is of the order of 1 TeV/c^2. However, the predicted width of the Higgs boson mass peak in this mass range is very large, creating difficulties in any attempt to accurately measure the mass of a very heavy Higgs boson. For example, an 800 GeV/c^2 Higgs boson has a width in excess of 200 GeV (the width $\sim \frac{1}{2} M_h^3$ (TeV units)).

Current experimental limits show that its mass is greater than about 60 GeV, and planned accelerator upgrades in the near future (LEP II) should be able to extend the mass range of the search only up to about 100 GeV/c^2. Therefore it would be useful to build an accelerator capable of searching for the Higgs up to at least 1 TeV/c^2. At this energy, either the Higgs will be produced or some other

exotic particle signifying new physics will be discovered. The LHC will be the first accelerator capable of exploring this mass regime.

1.4 LHC

1.4.1 Physics Interests

The most prominent physics question that it is hoped the LHC will answer is whether or not the Higgs boson exists. The Standard Model Higgs boson is predicted to lie in the mass range below 1 TeV/c^2, making the entire range of possible Higgs masses accessible at the LHC, with the possible exception of a low mass Higgs with $M_h < 130$ GeV/c^2. There are many Higgs particle production mechanisms possible at the LHC. However, since the LHC will be a proton-proton collider, the dominant process for Higgs production up to a Higgs mass of around 1 TeV/c^2 is gluon fusion, with a significant contribution from vector boson fusion processes for heavy Higgs production. The basic Feynman diagrams for these processes are given in Figure 1.2.

Although the detectability of the Higgs boson is the benchmark physics issue at the LHC, and the focus of this thesis, it is not the only source of interesting physics. The LHC will also be an important machine in exploring top physics, B-physics, supersymmetry, technicolour and compositeness along with many other interesting physics topics. While not considered in any detail here, an extremely brief review of the usefulness of the LHC in some of these areas is given below.

The LHC will act as the world's first "top factory". Even at the relatively low luminosity of its first few years of operation, the LHC will produce approximately

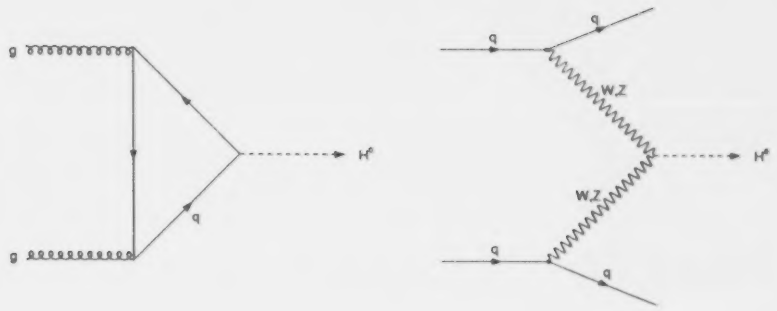

Figure 1.2: The Feynman diagrams for Higgs boson production via gluon fusion and vector boson fusion at a pp collider

10^7 $t\bar{t}$ pairs per year. This will allow for a much more precise measurement of the top quark mass and for the study of rare top decays. The LHC also provides an environment in which to perform extensive B-physics studies. These include the search for and measurement of CP-violation, the measurement of B_s^o mixing, searches for rare decays, the study of B-baryon decay dynamics and spectroscopy of rare B hadrons [1]. Also, supersymmetric extensions of the Standard Model predict the existence of many new particles over a large mass range. The LHC will have access to more of this range than any previous machine and, as such, will be able to conduct supersymmetric particle searches in previously unexplored mass regimes.

Figure 1.3 [11] shows the cross-sections for many interesting new physics processes at the LHC as well as expected Standard Model processes. This plot shows that for many potentially interesting physics processes, the LHC cross-section is very high compared to previous machines. However, the total cross-section shown in Figure 1.3

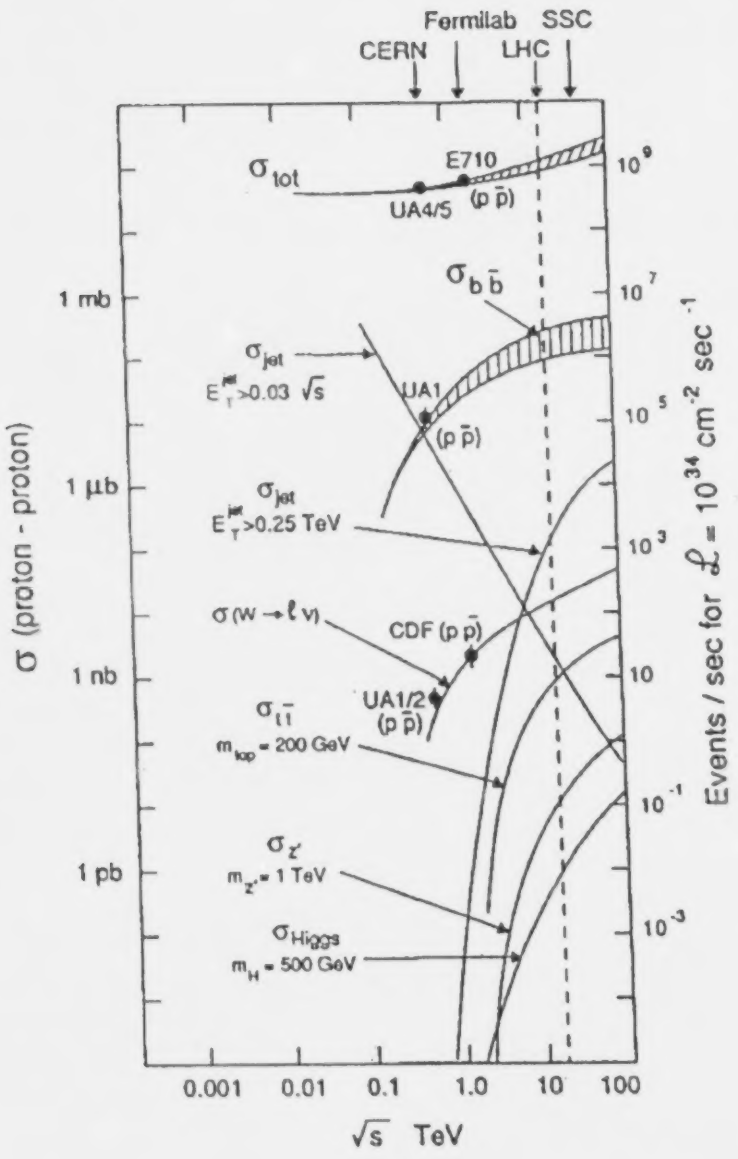

Figure 1.3: Cross-sections of many interesting physics processes at the LHC.

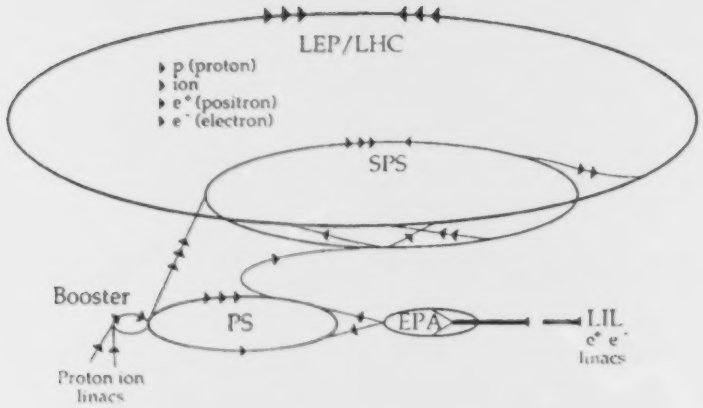

Figure 1.4: The LHC injector complex and main LHC ring are pictured here. The energies of each injection stage are as follows: linacs = 50 MeV, PS booster = 1.4 GeV, PS = 26 GeV, SPS = 450 GeV.

is higher by several orders of magnitude than the predicted Higgs cross-section. This means that the LHC detectors will have to be flexible enough to detect a wide range of physics processes despite a very large background.

1.4.2 Design

The LHC is the next major project planned for CERN [7]. It will be a proton-proton collider capable of producing proton collisions with a centre of mass energy of 14 TeV at a luminosity of 10^{34} cm^{-2} s^{-1}. It will be installed in the LEP tunnel (after the removal of the LEP ring) which has a 27 km circumference. The injector complex consists of 50 MeV linacs, the 1.4 GeV PS booster, the 26 GeV PS (proton synchrotron) and the 450 GeV SPS. The injector complex and LHC main ring are shown in Figure 1.4.

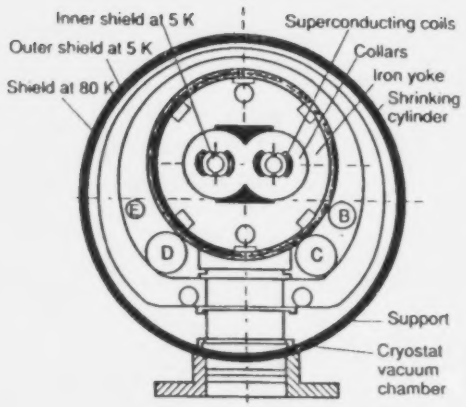

Figure 1.5: The cross-section of an LHC standard two-in-one dipole in its cryostat.

In addition to running as a proton-proton collider, the LHC will be able to run as a heavy ion collider (Pb-Pb) with a centre of mass energy of 1150 TeV and a peak luminosity of 10^{27} cm^{-2} s^{-1} [12]. Also, the rebuilding of the LEP ring above the LHC ring would allow high energy e-p collisions to take place. The mode of running considered in this thesis is the proton-proton mode.

Since the LHC will be colliding beams of like-charged particles, two separate beam-lines are necessary in order to allow two proton beams to circulate in opposite directions. The direction of the magnetic field in one beam-line must be opposite to that of the second beam-line. CERN has decided to accomplish this by using a magnet design that combines the two guide fields into a single magnet design [11] as shown in Figure 1.5. This option was chosen over two separate magnets due to space restrictions in the LEP tunnel. In order to meet the LHC energy requirements, these 14.2 metre magnets will be superconducting (cooled with superfluid Helium) with a field strength of $\approx$8.4 Tesla. In all, 1296 of these dipole magnets will be required

Energy	14 TeV
Dipole Field	8.4 T
Coil Aperture	56 mm
Aperture Separation	194 mm
Luminosity	$10^{34} cm^{-2} s^{-1}$
Injection Energy	450 GeV
Circulating Current	0.54 A
Bunch Spacing	25 ns
Particles/Bunch	10^{11}
R.M.S. Bunch Length	0.075 m
No. of Bunches	2835
Energy Loss/Turn	6.7 keV

Table 1.2: The design parameters of the LHC.

for the LHC. However, dipole bending magnets are not the only superconducting magnets needed for the LHC ring; 3.1 metre, 6.9 Tesla superconducting quadrapole magnets are also needed for beam focusing.

In order to maintain high luminosity, bunch lengths (the longitudinal spread of a bunch of particles being used in a collision) must be kept short. Short bunch lengths keep degradation in luminosity caused by beam crossing angle to a minimum. Short bunch lengths will be obtained at the LHC with RF cavities operating at 400 MHz needing a voltage of 8 MV at injection and 16 MV in collision. There will be eight of these superconducting cavities per beam (each beam has a separate RF system). Table 1.2 summarizes the LHC performance parameters as they as currently envisioned.

An important feature of the LHC is that it is designed to reach a peak luminosity of $\sim 1 \times 10^{34}$ cm^{-2} s^{-1} (after a build-up from 10^{32} cm^{-2} s^{-1} over a few years). This luminosity improves the chance of finding the Higgs particle at the LHC while putting serious demands on LHC detectors in the areas of radiation hardness and speed of readout. There are four interaction points which could be used for collision experiments planned for the LHC. Currently, general-purpose detectors, designed to meet these demands, are planned for two of the four interaction points. These two detectors are known as ATLAS and CMS. The other two interaction points will eventually be used for a heavy ion (ALICE) and a B-physics experiment (LHCB). The distribution of experimental areas around the LHC ring is illustrated in Figure 1.6. This project focusses on ATLAS, and as such, neither CMS nor the future heavy ion or B-physics experiments will be discussed in any detail.

1.5 ATLAS

ATLAS (*A Toroidal LHC ApparatuS*) is one of the proposed detectors for the LHC and is the only one considered in detail in this thesis. ATLAS is a general purpose detector designed to detect electrons, muons, jets and missing transverse energy [7]. A schematic view of ATLAS is shown in Figure 1.7.

At the LHC, a general purpose detector such as ATLAS must be able to detect and momentum analyze the high P_T (transverse momentum) fermions or bosons produced by the physical processes in which we are interested as well as measure missing energy, a key signature for new physics. A key constraint is placed on LHC detectors by the very high luminosity at which the LHC will operate. Luminosity is defined in Equation 1.13 where N_1 and N_2 are the numbers of particles in each bunch, n is the number of bunches in either beam, A is the cross-sectional area of the beam and f is

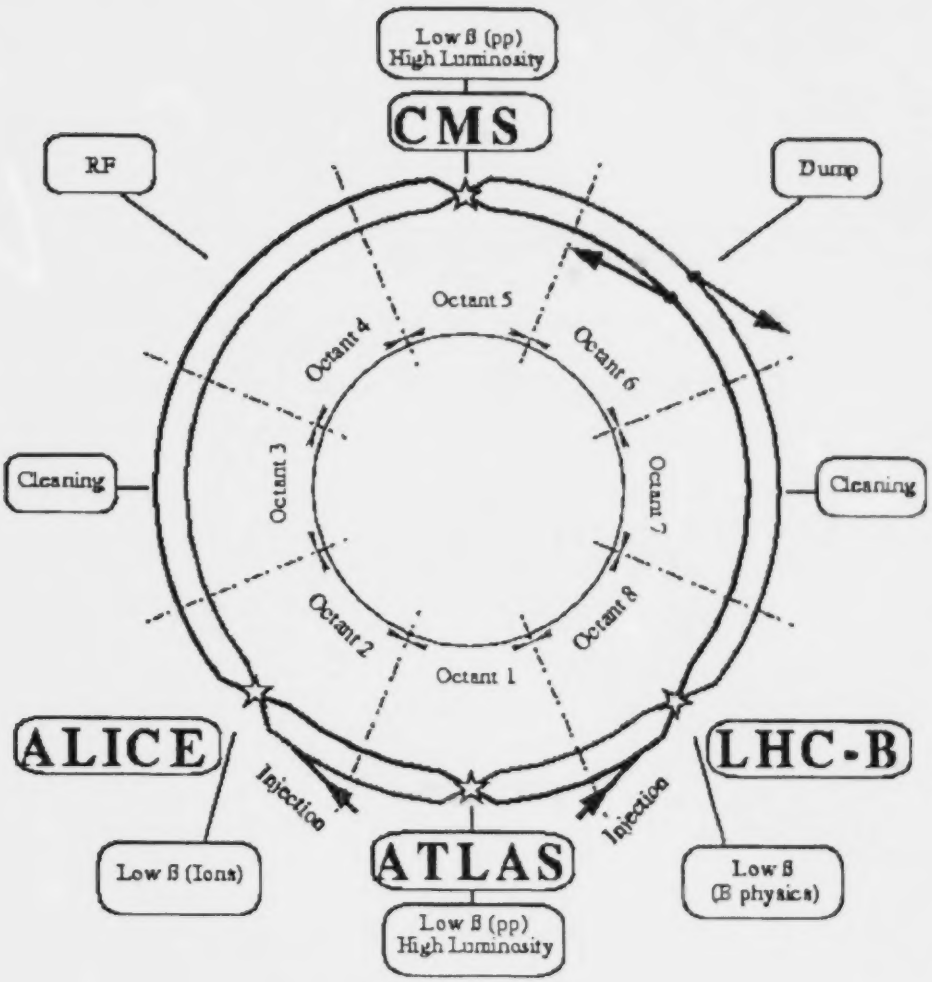

Figure 1.6: The four planned LHC detectors are illustrated. The first two to be built will be ATLAS and CMS. ALICE is a planned heavy ion experiment and LHC-B refers to a possible B-physics experiment.

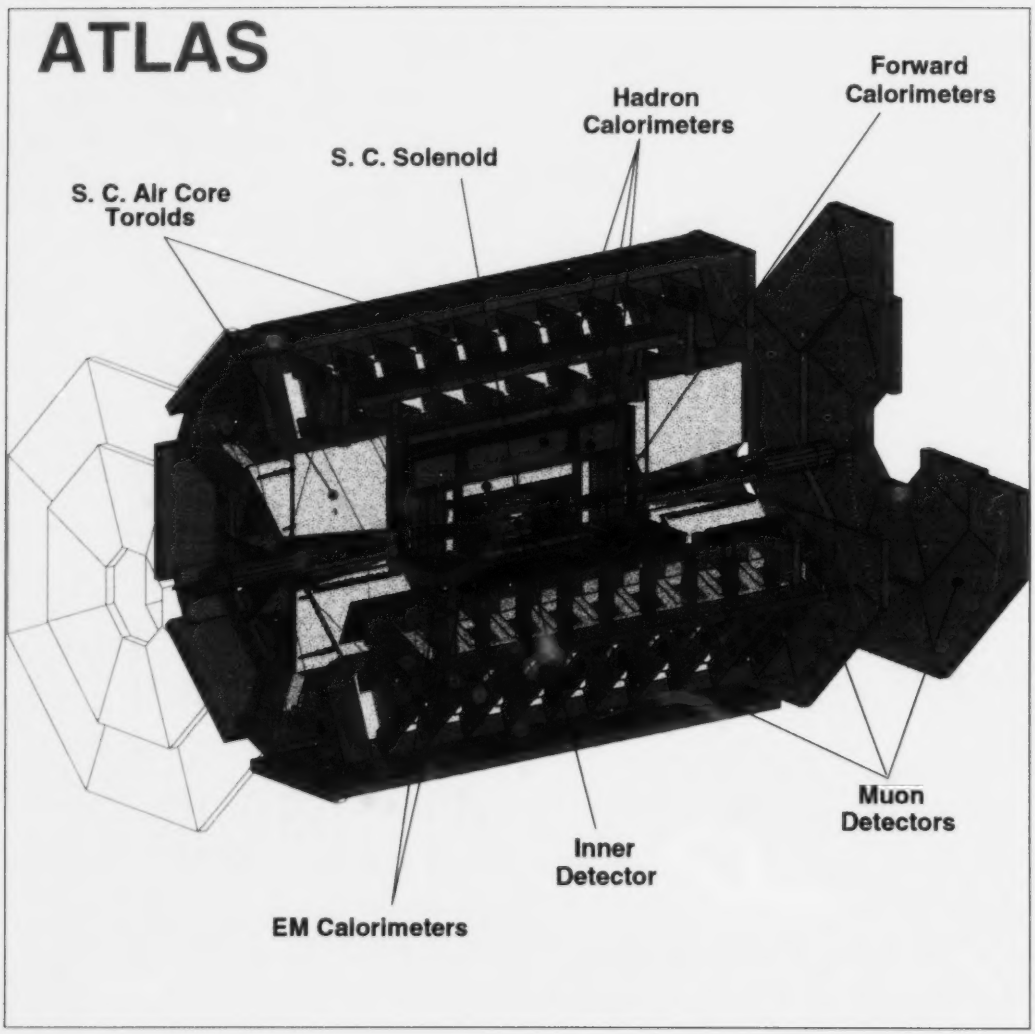

Figure 1.7: The proposed ATLAS detector

the revolution frequency.

$$L = fn\frac{N_1 N_2}{A} \tag{1.13}$$

This luminosity can be explained in the following way. Beams consist of 'bunches' of particles which cross each other at the interaction points. To obtain the highest possible luminosity, bunches must contain the maximum possible number of particles, must cross each other as frequently as possible and the beam area must be as small as possible. In the LHC these crossings will occur about once every 25 ns. For each bunch crossing (assuming a luminosity of 10^{34} particles/cm^2/sec) there will be, on average, 23 events. This means that any LHC detector will have to be able to process this large amount of information at the LHC bunch crossing rate of 40 MHz. Further, the detector components will have to be able to withstand radiation doses of up to 10^6 Gy (see Table 1.3) over a period of 10 years. ATLAS will be optimized to perform at the highest LHC luminosities while maintaining good performance at lower initial luminosities.

ATLAS, as a general-purpose detector, is actually made up of many sub-detectors, each built to perform specialized tasks. These subsystems include electromagnetic calorimetry, forward calorimetry, an inner detector, a muon system and hadronic calorimetry. Although the main focus of this project is the hadronic end-cap calorimeter, a discussion of the rest of the calorimetry and a very brief discussion of the other parts of ATLAS have been included in Chapter 2. A more detailed description can be found in the ATLAS technical proposal [1], produced in December 1994.

Detector Component	Dose ($kGy\ yr^{-1}$)	Neutron Fluence ($cm^{-2}yr^{-1}$)
Pixel	34	$5.9 \cdot 10^{13}$ tot. $1.6 \cdot 10^{13}$ neut.
SCT (barrel)	15	$2.7 \cdot 10^{13}$ tot. $1.0 \cdot 10^{13}$ neut.
SCT (Forward)	10	$2.2 \cdot 10^{13}$ tot. $1.6 \cdot 10^{13}$ neut.
GaAs	16	$1.3 \cdot 10^{13}$
MSGC	7.2	$2.0 \cdot 10^{13}$
Barrel TRT	2.5	$6.3 \cdot 10^{12}$
End-cap TRT	4.7	$1.3 \cdot 10^{13}$
Barrel EM calo.	0.6	$1.5 \cdot 10^{13}$
Barrel tile calo.	0.020	$1.6 \cdot 10^{12}$
EB tile calo.	0.036	$2.0 \cdot 10^{12}$
Barrel/EB crack	0.025	$1.0 \cdot 10^{12}$
end-cap EM calo.	53	$4.1 \cdot 10^{14}$
end-cap had. calo.	12	$6.1 \cdot 10^{14}$
Forward calo.	2300	$1.0 \cdot 10^{16}$

Table 1.3: This table contains expected ATLAS radiation doses for each detector region. In this table, tot. means the total fluence while neut. refers to fluence of neutral particles only

CHAPTER 2

The Design of ATLAS

This section presents an overview of the design of the subsystems that make up the ATLAS detector. All the geometries presented here refer to the technical proposal design of ATLAS (and hence the figures included in this chapter come from the technical proposal), more recent designs of ATLAS now exist, but are not considered here, as they have not been incorporated in to the simulations presented later in this thesis. The section begins with brief overviews of calorimetry and energy resolution, the inner detector and muon systems. Next, a detailed examination of electromagnetic calorimetry is presented, followed by a thorough description of the ATLAS hadronic calorimetry. Finally, short descriptions of the forward calorimetry and the ATLAS trigger and data acquisition system (DAQ) are presented.

In order to better understand the design of these subdetectors, the reader must be familiar with the coordinate system used to define positions in ATLAS. Since ATLAS has a cylindrical geometry, it would seem natural to work in the cylindrical coordinates r, z and ϕ. However, instead, z, ϕ and the pseudorapidity (η), defined as:

$$\eta = -\ln \tan(\theta/2)$$

are used. This quantity is zero at $\theta = 90°$ (θ is measured from the beamline) and becomes infinite as the θ goes to zero. The pseudorapidity has certain qualities which make it particularly useful as a coordinate in high energy physics. The first is the fact that it is Lorentz invariant, making it easy to use in an environment of highly

energetic (and hence highly relativistic) particles. The second advantage is that a bin of a certain size in pseudorapidity will actually be smaller (in cm^2, for instance) closer to the beamline than it is at larger angles to the beamline. This produces a particle distribution which is relatively flat in η. So, for the remainder of this thesis, η will be used refer to the pseudorapidity and ϕ will refer to the azimuthal angle.

2.1 Calorimetry, Jets and Energy Resolution

A calorimeter uses alternating layers of absorber and sensitive material to measure the energy of a particle by sampling the energy deposited in the sensitive medium (eg. liquid Argon) by the particle shower induced by the incident particle. The resolution of a calorimeter is a way of quantifying the relative spread of the energy distribution it produces as its measurement of particle energy. This fractional energy resolution is defined by the following equation:

$$\frac{\sigma}{E} = \frac{a}{\sqrt{E}} \oplus b \oplus \frac{c}{E} \tag{2.1}$$

where $\oplus$ refers to adding in quadrature.

The first term on the right-hand side of this equation is called the sampling term. As sampling is a statistical process, with the measured energy being proportional to the number of samples, the energy resolution is therefore proportional to $\sqrt{no.of samples}$. Thus, the energy resolution of a calorimeter can be improved by either increasing the frequency with which the shower is sampled (ie. more sampling layers per depth of calorimeter) or by increasing the depth of each sampling layer. Clearly, this term decreases in importance with increasing energy due to the factor of $\sqrt{E}$ in the denominator.

The second term in Equation 2.1 is known as the constant term, as it is

independent of energy. This term can become the dominant source of error at high energies because the other two terms in the equation shrink with increasing energy. The constant term takes into account non-uniformities in calorimeter response due to such factors as mechanical non-uniformities and incomplete shower containment. In the case of hadronic calorimeters this term can also take into account differing response to electrons and pions. Finally, the third resolution term describes electronic noise effects and usually comes into play at low energies.

The measurement of the energy resolution is, in this project, restricted to the energy resolution of particle jets. A jet of particles is formed when a quark or gluon is produced and hadronizes. To understand this hadronization, consider the process $e^+e^- \rightarrow q\bar{q}$ in which there is a quark and an antiquark leaving the interaction region [14]. These quarks each carry a colour charge which we believe to be confined, and so the force between them gets stronger as they get farther apart. The "string" between them will then break, leading to the creation of additional $q\bar{q}$ pairs which, in turn, form a collection of colourless states with short lines of force ($\sim$1 fm). These states are, of course, low mass hadrons (mainly pions) [15]. Therefore, a "jet" of low mass hadrons has been produced.

When a jet of hadrons enters a calorimeter, neutral pions will decay into two photons creating an electromagnetic shower, despite the fact that it is due to a hadron. The charged pions, on the other hand, will interact with nuclei, producing more and more particles until the energy of all of the particles is low enough that all further losses take place solely via ionization (ie. energy becomes too low for nuclear interactions to take place). So, neutral pions produce showers which are EM in character while charged pions produce more hadrons (including π^0s which shower electromagnetically, etc.). This means that, for a given jet, energy deposited in a calorimeter is divided into separate EM and hadronic components and the fraction

of jet energy in each component can fluctuate a great deal from one jet to another. This type of shower fluctuation makes it more difficult to measure the energy of a jet in a calorimeter than it is to measure the energy of an electron or a photon (particles which shower only electromagnetically). Also, a hadronic shower typically contains many fewer particles than does an EM shower. For example, a 50 GeV pion interacting in lead will produce on the order of 50 secondary pions while a 50 GeV electron will produce approximately 1000 particles at its shower maximum alone [14]. In sampling calorimeters, measuring processes with few particles leads to statistical fluctuations which degrade the energy resolution performance of the calorimeter. A third obstacle to good jet energy resolution is that many of the low energy nuclear processes involved in hadronic shower production are not particularly well understood. This means that, while electromagnetic showers can be very well modelled in Monte Carlo simulations, simulations of hadronic showers are not as reliable, making detector opitimization via Monte Carlo more difficult for jets than for EM interactions. Another difficulty in measuring hadronic showers is due to the fact that most calorimeters have a different response for electrons than they do for pions. This is because, in an electromagnetic shower, the bulk of the incident energy appears eventually in the form of ionization [16]. However, in a hadronic shower, approximately 30% of the incident hadron energy is lost by the breakup of nuclei, nuclear excitation and evaporation of neutrons or protons and does not give an observable signal. This discrepancy between EM and hadronic energy measurements must be remedied to acheive best calorimeter performance, making the calorimeter a "compensating" calorimeter.

Despite the intrinsic difficulty in precisely measuring the energy of a jet of particles, there are certain minimum energy resolution requirements that must be satisfied for good physics performance of ATLAS calorimetry (these requirements

will be detailed later in this chapter). Thus, the challenge is to optimize the design of the calorimetry in order to satisfy minimum requirements for all three terms of the energy resolution equation for each of the individual calorimeters in ATLAS.

2.2 Inner Detector

As its name indicates, the inner detector is located inside all of the other detector components, closest to the beam line. The basic functions of the inner detector are:

1. to perform precise measurements of leptons and to identify electrons and photons at high luminosities
2. to perform τ and b tagging at lower luminosities. [17].

The inner detector can be divided into three parts which are both geometrically and mechanically separate. These parts are a barrel part and one end-cap part on each side. Most of the barrel region is characterised by 3 active layers with a cylindrical geometry (barrel straw tracker, barrel silicon strip layers and barrel pixels). Straw trackers are cylindrical drift tubes filled with gas while silicon strips layers and barrel pixels are semiconductor detectors. The basic priciple of semiconductor detectors is that the passage of ionizing radiation creates electron-hole pairs in the semiconductor which are collected by an electric field. The difference between strips and pixels is mainly geometry, pixels being closely spaced pads capable of good two dimensional reconstruction while strips give better spatial resolution in one coordinate than the other. The details of these designs can be found in the ATLAS Technical Proposal [1] and the technical proposal layout of the inner detector is illustrated in Figure 2.1.

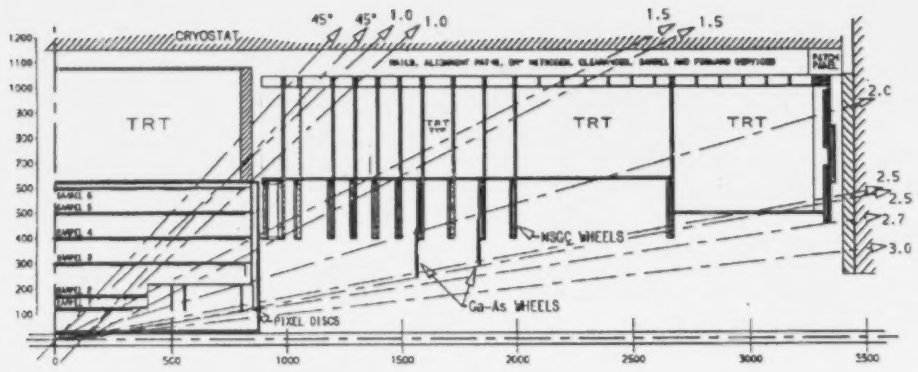

Figure 2.1: Layout of the ATLAS inner detector

The three different technologies employed in the design of the inner detector (pixels, strips and straw trackers) each have specific advantages that determine their location and function within the inner detector. Of these three different detector technologies, the pixel detectors are installed closest to the beam pipe. ATLAS' multi-layer pixel system provides two-dimensional spatial information for pattern recognition and is much more radiation-resistant than silicon strip detectors. The silicon strip detectors are used for larger area precision trackers. GaAs will likely be used in the strip detectors in the forward region due to its higher radiation tolerance. The straw tracker will be used at larger radii, where the track density is relatively low. The straw-tube system is also known as the Transition Radiation Tracker (TRT).

2.3 Muon System

The quality of the muon measurement has been one of the most important design criteria for ATLAS. The reason for this is that good muon momentum measurements are essential for recognizing decays such as $H \rightarrow ZZ \rightarrow 4\ell^{\pm}$ (the charged leptons could be any of e^+, e^-, μ^+, μ^-, τ^+ or τ_-) and $H \rightarrow ZZ \rightarrow qq\mu\mu$ (all quark flavours are allowed except for top).

The muon system for ATLAS is composed of three large superconducting air toroid magnets, precision tracking detectors with 60μm intrinsic resolution and a powerful dedicated triggering system. The tracking detectors combine several different technologies, including monitored drift tube chambers, cathode strip chambers, resistive plate chambers, and thin gap chambers.

Monitored drift tube chambers* (MDTs) are used at low η, up to $|\eta| = 2$. At higher values of η, the need for increased granularity has led to the choice of cathode strip chambers (CSCs) instead of MDTs. The choice of trigger chamber technologies depends primarily on the rate capability and spatial resolution of each technology. At $|\eta| < 1.1$, where the rate is relatively low and spatial resolution is not as important, resistive plate chambers (RPCs) have been chosen. For triggering in the region $1.05 < |\eta| < 2.2$, where the rate is higher and spatial resolution is more important, thin gap chambers (TGCs, a form of wire-chamber designed to be very thin) have been adopted. Figure 2.2 shows the design of the ATLAS muon system.

*These drift tubes are called "monitored" because of the sophisticated laser alignment system used to monitor the position of each chamber relative to the other chambers and to the rest of the detector

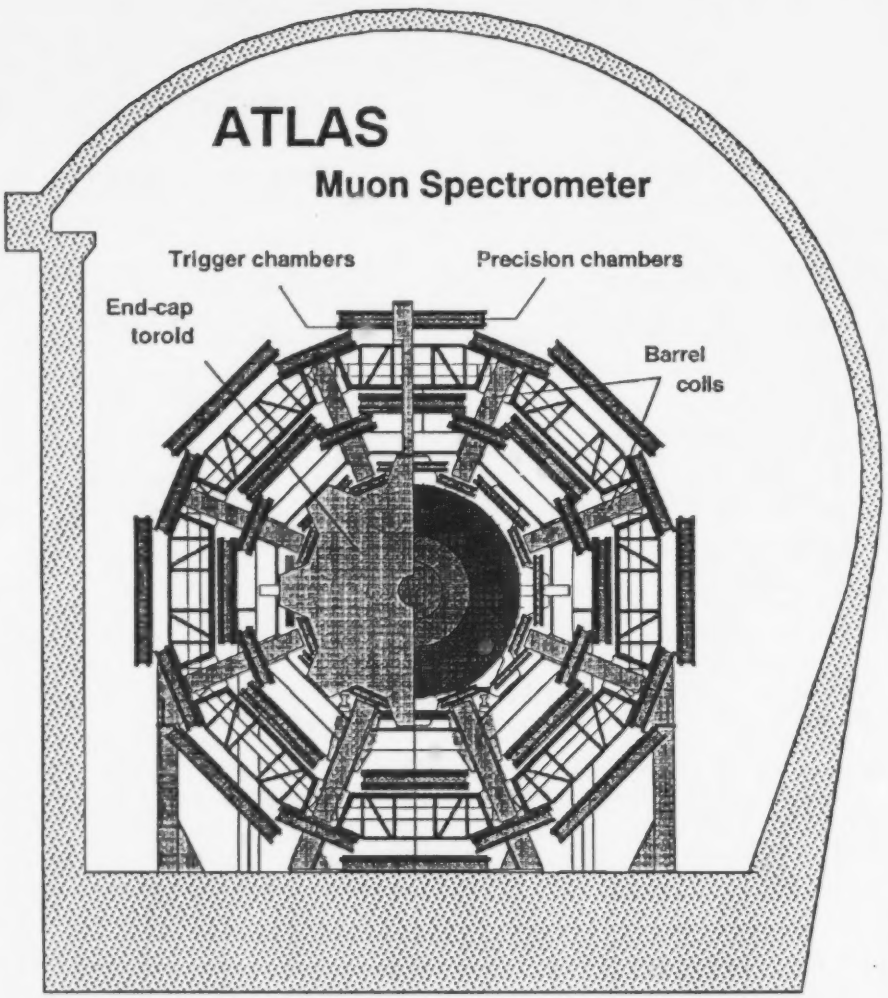

Figure 2.2: The ATLAS Muon Spectrometer (radius is approximately 11 metres).

2.4 EM Calorimetry

Many of the important physics processes at the LHC involve decays to electrons or photons. Detection of these processes depends heavily on good electromagnetic (EM) calorimetry. Thus, the EM calorimetry must meet stringent requirements in terms of acceptance, dynamic range, particle identification, energy resolution and direction measurement. Further, the design is also constrained to operate in the high radiation environment of ATLAS, so it must be radiation hard with good stability over the life of the detector ($\sim$ 10 years under normal ATLAS operating conditions, ie. a few years to build from a luminosity of 10^{32} $cm^{-2}s^{-1}$ to full luminosity of 10^{34} $cm^{-2}s^{-1}$).

The electromagnetic calorimetry in ATLAS is divided into two major regions, barrel and end-cap covering a pseudorapidity range from -3.2 to 3.2. Both the barrel and end-cap regions are sampling lead-liquid argon calorimeters with novel "accordion" geometries, shown in Figures 2.3 and 2.4. In front of each of these accordion calorimeters there are finely segmented presamplers, designed to pinpoint particle position and recover energy lost by early-showering particles.

The EM barrel calorimeter consists of two identical half-barrels covering a pseudorapidity range of $|\eta| < 1.4$. It must be designed as a hermetic detector, allowing the minimum number of particles to escape through uninstrumented cracks in the detector. For this reason (among others) it was decided that a new "accordion" geometry would be used. In this design the absorber plates are bent into the shape of an accordion as shown in Figures 2.3 and 2.4. These figures, which represent the technical proposal design, show that folding angle varies with radius. The folds vary from 90.7° to 67.5° as radius increases in order to keep the gap width and the sampling fraction constant. In this scheme, it is possible to design a barrel calorimeter without uninstrumented cracks, as the connections to the preamplifiers come from the end

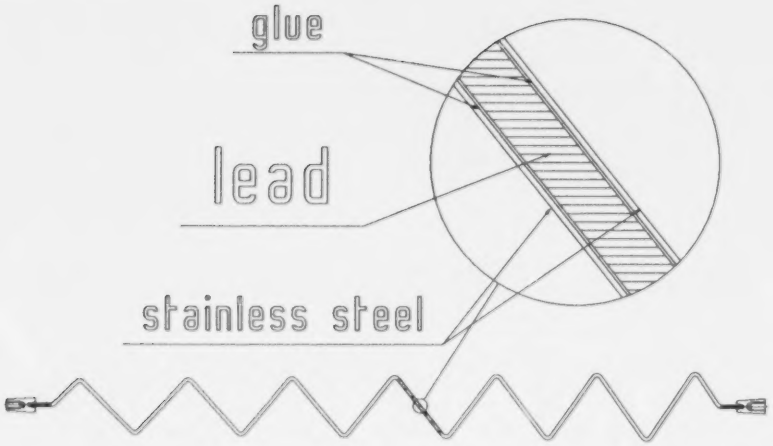

Figure 2.3: Scheme of an absorber plate

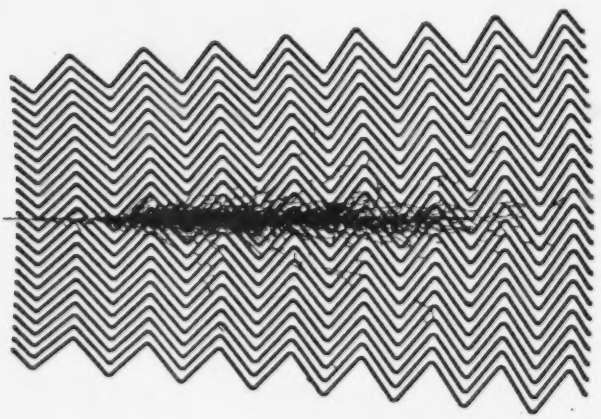

Figure 2.4: A simulation of an electromagnetic shower due to a 100 GeV electron in an accordion geometry EM calorimeter. Tracks down to 10 MeV are shown.

of a tower instead of out the side of a tower as in a conventional calorimeter design. The barrel accordion will have a segmentation of $\delta\eta \times \delta\phi \simeq 0.003 \times 0.1$ in the first depth compartment, 0.025×0.025 in the second compartment and 0.025×0.05 in the third compartment. This segmentation should permit good electron and photon identification and position resolution.

At high η, in the range $1.4 < |\eta| < 3.2$, the electromagnetic calorimeter, which also has an accordion geometry, forms a part of the end-cap detector. To ensure good ϕ uniformity, the folding angle of the accordion in the end-cap varies with radius. For technical reasons, the folding angle must be kept between 60° and 120°. This makes it necessary to divide each end-cap into two coaxial wheels. The segmentation does not have to be as fine in this region as in the barrel, because most of the processes of interest from the EM calorimetry point of view are high P_T processes, expected to be in the central region. For this reason the first two depth compartments have a segmentation of $\delta\eta \times \delta\phi = 0.05 \times 0.05$ while the third compartment has a segmentation of 0.05×0.1.

2.5 Hadronic Calorimetry

The main tasks in hadronic calorimetry in ATLAS are:

1. To identify jets and measure their energy for inclusive cross-section measurement (jet spectroscopy)

2. To measure missing transverse energy, an important signature in many physics processes.

3. To act as a shield for the muon chambers (detector is 10λ[†] deep.)

For any calorimeter, the resolution is limited by intrinsic effects; the loss of energy to non-interacting particles, different fragmentation for light quarks, heavy quarks and gluon jets, the effect of the magnetic field sweeping radiation (energy) in and out of the jet and calibration factors which can only be calculated from test beam measurements using single particles are some of these effects. Also, at high luminosity, pile-up energy from minimum bias events is a relevant source of error for jets with energies less than 50 GeV.

For the LHC, hadronic calorimetry with an energy resolution of $\frac{\delta E}{E} = \frac{50\%}{\sqrt{E}} \oplus 3\%$ (E in GeV) and a granularity of $\delta\,\eta \times \delta\,\phi = 0.1 \times 0.1$ has been shown to be adequate for the study of the physics processes of interest [1]. In particular, the study presented later in this thesis will show that this is sufficient for the study of the $H \rightarrow ZZ \rightarrow \mu\mu jj$ signal. In the forward region a resolution of $\frac{\delta E}{E} = \frac{100\%}{\sqrt{E}} \oplus 10\%$ and a granularity of $\delta\,\eta \times \delta\,\phi = 0.2 \times 0.2$ is sufficient.

2.5.1 Barrel

In the barrel region, ATLAS contains a large scintillating tile hadron calorimeter with steel as the absorbing material. The technology for this detector is based on a sampling technique with scintillating plates read out by wavelength shifting fibres. New in this approach is the unusual orientation of the scintillating tiles, placed in planes perpendicular to the colliding beams and staggered in depth (as illustrated in

[†] λ is the nuclear interaction length. A single nuclear interaction length is the radius about the centre of a hadronic shower which will contain 95% of the incoming energy. It is defined as: $\lambda = 1/(N_A\sigma)$ where N_A is Avagadro's number, σ is the total cross-section and A is the atomic mass. The equivalent radius for EM showers is 2 × the Moliere radius. An approximate formula for the Moliere radius is $R_M = 7A/Z(\mathrm{gm/cm^2})$, where A is the atomic mass of a material and Z is its atomic number.

Figure 2.5). This, as predicted from Monte Carlo simulations, provides good sampling homogeneity.

2.5.2 End-Cap

The hadronic end-cap is the part of the ATLAS detector upon which this research is focussed. The design goal for the resolution of the jets in the end-cap hadronic calorimeter is $\frac{50\%}{\sqrt{E(GeV)}} \oplus 3\%$. The design also requires good spatial resolution in order to be able to search for heavy Higgs through $H \rightarrow ZZ \rightarrow jj\ell\ell$. The search for this signal, as well as others will be discussed in Section 4.

The hadronic end-cap is a sampling copper-liquid argon calorimeter. The technical proposal design of the hadronic end-cap is shown in Figure 2.6. Its position in the ATLAS calorimeter system is illustrated in Figure 2.7. As can be seen from Figure 2.6, the end-cap has two major divisions in z, known as wheels. The first wheel contains 24 readout cells, while the second wheel contains 32 readout cells. The spatial resolution requirement is met by having a segmentation of $\delta\,\phi \times \delta\,\eta \simeq 0.1 \times 0.05$ for $|\eta| < 1.9$ and 0.1×0.1 for $|\eta| > 1.9$.

The hadronic end-cap will be about 10 interaction lengths[‡] deep and will extend over a pseudorapidity range from $1.5 \leq \eta \leq 3.2$. Since it is at such high η, the hadronic end-cap must operate in very high radiation conditions. Copper was chosen over the more standard iron or steel absorber because of copper's shorter interaction length.

A picture of the cell structure in the hadronic end-cap is given in Figure 2.8. This readout structure consists of $4 \times 1.735mm$ LAr gaps bounded by $2.5cm$ cop-

[‡]If a group of n particles enters a particular material, the depth at which $n - n/e$ have interacted with the material is known as the interaction length in that material.

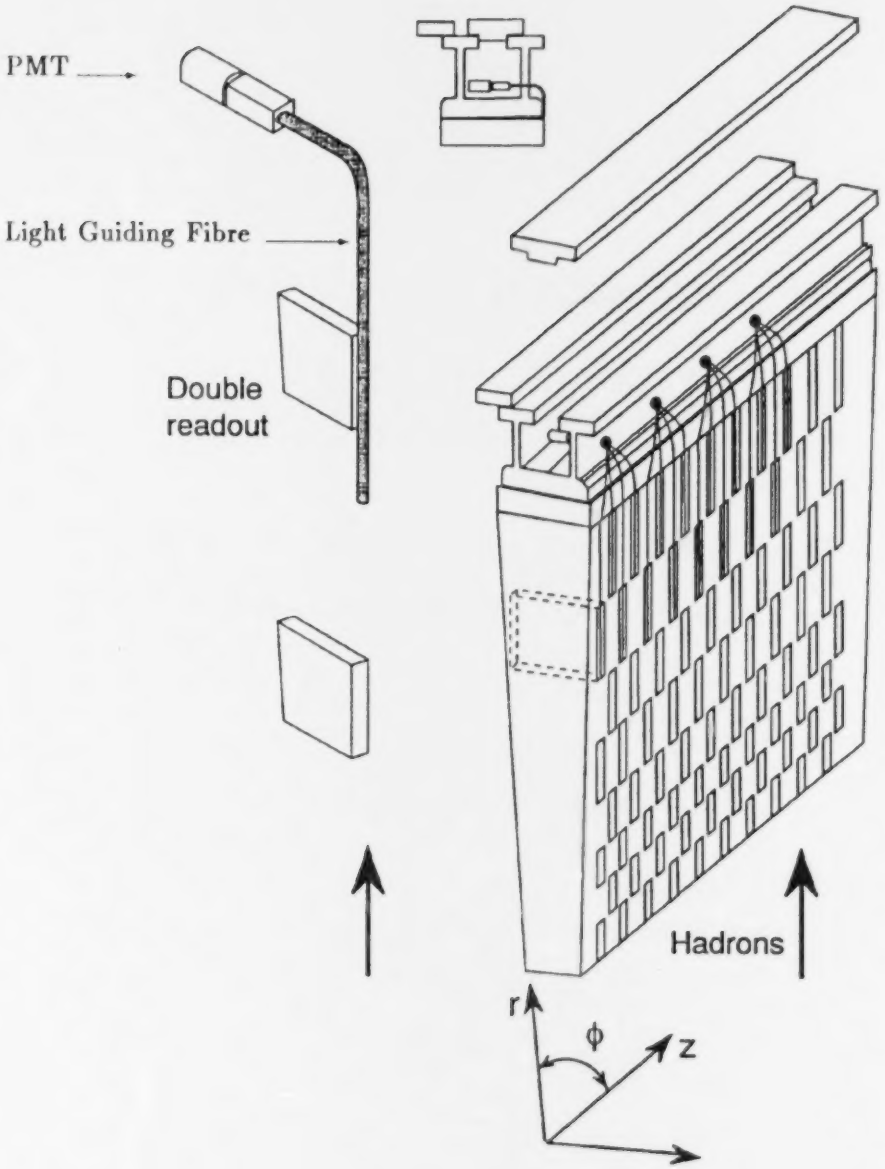

Figure 2.5: Principle of the tile hadronic calorimeter

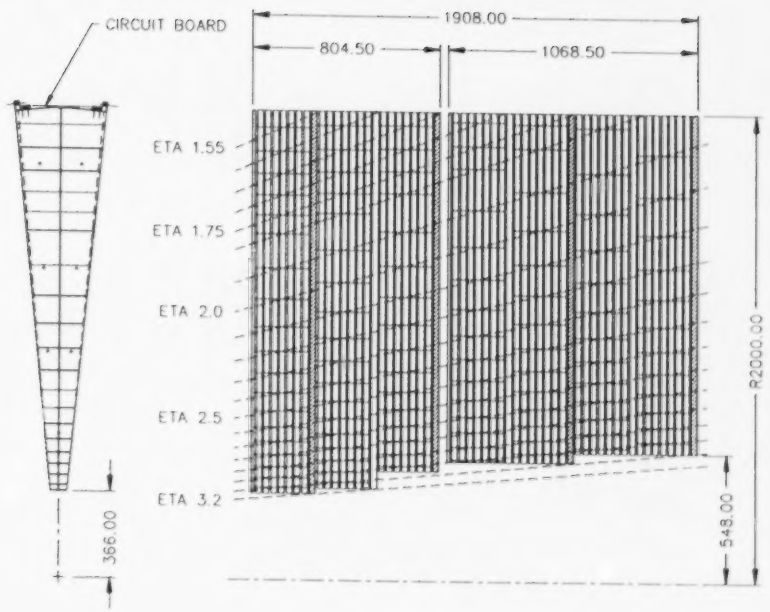

Figure 2.6: R-ϕ and R-Z cross-sections of the technical proposal Hadronic end-cap geometry.

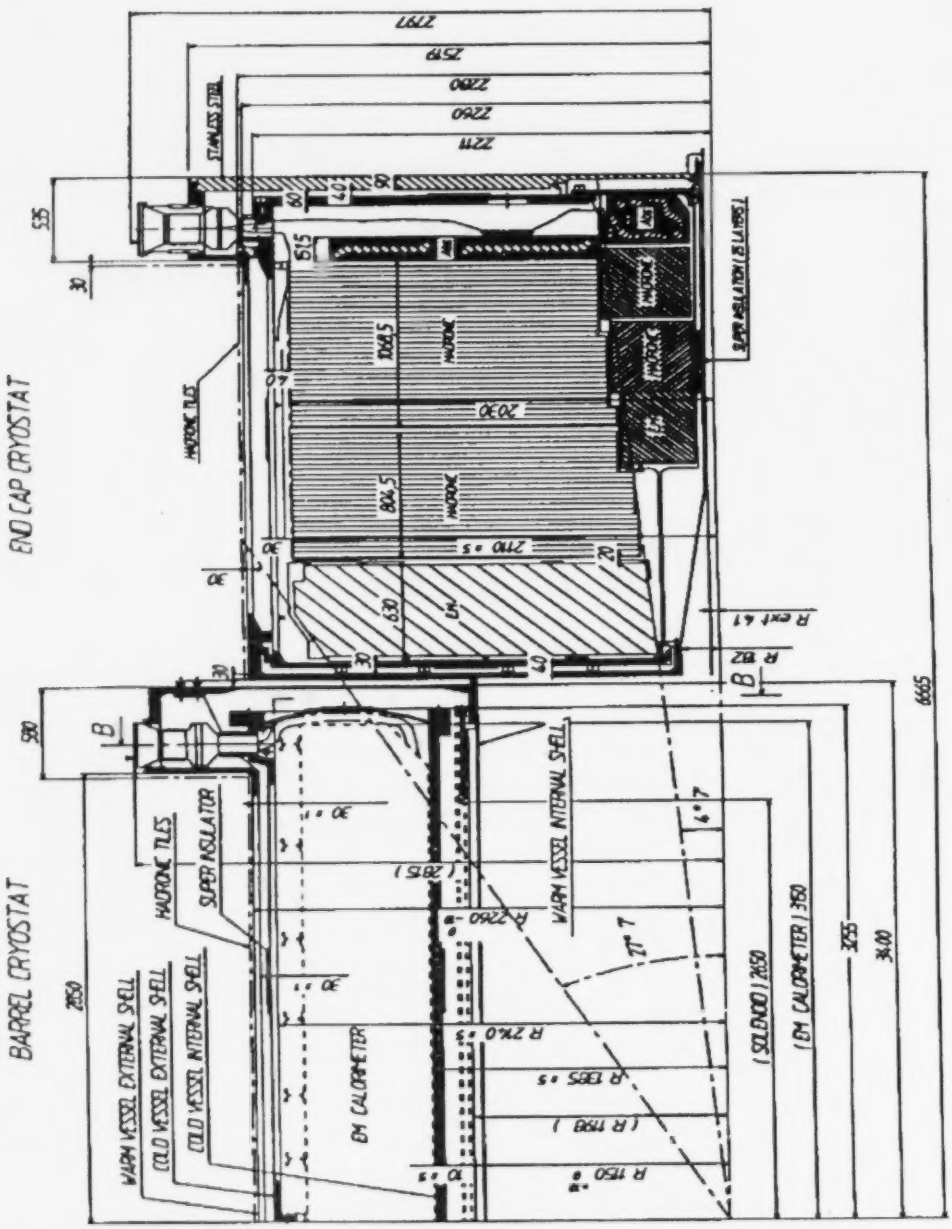

Figure 2.7: Position and cross-sectional view of the hadronic end-cap in ATLAS (technical proposal design, numbers in mm)

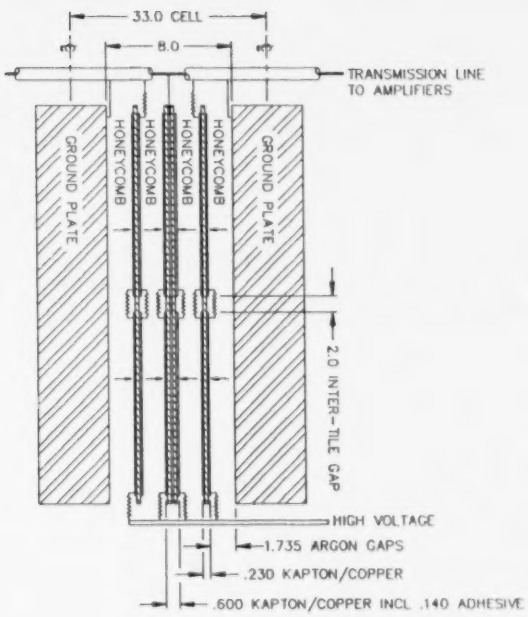

Figure 2.8: Detailed structure of the readout cell

per plates. There are three electronics boards between the two copper plates. Each board is a multilayer sandwich of copper coated polymide film / aramid fibre honeycomb. The latter sandwich contains the etched tile arrays which produce the required readout segmentation of $2\pi/64$ in ϕ and 0.1 in pseudorapidity. The middle board is called the signal board and its function is to read out the signal from the LAr to the preamps. The outer two boards form the electro-static transformer structure.

An Electro-Static Transformer structure (EST) [18] is used in order to reduce the capacitances associated with liquid ionization calorimetry in ATLAS. The principle of this type of transformer is to break down large liquid argon gaps into many smaller gaps connected in series. This arrangement will lead to a lower overall capacitance for each readout cell because capacitors connected in series have capacitances which add as 1/C. Therefore, an EST readout structure matches large capacitance signal towers to low capacitance preamps without the use of an external transformer. This is done in order to minimize electronic noise.

2.6 Forward Calorimetry

In order to have as complete a coverage for jets in ATLAS as possible, forward calorimetry is required. As an example of the usefulness of jet coverage in this region, the forward calorimeter will be an essential part of forward jet-tagging in the search for a heavy Higgs boson which decays to jets via W or Z bosons. However, it is difficult to design a detector to give this η coverage at ATLAS due the fact that the forward region is the most intensely radiated area of ATLAS (see Table 1.3) suffering a dose of 2300 kGy/year. Due to the extreme particle and energy flux, a specialised forward calorimeter is the only detector type which can work in this region. Speed of response and radiation hardness are premier requirements.

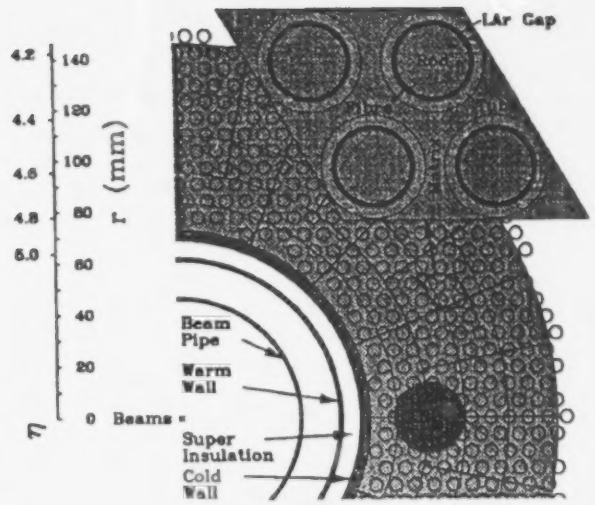

Figure 2.9: Front face of EM Fcal module, dark circle indicates Moliere radius.

The specialised forward calorimeter is a liquid argon calorimeter formed from three modules. The first, or EM, module is made of copper (or brass), so that the EM showers spread enough to give uniform response for reasonably sized electrodes. The second and third modules are hadronic and are made of a combination of stainless steel and a tungsten alloy, in order to limit the transverse spreading of the hadronic showers.

The geometry of the forward calorimeter is not a standard parallel plate design primarily because the high energy flux in this region of the detector requires that the liquid argon gaps be very narrow to avoid buildup of positive argon ions in the gap. Because narrow gaps in a parallel plate structure are hard to maintain, a new structure has been chosen based on rods and tubes as shown in Figure 2.9. The gap width is maintained constant by wrapping a quartz fibre around the tube and allowing Liquid argon to fill the narrow (250 μm) gap between the rod and the tube.

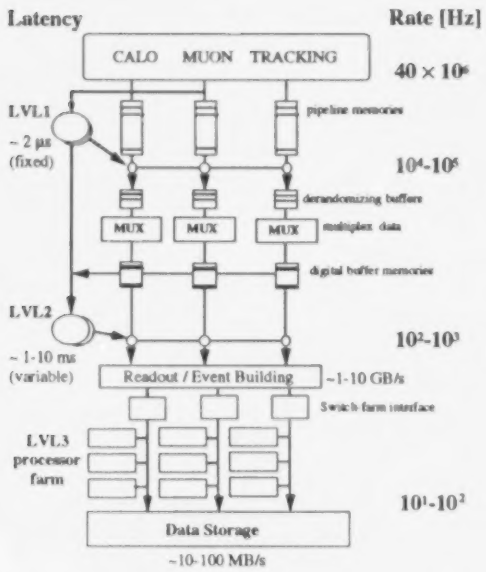

Figure 2.10: Design of the ATLAS trigger system.

2.7 Trigger and DAQ

In ATLAS, the trigger and data acquisition systems (DAQ) are particularly important. The high rate at which data will be produced at ATLAS means that it will be necessary to implement a high speed system to sort through the incoming data and choose which events to store and which ones to discard. This is the role of the trigger and DAQ.

The ATLAS trigger system is divided into three levels. The multi-level structure of this triggering system is illustrated in Figure 2.10. The first level is named the Level I trigger and, as currently designed, works at the LHC bunch crossing rate of 40MHz with latency (time to make a decision) of 2.5μs. It must reduce the data flow

rate to 100 kHz so that the data can be passed to the Level II trigger. In order to run at high speed, the Level I trigger uses a reduced detector granularity and does not include inner detector data. Its function is to identify areas of interest in the detector (for accepted events) and pass the location of these areas on to the Level II trigger. The Level II trigger uses information from the calorimetry, muon system and inner tracking to further reduce the rate from 100 kHz to 1 kHz and has a latency which can vary, ranging as high as 10 ms. It uses the full granularity of the detector in the areas of interest identified by the Level I trigger. Finally, the data is passed to the Level III trigger. The Level III trigger performs complete event reconstruction with a decision time of up to 1 s. It is the Level III trigger which makes the final decision to store the data and it must do so at a rate of 10-100 Mb/s.

CHAPTER 3

End-Cap Simulation and Optimization

3.1 Introduction

Simulation studies of detector design and performance are an important part of the planning process in building modern particle detectors. New designs are produced and the feasibility of existing designs are tested through exhaustive computer simulations. These simulations provide a valuable first look at detector performance and save considerable time and money that would otherwise have to be spent on extensive prototyping.

In the past, significant tests of the performance of the ATLAS end-cap have been performed [19] [20]. These tests show that the performance of the end-cap detector is acceptable with respect to ATLAS design goals. However, further studies to optimize the detector in the presence of pile-up effects are needed.

In this chapter, simulation work done to optimize the design of the ATLAS hadronic end-cap calorimeter is detailed. This simulation work tests the first type calorimeter design requirement mentioned at the beginning of this thesis: whether the calorimeter meets its primary design requirements in a setting that simulates true experimental conditions. Each of the studies presented in this chapter involves testing end-cap design changes to optimise its performance in the presence of pile-up effects, effects which are important under real experimental conditions.

First, ATLAS simulation software packages are introduced. Next, the energy resolution of the hadronic end-cap in the presence of pile-up effects is examined for five different end-cap configurations. The third subsection considers the effect on energy resolution of changing the hadronic end-cap granularity in the presence of pile-up. Finally, the effect of doubling the thickness of the copper absorbers in the second wheel of the hadronic calorimeter is examined in the presence of pile-up.

Included as an appendix to this thesis is an ATLAS note [20] written by Robert Davis and Dugan O'Neil of the University of Alberta and Pierre Savard of the University of Montreal. This note explores energy resolution issues in great detail for the technical proposal end-cap geometry and, as such, is a useful reference in this subject area.

3.2 ATLAS Software

The first step in performing ATLAS simulations is to understand the structure and status of the various ATLAS simulation software packages. The simulation process in ATLAS consists of four steps. They are:

1. generation of events with Monte Carlo physics generators
2. simulation of events in the detector
3. digitization of the raw data
4. reconstruction of the data

These processes can be controlled by several different software packages written at CERN. A flow diagram of the generation software sequence is given in Figure 3.1

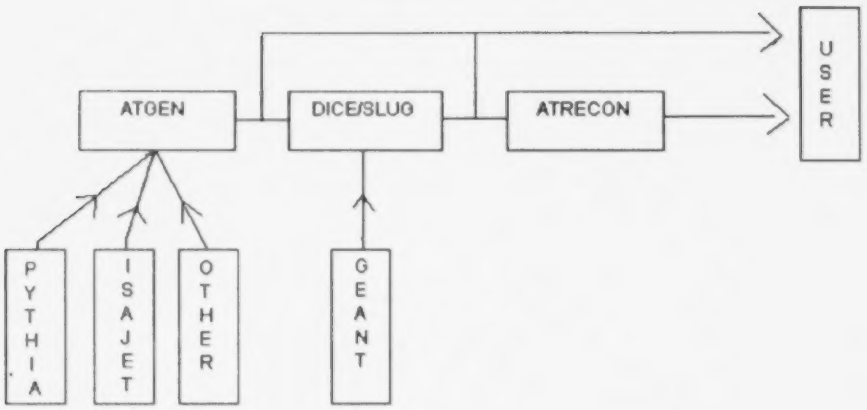

Figure 3.1: A flow diagram of ATLAS software. Note that the user can extract information to perform analyses at any of the three major software outputs. Also, ATGEN is an interface to many generators, too many to include in the diagram.

For the generation of events with physics generators, ATGEN [21] is used. ATGEN is an interface to several powerful Monte Carlo generators including PYTHIA [22], JETSET [22], VECBOS [23], HERWIG [24], NJETS [25], ISAJET [26] and ISASUSY [26]. In addition to producing the four-vectors to be used for a full simulation study, its built-in analysis routines allow for easy completion of particle level studies. These particle level analyses can provide an important check on the four-vectors before time-consuming full simulation studies are undertaken.

The standard CERN package for simulating the passage of radiation through matter is GEANT [27], which allows for the simulation of many different materials and geometries as well as most physical processes relevant to the passage of particles through a detector. For instance, particles or jets produced by a physics generator can be passed into GEANT which will then generate showers, form jets or simulate

other behaviour expected in a real detector. Yet, in the ATLAS software environment, GEANT does not work alone. The DICE [28]/SLUG [29] interface has been designed for ATLAS GEANT users. This interface contains several versions of ATLAS geometries which can be invoked with little or no programming by the user. They also allow the addition of new detector geometries in the same fashion as GEANT. Finally, DICE/SLUG controls the ZEBRA* memory management for GEANT.

After the event has been processed by DICE/SLUG the data is passed into ATRECON, which handles the reconstruction of the simulated data. This package is responsible for calibration and noise addition for each ATLAS subdetector. ATRECON is the package in which all of the final physics analysis is performed. For example, this package has jet finding routines already built-in, and others are easily added to attempt reconstruction of Higgs boson signals in the end-cap region.

3.3 Effects of Pile-up with Different End-Cap Configurations

It is expected that the addition of pile-up effects (as defined in the following section) will make ATLAS calorimetry design goals more difficult to achieve. Therefore, it is important to optimize the design of the end-cap to minimize the effects of pile-up. At the same time, software techniques, including energy cuts, should be used in an attempt to reduce pile-up in standard designs.

This study aims to produce effective software techniques to reduce pile-up effects both in the standard technical proposal end-cap configuration, as well as using

*ZEBRA is a CERN package used by GEANT and other CERN library programs to manage memory and allow them to use dynamic data structures

extensive Monte Carlo simulation techniques to change the longitudinal segmentation of the end-cap in a further attempt to achieve optimum resolution in the presence of pile-up. The choice of end-cap configurations was made based on [19]. This study is designed to emulate the previous work of [19] but with the inclusion of pile-up effects.

The standard (technical proposal) configuration of the hadronic end-cap uses 56 copper plates, each 2.5cm thick, grouped into 4 readout segments in depth. The first 8 plates form the first readout segment, while the next three segments contain 16 plates each. This configuration is represented as 8/16/16/16. Other configurations containing 56 2.5 cm plates considered here include: 1 segment 56 plates, 2 segments 24/32, 3 segments 16/16/24 and 8/16/32. The performance of each of these configurations will be examined in detail in this section.

3.3.1 What is Pile-up?

As the ATLAS detector is designed to operate in an extremely high luminosity environment, each bunch crossing will result in the production of, on average, 23 minimum bias events. The production of many of these minimum bias events over many bunch crossing leads to energy "piling-up" in the detector. A minimum bias event is defined, for the purposes of this study, as including the following PYTHIA processes: ISUB = 11, 12, 13, 53, 68. These processes are described in Table 3.1.

A signal of interest is expected approximately once every 23 bunch crossings at ATLAS and so, about every 500 ns an "interesting" physics signal (a signal containing a high P_T interaction) will occur. Yet, a burst of minimum bias particles can be expected every 25ns. This leads to minimum bias energy "piling-up" in the detector between physics signals. This is a particularly dangerous effect at high η, where most of the minimum bias energy is deposited. The presence of pile-up would be

Process Number (ISUB)	Process Type
11	$f_i f_j \rightarrow f_i f_j$
12	$f_i \overline{f_i} \rightarrow f_k \overline{f_k}$
13	$f_i \overline{f_i} \rightarrow gg$
53	$gg \rightarrow f_k \overline{f_k}$
68	$gg \rightarrow gg$

Table 3.1: This table contains the PYTHIA processes used to define a minimum bias event in this study. In this table *f* represents a fermion (quark or lepton) while g represents a gluon. The indices indicate flavour (6 flavours of quarks, 6 types of leptons).

expected to result in an over-estimation of the physics signal energy and a widening of the signal peak due to the width of the minimum bias energy peak (ie. energy fluctuations in minimum bias events). However, this problem of over-estimating the energy of a signal can be severely reduced by "bi-polar shaping" the detector signals.

An example of a shaping function is given in Figure 3.2. Shaping is done in order to increase the speed of response of the calorimetry. Without shaping, the signal from a LAr gap (for example) would decay very slowly (as the straight line (a) in Figure 3.2), shaping the signal provides a means to attenuate the decay of a signal and minimize the sum of electronic and pile-up noise [1]. This shaping function spans all 23 bunch crossings expected to occur between events of interest. It integrates to zero, with the physics signal occurring, ideally, when the function's value is 1. This has the effect of leaving the signal energy unchanged, while altering the minimum bias energy so that it is centred around 0. In this way, the pile-up is prevented from affecting the mean energy of the signal, however, the RMS value of this signal will still be affected.

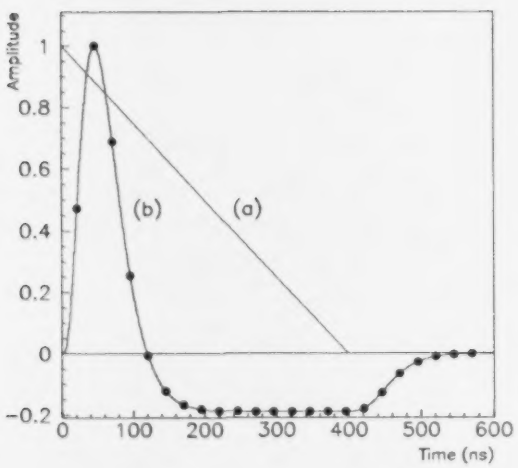

Figure 3.2: The shaping function of the ATLAS hadronic end-cap calorimeter. The horizontal axis represents time (0-475ns), while the vertical axis represents the factor by which the detector energy will be scaled. The straight line (a) indicates the drift current vs. time for an ionization calorimeter. The characteristic shaping time for this particular shaping function is $t_p(\delta) = 20$ ns.

In other words, a 100 GeV jet will still appear to contain 100 GeV of energy, but the uncertainty of this measurement will be increased. An example illustrating this effect is provided in Figure 3.3. This decrease in signal energy resolution is what makes the reduction of pile-up an important issue in end-cap calorimeter design, particularly for relatively soft jets (50 GeV-100 GeV).

3.3.2 Calibration

The first step necessary in order to get energy resolution results is to determine calibration constants for the end-cap region. These calibration constants serve two main functions. The first is to allow the reconstruction of jet energy from calorimeter energy. A sampling calorimeter detects only a small fraction of the total particle energy entering the detector and so a calibration constant is necessary to reconstruct the true energy. The second function is to perform a type of software compensation[†] for the calorimeter. By separately weighting the different depth compartments of the calorimeter a more uniform calorimeter response can be achieved. For instance, energy from a high energy jet might have a tendency to leak out of the back compartment of the hadronic calorimeter. In this situation, the last compartment of the calorimeter might be weighted more heavily than the other compartments in order to compensate for this effect. To determine these calibration constants, the method presented in [19] was used. In this method, the energy in the i^{th} event is defined by:

$$E_i = \sum_{j=1}^{M} C_j \times E_{ij} \tag{3.1}$$

where E_{ij} is the energy deposited in the j^{th} calorimeter division in the i^{th} event, C_j are the calibration parameters and M is the number of longitudinal segments to be

[†]a compensating calorimeter has the same response for electrons and pions

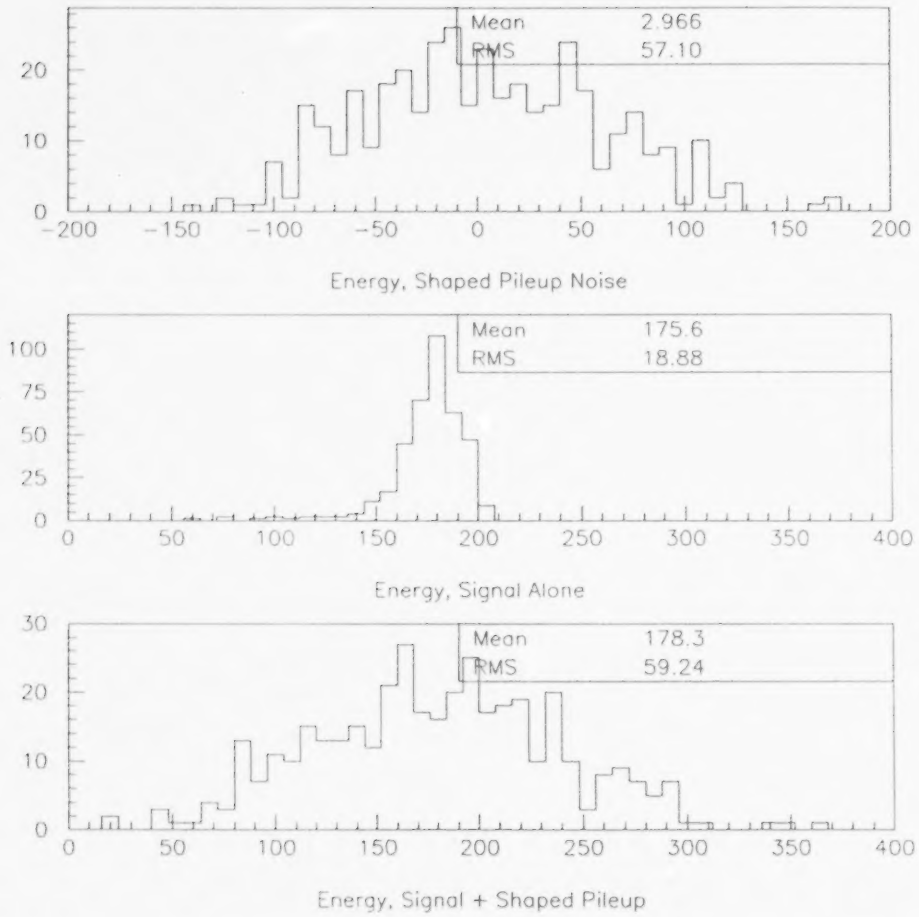

Figure 3.3: The first energy histogram shows the shaped pile-up noise due to minimum bias background, the second histogram shows a signal before the addition of shaped pile-up, the third shows this signal after the shaped pile-up has been added event by event (it cannot be obtained by simply adding together the first two plots) in the end-cap region. Note: Once cuts have been made to reduce the effects of pile-up, the picture above improves considerably, as will be shown in the chapters to come.

given different calibration constants. The calibration parameters are then determined by minimization of the functional:

$$F = \sum_{i=1}^{N} \left(E_i - E_i^{jet} \right)^2 \tag{3.2}$$

where E_i^{jet} is the energy of the jet in the ith event and N is the number of events.

For the purposes of this study, there were 3 calibration parameters for the EM end-cap and between 1 and 4 constants for the hadronic end-cap depending on the configuration. So, for example, in the standard longitudinal configuration of the end-cap (8/16/16/16) there would be 7 different calibration parameters, one for each longitudinal segment. Also, a different set of calibration parameters is required for each energy value (eg. a 700 GeV jet needs different calibration constants than a 200 GeV jet would). An example of the calibration constants is given in Table 3.2 for 200 GeV jets. These calibration constants are obtained for an $R = 0.5$ cone, where R is defined as:

$$R = \sqrt{\Delta\eta^2 + \Delta\phi^2}. \tag{3.3}$$

The reconstructed energy from these calibration constants (200 GeV, 0.5 cone) has a resolution of $\sigma/\mu = 4.85\%$ (σ is the width of the distribution while μ is the mean).

3.3.3 Reconstruction

Once the calibration constants have been obtained, it is necessary to reconstruct the signal. In the reconstruction stage of this analysis, the DICE geometry package was again used. This package was chosen over the standard ATLAS reconstruction package, ATRECON, due to the fact that the current hadronic end-cap design is not yet well implemented in the ATRECON package. So, to reconstruct events in the

Depth Segment	Calibration Constant
1	6.37
2	5.19
3	7.32
4	39.36
5	35.01
6	32.21
7	47.42

Table 3.2: This table contains the calibration constants for each of the seven depth segments in the end-cap calorimeter. The first three segments are part of the EM calorimeter, the last four are hadronic segmentations.

latest end-cap geometry (technical proposal version), a modified version of DICE had to be used in cooperation with stand-alone code.

The first piece of code required to perform the reconstruction is a version of DICE modified to read out the detector hits (energy deposits in a simulated detector cell) from hit banks in the ZEBRA file outputted by the simulation. Separate versions of this code were written for the signal and pile-up simulations. The DICE code for signal analysis simply reads out the detector hits and writes the eta, phi, z and energy values of each cell in a specified cone to a text file. The DICE code for pile-up analysis performs a similar function, outputting a text file in an identical format to the signal text file. The main difference for the pile-up code is that the energy from minimum bias events are combined to form bunch crossings. In other words, an average of 23 minimum bias events are combined into a single bunch crossing at this stage and the energy in each cell written to the text file is the energy per bunch, rather than the

energy per minimum bias event.

The next stage in the reconstruction process is the shaping of the pile-up events. This shaping is performed in a piece of stand-alone code which chooses a random set of 23 bunch crossings from the text file produced by the DICE pile-up analysis code and applies a shaping function to the energies in this event. This stand-alone code then produces a text file containing the shaped energies for each read-out cell.

Finally, the signal and pile-up events must be merged and calibration constants must be applied. In order to do this, another piece of stand-alone code was written. This code reads the energy per cell from the signal and shaped pile-up text files and merges the energies on a cell by cell basis. It then applies calibration constants to the energies and produces an HBOOK[‡] file containing the reconstructed energies with and without pile-up for each jet event.

3.3.4 Results

Figure 3.4 shows a plot of a comparison of the σ/E, where E is the energy, of the signal, signal+pile-up, and signal+pile-up with a 1 GeV E_t cell cut (ie. all cells containing less than 1 GeV E_T are removed). The points on this plot were obtained by fitting a Gaussian to the energy distribution histograms of jets at several different energy points. The σ of this Gaussian fit divided by its mean is a measure of the energy resolution of the calorimeter at a particular energy. There are 700 events at each of 5 energy points (40,100,200,500,800 GeV). The five energy points are fitted to the form:

$$\sigma/E = P1/\sqrt{E} \oplus P2 \tag{3.4}$$

[‡]HBOOK is a fortran callable package for histogramming

giving a sampling and constant term which appear on the plot as P1 and P2. This plot is for the configuration in which the hadronic end-cap is made up of only one depth division, consisting of 56 copper plates. These results were also obtained using the four other end-cap configurations. Figure 3.5 shows a direct comparison of the energy resolution for each of the simulated configurations on the same axis. Figure 3.6 is the same plot after a 1 GeV E_t per tower (a tower refers to a sum of all cells in depth at a particular value of η and ϕ) cut has been applied. Finally, in order to compare the resolution of the calorimeter with pile-up and tower cuts applied to the situation where no pile-up exists, Figure 3.7 shows the energy resolution of the calorimeter for 5 different configurations (56, 24/32, 16/16/24, 8/16/32, 8/16/16/16) without pile-up.

3.3.5 Conclusions

The study of the effects of pile-up in each of five different configurations (56, 24/32, 16/16/24, 8/16/32, 8/16/16/16) has illustrated that none of these configurations differ significantly from one another in terms of energy resolution except for a small difference at low energy. This result confirms earlier work [19] on energy resolution without the inclusion of pile-up effects. These studies lead to the conclusion that any of the possible configurations of the hadronic end-cap consisting of 2.5 cm copper plates is satisfactory and that the ganging of the plates in depth has little bearing on energy resolution.

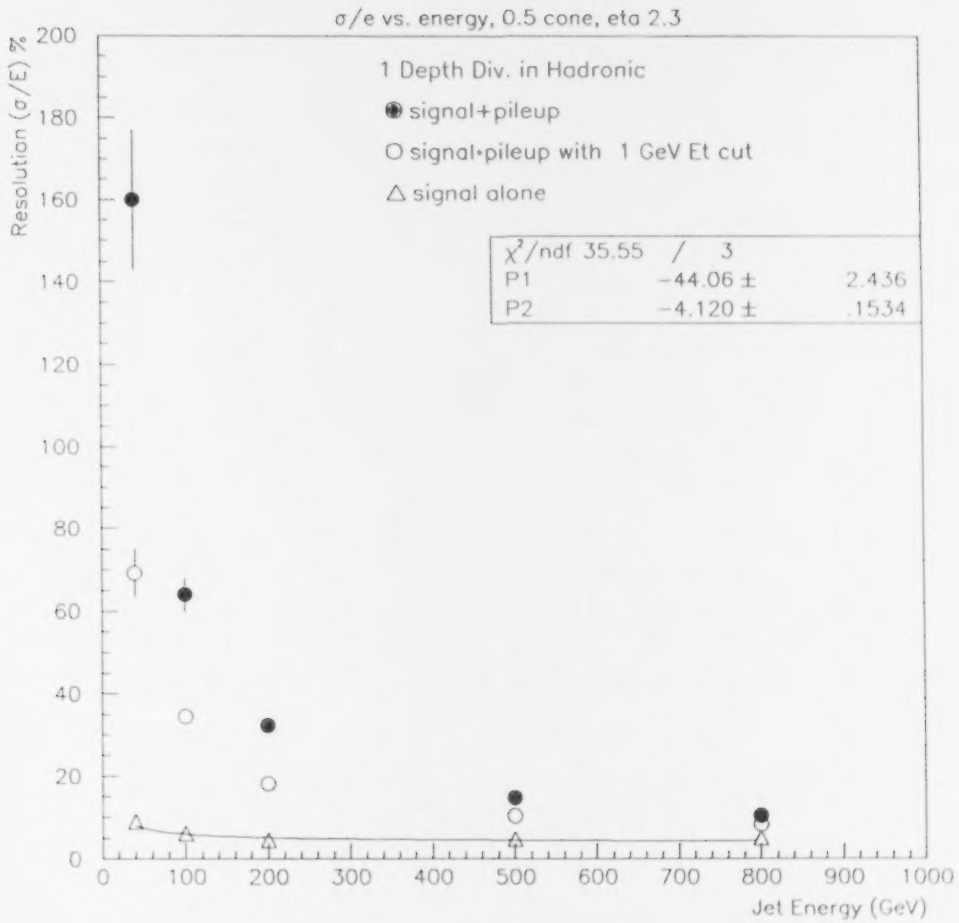

Figure 3.4: Energy resolution with pile-up is plotted against jet energy for a 0.5 cone at $\eta = 2.3$ for the end-cap configuration which contains only one depth division consisting of 56 copper plates.

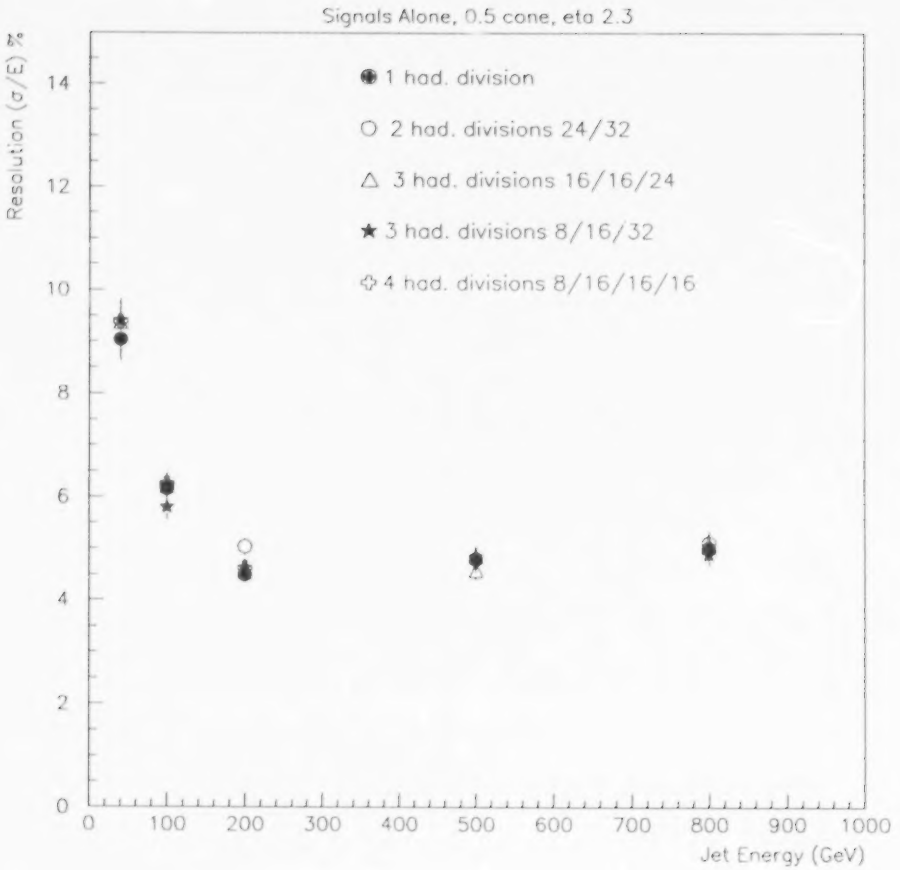

Figure 3.5: Energy resolution with pile-up is plotted against jet energy for a 0.5 cone at $\eta = 2.3$ for 5 different end-cap configurations.

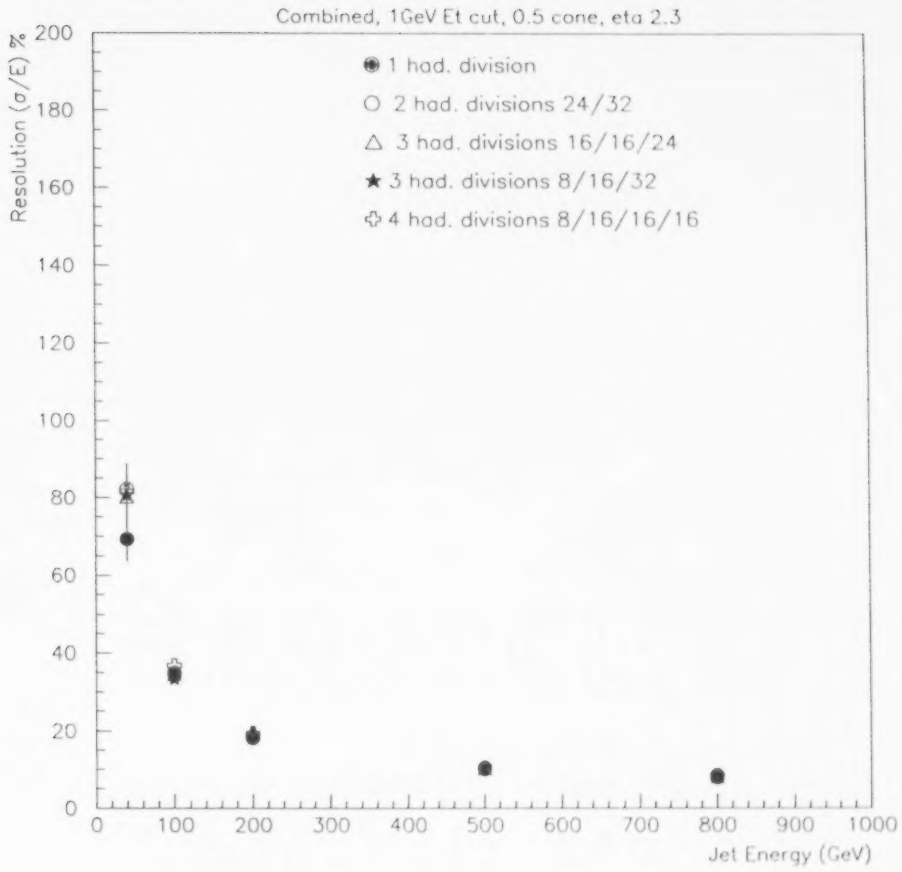

Figure 3.6: Energy resolution with pile-up is plotted against jet energy for a 0.5 cone at $\eta = 2.3$ for 5 different end-cap configurations with a 1 GeV E_t cut.

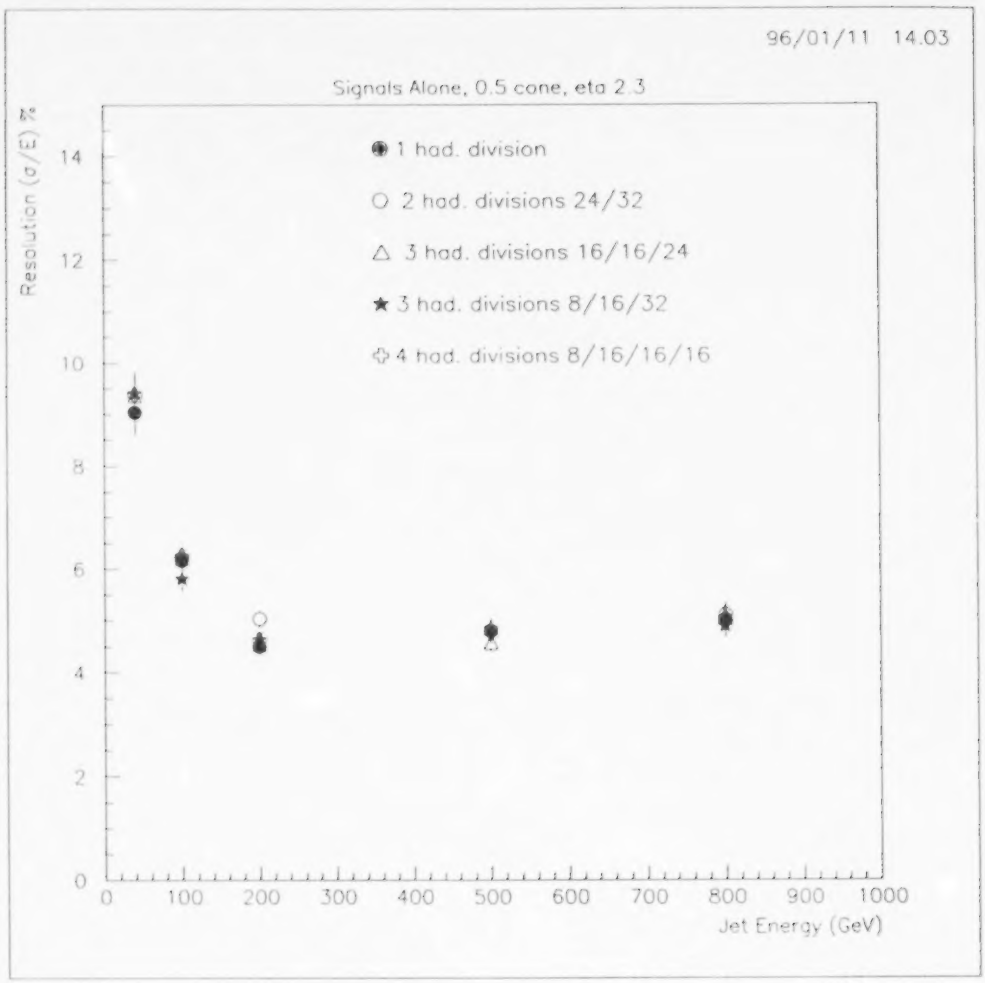

Figure 3.7: Energy resolution is plotted against jet energy for a 0.5 cone at $\eta = 2.3$ for 5 different end-cap configurations.

3.4 Study of Changing Granularities in the Hadronic End-Cap

3.4.1 Introduction

The technical proposal hadronic end-cap granularity is 0.05×0.1 below $\eta = 1.8$, and 0.1×0.1 at all other values of η. It has been suggested at CERN hadronic end-cap meetings that the granularity of the hadronic end-cap be changed to 0.2×0.2 in η/ϕ for $\eta > 2.4$[§] . This geometry change would lead to a reduction in the number of readout cells in the hadronic end-cap, producing a cost savings. To test the effect of this change on energy resolution in the presence of pile-up, two η positions,$\eta = 2.5$ (near edge of granularity change region) and $\eta = 2.8$ (near edge of calorimeter), were considered in the end-cap region.

In order to test the proposed granularity change, 500 $d\bar{d}$ di-jets were generated using ATGEN/PYTHIA at transverse energies of 40, 60, 80, 100, 120, and 180 GeV at $\eta = 2.5$ and passed through DICE 1.09 using GEANT 3.2130. The value of $\eta = 2.5$ was chosen because it is near the edge of the region affected by the granularity change. Similarly 500 $d\bar{d}$ di-jets were generated at $\eta = 2.8$, the centre of the affected region, at energies of 100, 200, 500, and 800 GeV. The geometry used was TP3[¶] standard except for the removal of the end-cap preshower and addition of a detailed hadronic end-cap module.

Pile-up noise was simulated in the same geometry using minimum bias events

[§]This change has now been adopted by ATLAS, since it has been shown here and in [19] that it is an acceptable change

[¶]TP3 refers to a particular version of the simulated ATLAS geometry, agreed upon by the simulation group. This particular version of the geometry is the last one implemented in the standard DICE framework (all newer geometries are being integrated into DICE3, a new simulation package)

(PYTHIA processes defined in Table 3.1) from ATGEN/PYTHIA. A Poisson mean of 23 minimum bias events per bunch crossing was used and a total of 23 bunch crossings were convolved with the proper shaping function to create each pile-up event. A detailed description of the method of pile-up inclusion is given in Section 3.3.3.

Calibration for each energy and η position was performed by minimization of the mean square error between the generator jet energy and the reconstructed energy using the signal jets alone as described in Section 3.3.2. However, in this case the calibration technique is applied in an iterative way. After the first pass, only reconstructed jets which lie within 3σ of the mean reconstructed energy are used for the second pass calibration. The algorithm ceases iterating when the difference between the results of the previous two passes falls below a set threshold (eg. the standard deviation on the energy measurement changed by less than 1%). The calibration constants obtained via this technique are then applied to the entire sample of jets to obtain the energy resolution. This technique was adopted in order to provide a more stable set of calibration constants (ie. not subject to effects of pathological events). It turns out, however, that this calibration technique offers no significant advantage as compared to the one-pass technique presented earlier.

3.4.2 Results

In this study, the energy resolution of the end-cap calorimeters was compared for a ΔR=0.5 cone for the coarse and fine grained hadronic calorimeter. A cell was included in the jet if its centre fell within a ΔR=0.5 cone of the jet axis. Therefore, this 0.5 cone would contain a different area depending on the granularity of the cells within the cone. For example, at $\eta = 2.5$, a 0.5 cone contained roughly 7% more 0.1×0.1 cells in the coarse grained (0.2×0.2 above $\eta = 2.4$) as in the fine grained case.

Layer	1	2	3	4	5	6	7
E_t Cut (GeV)	0.51	0.31	0.18	0.27	0.17	0.043	0.0152

Table 3.3: Transverse energy cut per 0.1×0.1 cell in each layer of the end-cap for an integrated cut of 1.5 GeV over a 0.1×0.1 η/ϕ tower. The cut in the 0.2×0.2 η/ϕ cells will be 4 times these amounts.

Three pile-up-inclusive situations were examined to determine the effect of the granularity change on energy resolution. The first situation involved including pile-up with the jet signals with no cuts to reduce pile-up effects. In the second, a cell was required to have greater than 0 GeV to be considered in the energy sum. Due to the effect of shaping, this cut would be expected to remove approximately half of the cells containing only pile-up without affecting the signal. The last situation involved a z dependent cut and consisted of an integrated cut of 1.5 GeV in E_t across each 0.1×0.1 η/ϕ tower. The actual cut in each of the seven layers of the end-cap was modulated by the RMS of the pile-up in that layer. The resulting cut is shown in Table 3.3. The resulting energy resolution points for the $\eta = 2.5$ case may be seen in Figures 3.8, 3.9, 3.10 and 3.11 for the various cuts. No significant difference in the energy resolution in the presence of pile-up is seen between the 0.1×0.1 η/ϕ granularity and the 0.2×0.2 η/ϕ granularity.

These same three situations were also considered for the $\eta = 2.8$ case. However, this η value presented some problems which distinguished it from the $\eta = 2.5$ case. Since the jets were near end-cap/forward crack, the 0.5 cone included some cells of the forward calorimeter. The forward calorimeter was calibrated separately, using $d\bar{d}$ events at $\eta = 4.0$ and its pile-up signal was shaped with the hadronic end-cap shaping function. However, since very few cells from the forward are included in a 0.5 cone

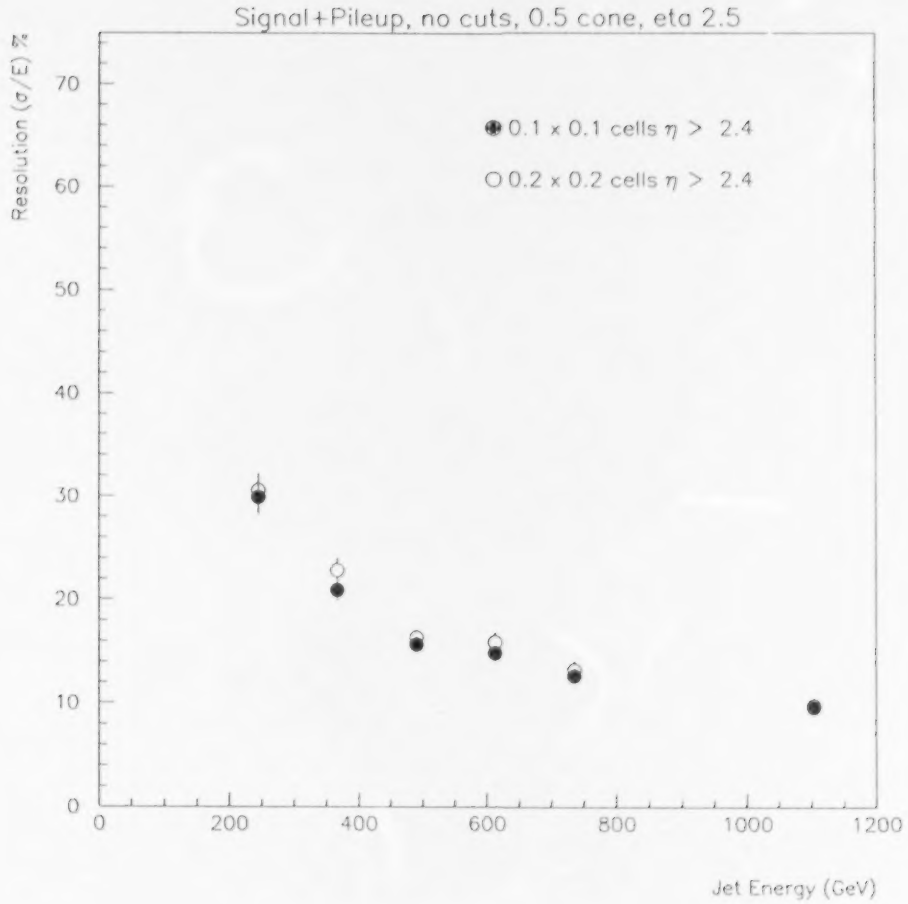

Figure 3.8: Energy resolution of jets at $\eta = 2.5$ in the presence of pile-up with no cell cut on the energy distributions. The results for the 0.1×0.1 η/ϕ granularity are shown by the open circles and those for the 0.2×0.2 η/ϕ geometry by the filled circles.

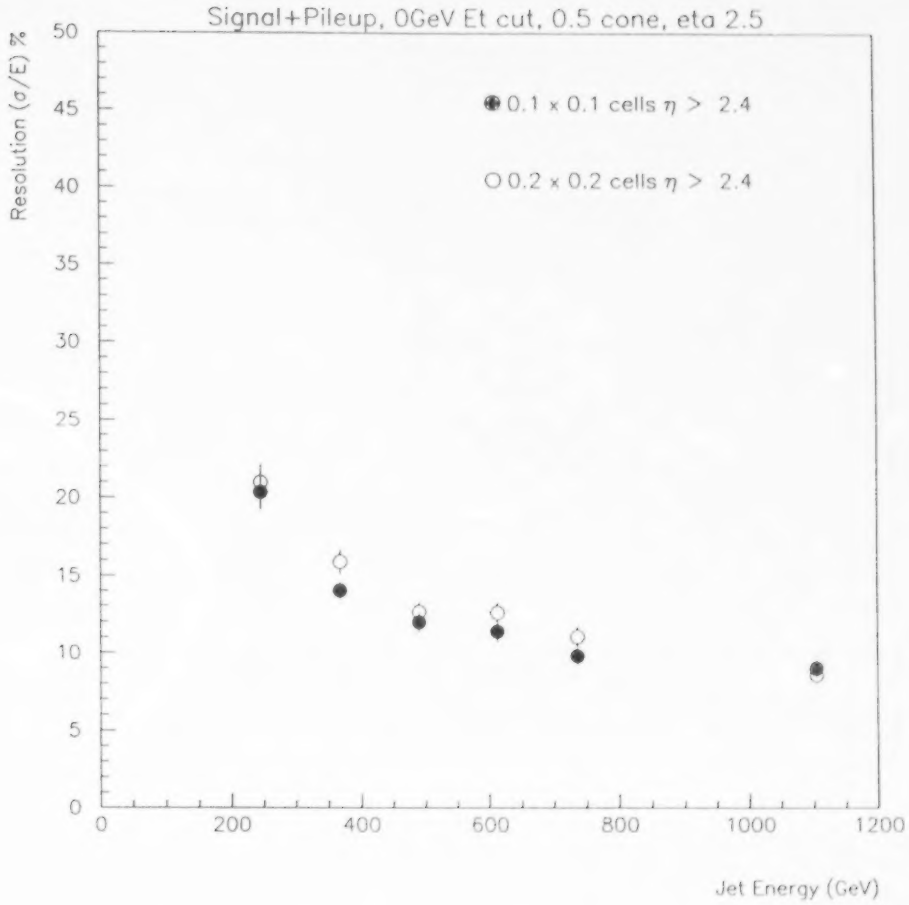

Figure 3.9: Energy resolution of jets at $\eta = 2.5$ in the presence of pile-up with a 0 GeV transverse energy cell cut on the energy distributions. The results for the 0.1×0.1 η/ϕ granularity are shown by the open circles and those for the 0.2×0.2 η/ϕ geometry by the filled circles.

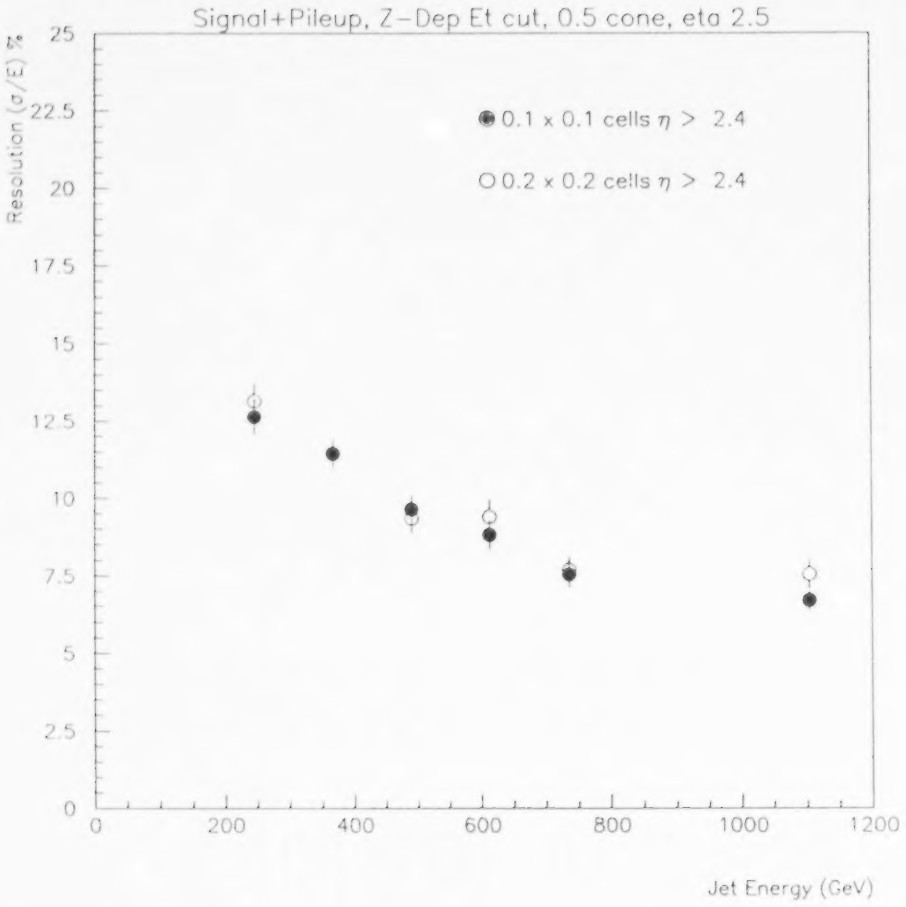

Figure 3.10: Energy resolution of jets at $\eta = 2.5$ in the presence of pile-up with a 1.5 GeV cut per $0.1 \times 0.1 \eta/\phi$ tower transverse energy cell cut on the energy distributions. The results for the 0.1×0.1 η/ϕ granularity are shown by the open circles and those for the 0.2×0.2 η/ϕ geometry by the filled circles.

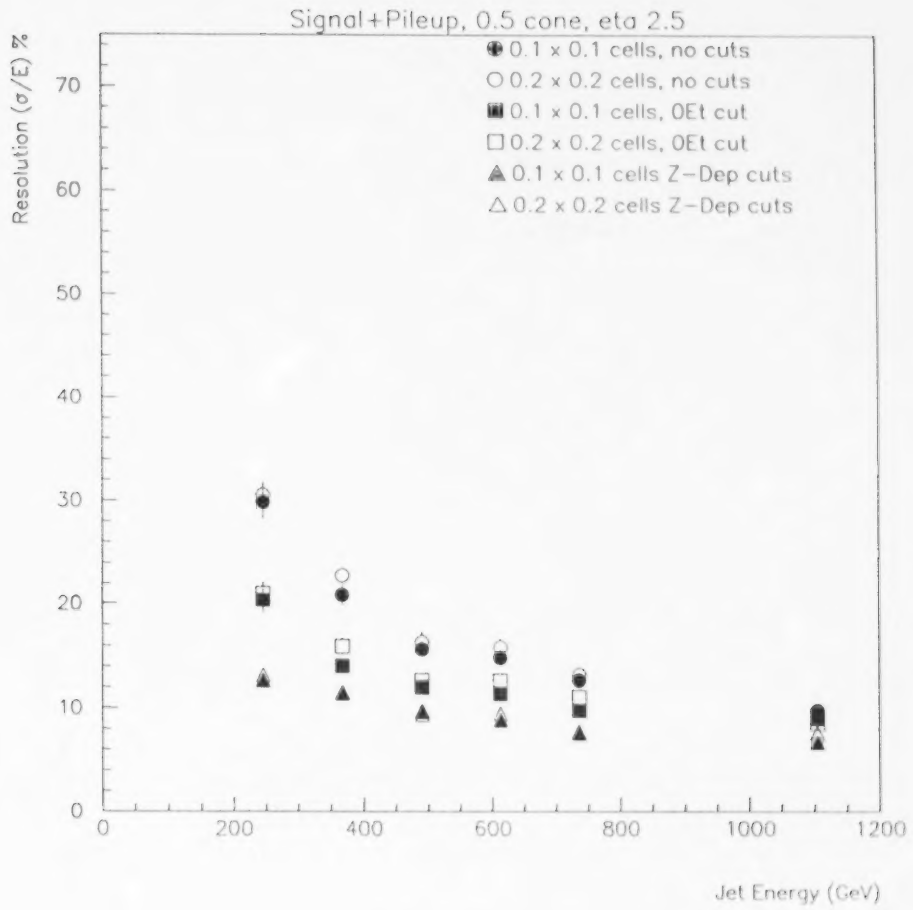

Figure 3.11: Energy resolution of jets at $\eta = 2.5$ in the presence of pile-up with and without transverse energy cuts for both hadronic end-cap granularities.

centred about $\eta = 2.8$ the energy content of the forward had a very small effect.

The same two cuts applied to the $\eta = 2.5$ data were applied to the $\eta = 2.8$ data as well. The only difference was that in this data sample a cut must also be applied to the few forward calorimeter cells included in the 0.5 cone. For both sets of cuts (0 GeV E_t and Z-dependent E_t), a 0 GeV E_t cut is applied to the forward cells.

The resulting energy resolution points may be seen in Figures 3.12, 3.13, 3.14 and 3.15 for the various cuts. Little difference in the energy resolution in the presence of pile-up is seen between the 0.1×0.1 η/ϕ granularity and the 0.2×0.2 η/ϕ granularity cases. However, at lower energies a difference is noticeable when a 0 GeV E_t cut is applied.

3.4.3 Conclusions

This study of a proposed change in end-cap granularity above $\eta = 2.4$ has illustrated that at $\eta = 2.5$ the proposed change has no significant effect on jet energy resolution. At $\eta = 2.8$, however, some of the energy points appear to be affected by the granularity change. This effect is small and only appears at lower energies (it is virtually eliminated by the z-dependent cut). However, even in this energy regime, the effect of the granularity change appears from these results to be negligible in terms of energy resolution.

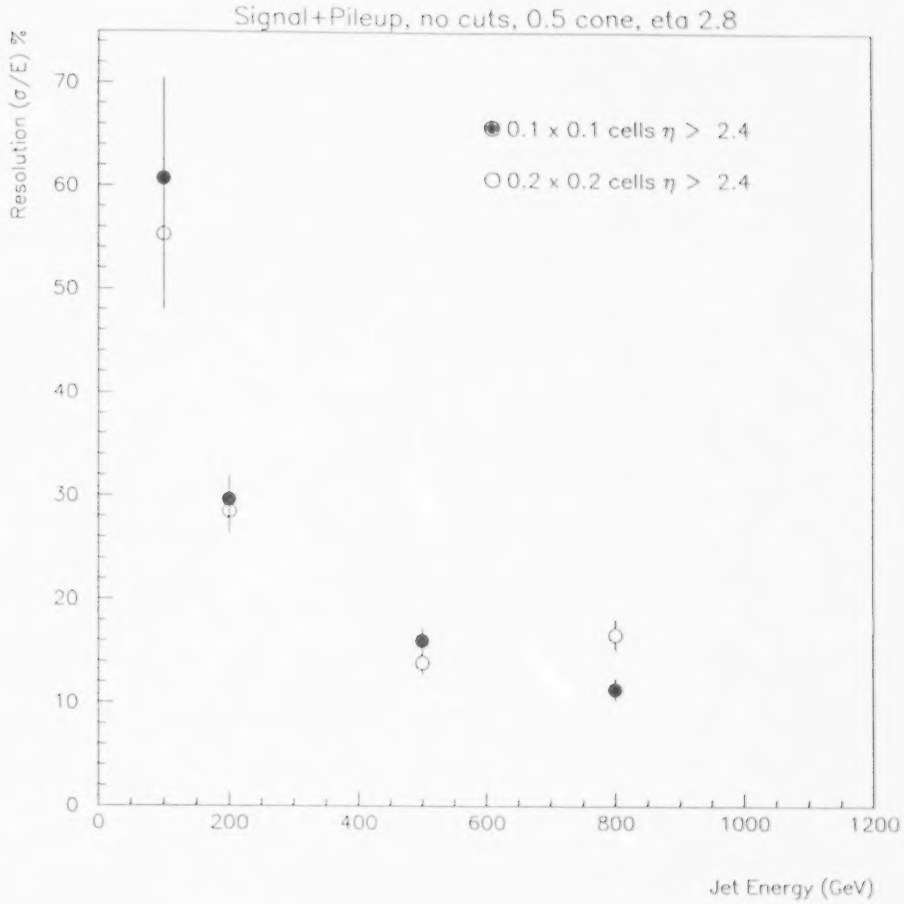

Figure 3.12: Energy resolution of jets at $\eta = 2.8$ in the presence of pile-up with no cell cut on the energy distributions. The results for the 0.1×0.1 η/ϕ granularity are shown by the filled circles and those for the 0.2×0.2 η/ϕ geometry by the open circles.

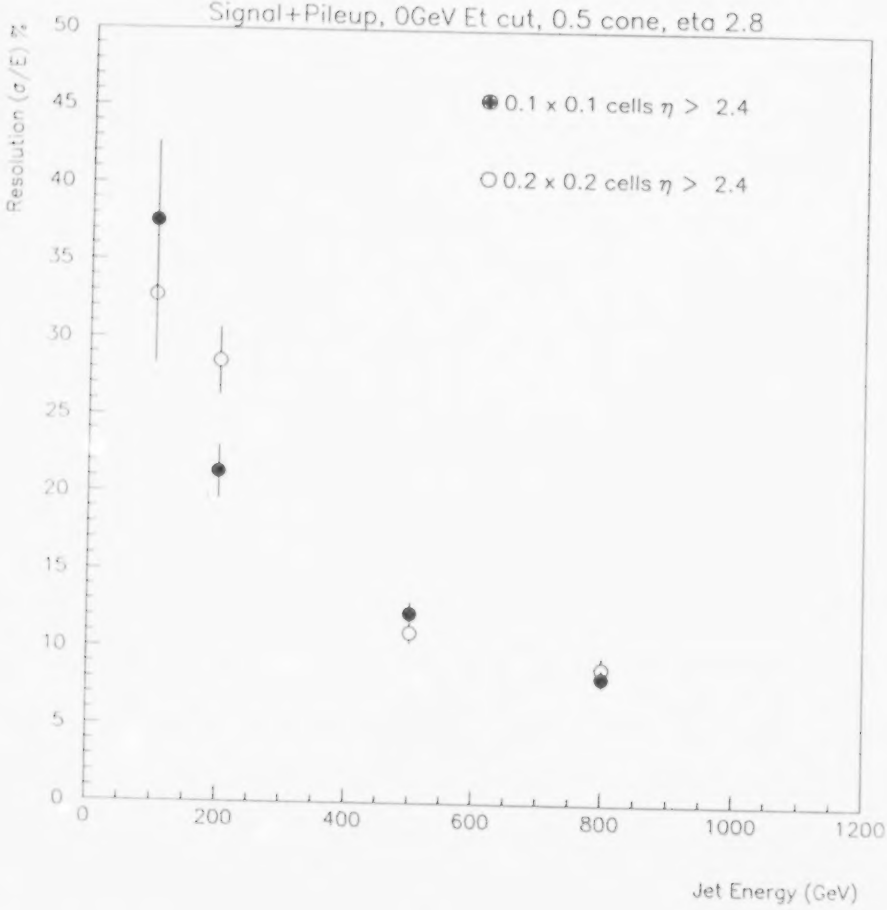

Figure 3.13: Energy resolution of jets at $\eta = 2.8$ in the presence of pile-up with a 0 GeV transverse energy cell cut on the energy distributions. The results for the 0.1×0.1 η/ϕ granularity are shown by the filled circles and those for the 0.2×0.2 η/ϕ geometry by the open circles.

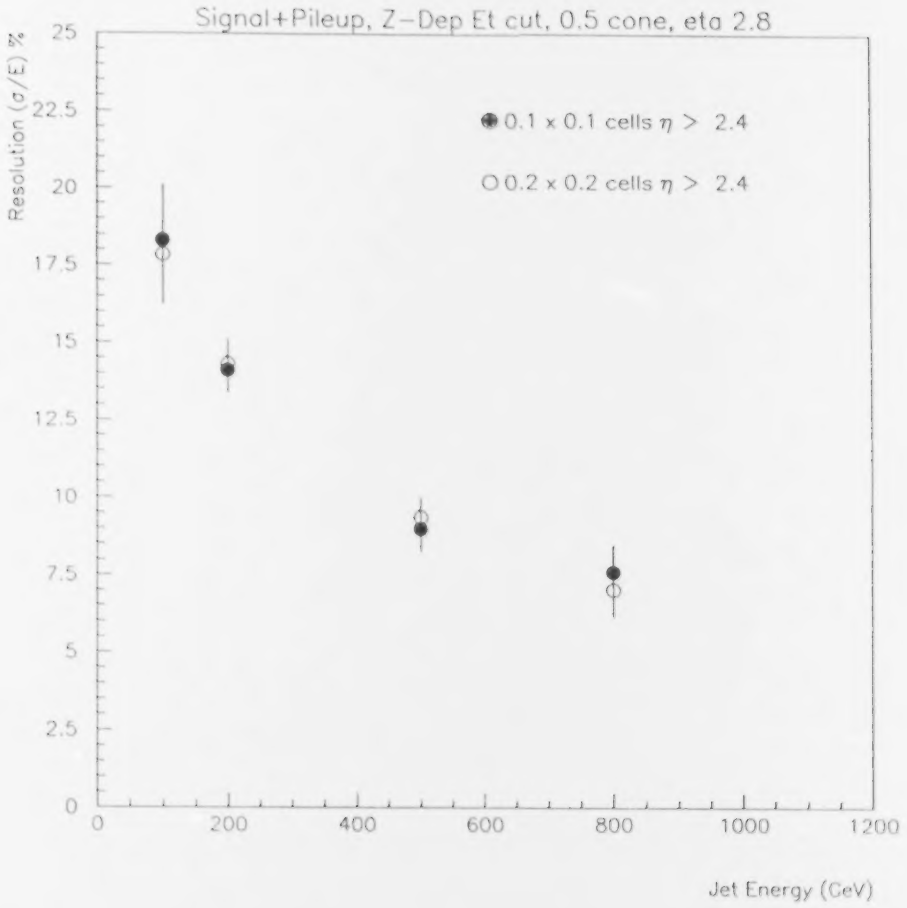

Figure 3.14: Energy resolution of jets at $\eta = 2.8$ in the presence of pile-up with a 1.5 GeV cut per 0.1×0.1 η/ϕ tower (see Table 3.3) transverse energy cell cut on the energy distributions. The results for the 0.1×0.1 η/ϕ granularity are shown by the filled circles and those for the 0.2×0.2 η/ϕ geometry by the open circles.

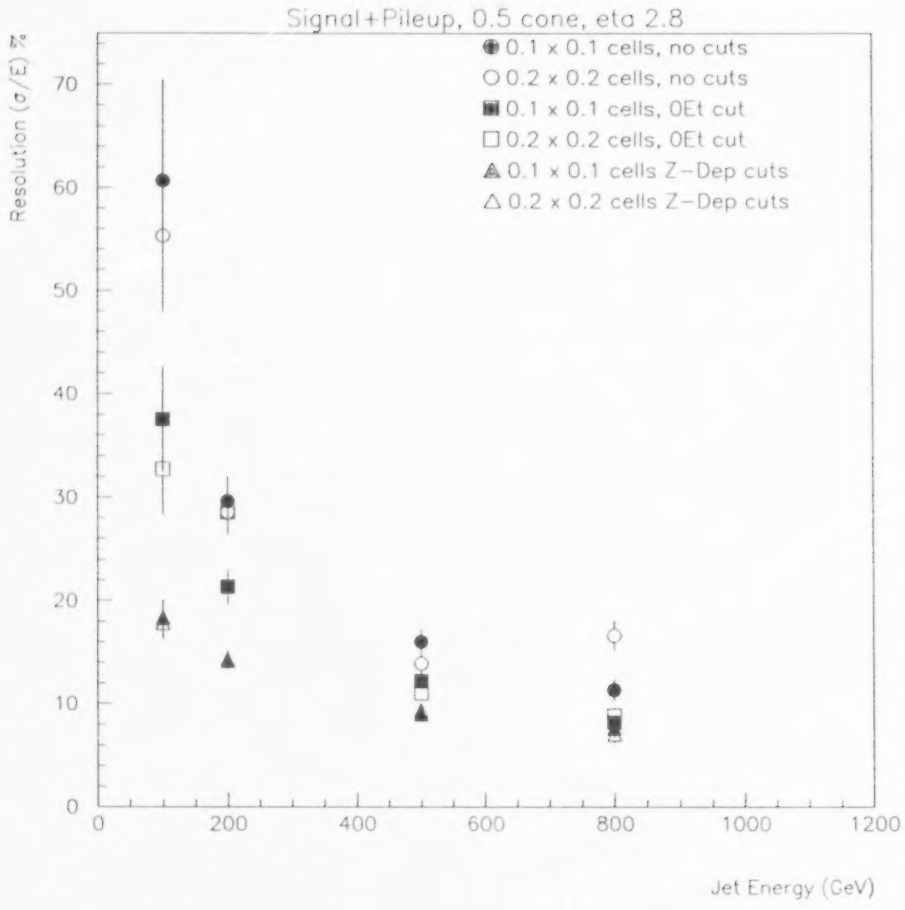

Figure 3.15: Energy resolution of jets in the presence of pile-up with and without transverse energy cuts for both hadronic end-cap granularities

3.5 Study of Plate Thickness Changes in the Presence of Pile-up

3.5.1 Introduction

The final end-cap geometry study presented here involves changing the standard end-cap geometry by increasing absorber plate thickness in the last two hadronic segments and considering the energy resolution. If this change is shown to provide acceptable energy resolution, the plate thickness doubling would provide a cost savings (less readout required). As in the previous studies, this is performed with and without pile-up effects. In order to perform this study, 500 $d\bar{d}$ dijets were generated using ATGEN/PYTHIA at transverse energies of 15, 40, 60, 80 GeV at $\eta = 2.3$ and passed through DICE 1.09 using GEANT 3.2130. The geometry used was TP3 standard except for the removal of the end-cap preshower and addition of a detailed hadronic end-cap module. Pile-up noise was produced and added to the signal in the same manner as the previous studies mentioned in this thesis.

In order to simulate the double thickness of copper plates in the back wheel of the calorimeter, the method of ATLAS-CAL-NO-083 [19] was used. In this method, only energy depositions from even numbered liquid argon layers are taken into account. This method does not precisely simulate the effect of doubling the thickness of the absorbers in the second wheel because of the presence of an extra liquid Argon gap between the two 2.5 cm copper plates which are effectively combined. However, the relatively low density of liquid Argon means that its influence on the effective thickness of the copper plates will be small and so, this method provides a reasonable approximation of a doubling of plate thickness.

3.5.2 Results

As in the earlier study of granularity changes in the end-cap, three pile-up-inclusive situations were examined to determine the effect of the plate thickness change on energy resolution. The first situation involved including pile-up with the jet signals when no cuts to reduce pile-up effects are applied. In the second, a cell was required to have greater than 0 GeV to be considered in the energy sum, while the last situation involves a z dependent cut and consisted of an integrated cut of 1.5 GeV in E_t across each 0.1×0.1 η/ϕ tower. The actual cuts in each of the seven layers of the end-cap was modulated by the RMS of the pile-up in that layer. The resulting cuts are shown in Table 3.3.

The resulting energy resolution without pile-up may be seen in Figure 3.16 while the equivalent plot from CAL-NO-083 [19] is shown in Figure 3.17. When pile-up is included, the results are shown in Figures 3.18, 3.19 and 3.20 for the various cuts. In agreement with CAL-NO-83 (which did not include the effects of pile-up), no significant difference in the energy resolution in the presence of pile-up is seen between the fine and coarse back compartment segmentations.

The differences in the values of σ/E between CAL-NO-083 and these results for the signal alone (no pile-up) are due to several factors. The first is that a different geometry was used in this study than was used in CAL-NO-083. This study was performed in the DICE-95 hadronic end-cap geometry (includes all gaps, cracks), while the results of CAL-NOTE-083 were obtained in an earlier, less detailed, end-cap geometry. The second difference is that all energy resolution results in this study are quoted for a 0.5 cone (due to the desire to include pile-up), while CAL-NO-083 includes the entire end-cap volume. The final difference is in the calibration. The use of different calibration constants means that the absolute numbers for the σ/Es in

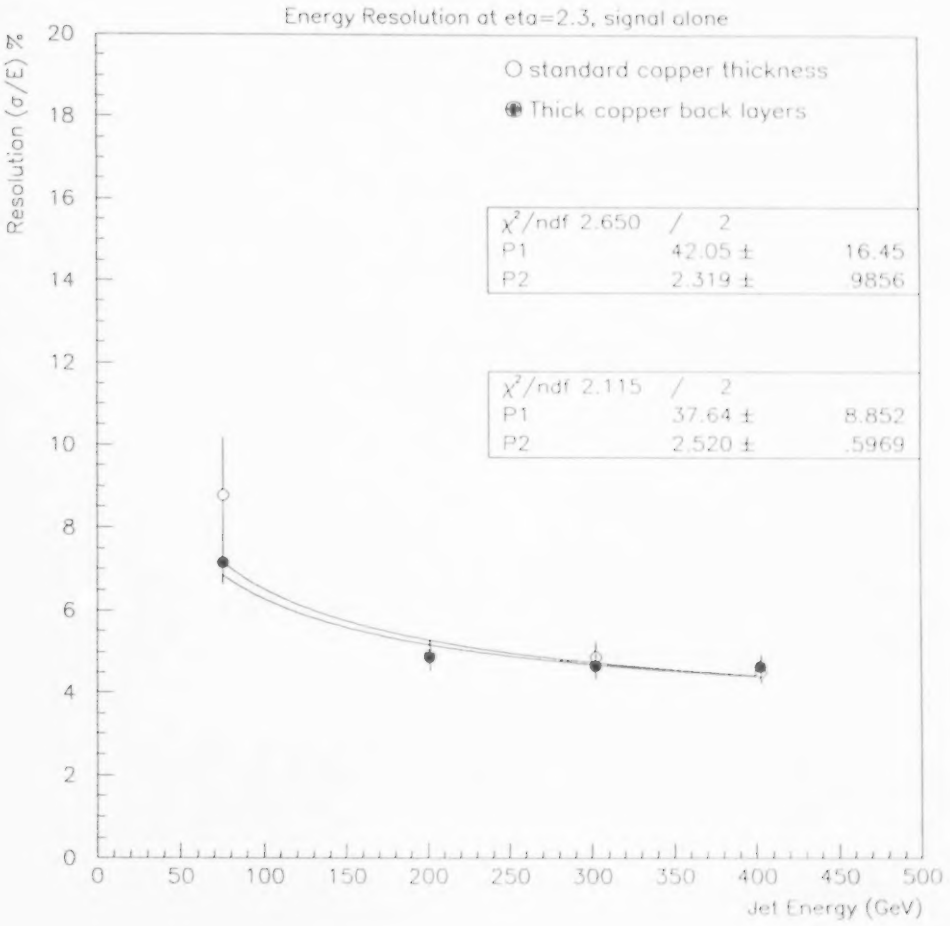

Figure 3.16: Comparison of thick and thin plates in the last two segments of the end-cap for jets of several energies.

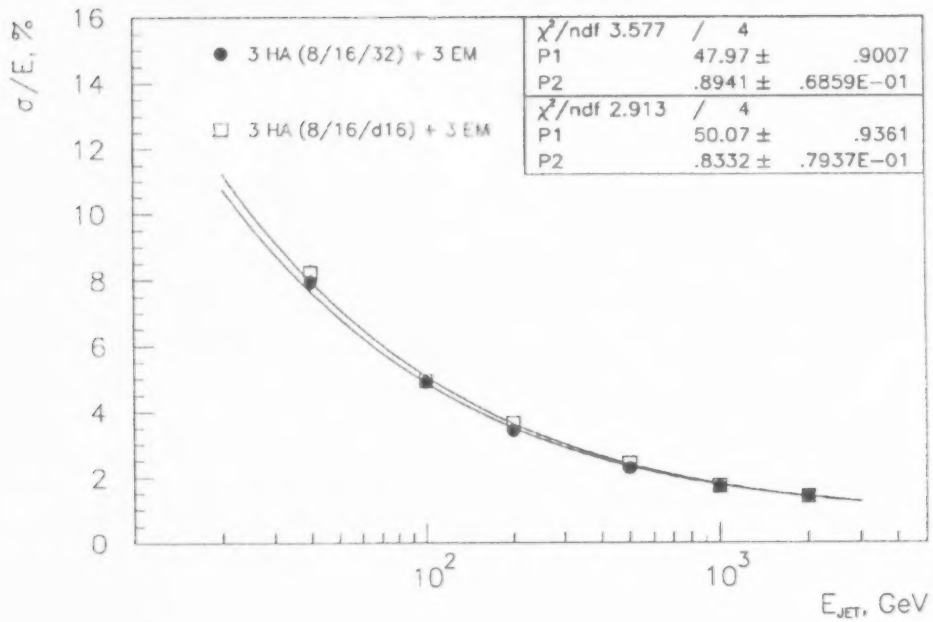

Figure 3.17: Energy resolution of jets from CAL-NO-083. The results for the 2.5mm copper plates in the last two segments are shown by the filled circles and those for the 5mm copper plates by the open circles.

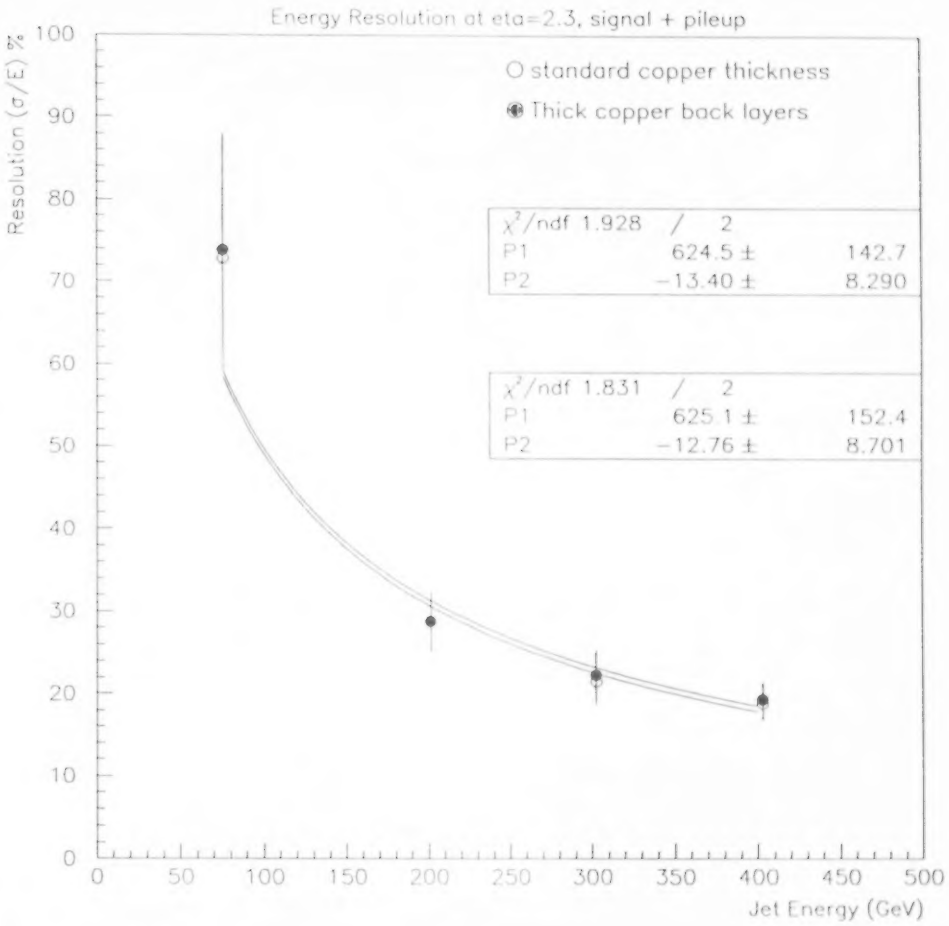

Figure 3.18: Pile-up-inclusive energy resolution **results for the 2.5mm copper plates in the last two segments are shown by the open circles and those for the 5mm copper plates by the filled circles.**

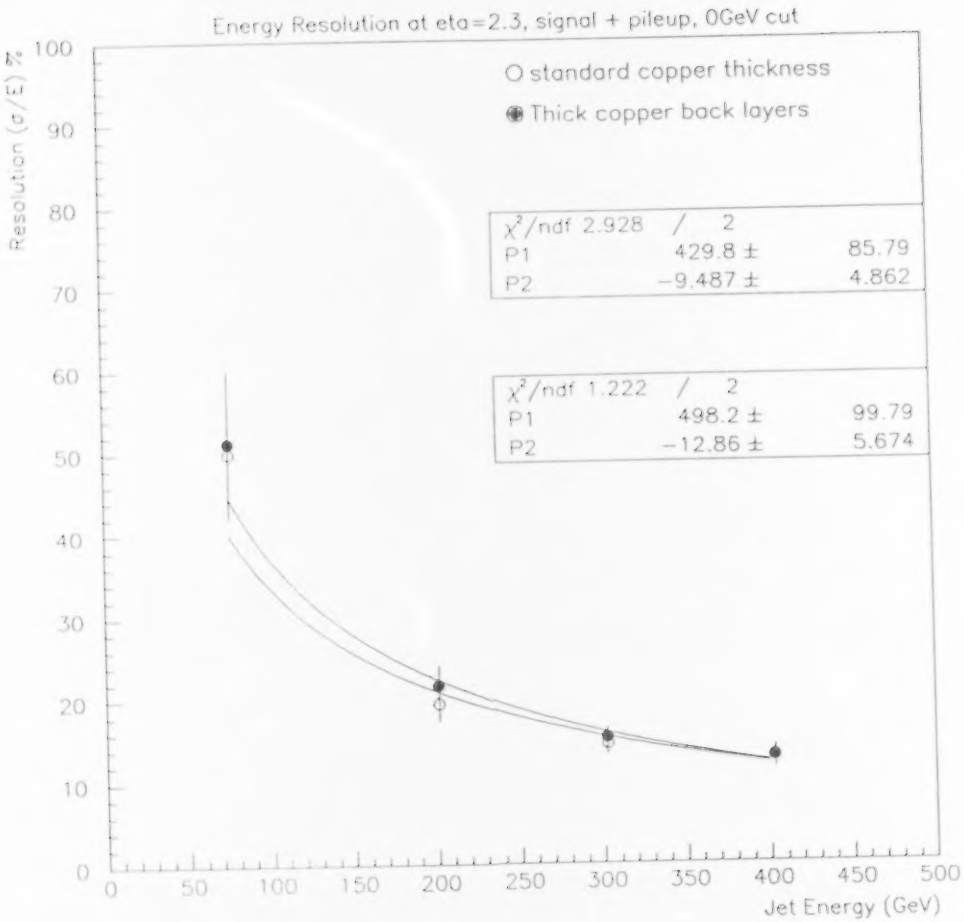

Figure 3.19: Energy resolution results for a 0 GeV E_t cut, thin plates in the last two segments are shown by the open circles and thick plates by the filled circles.

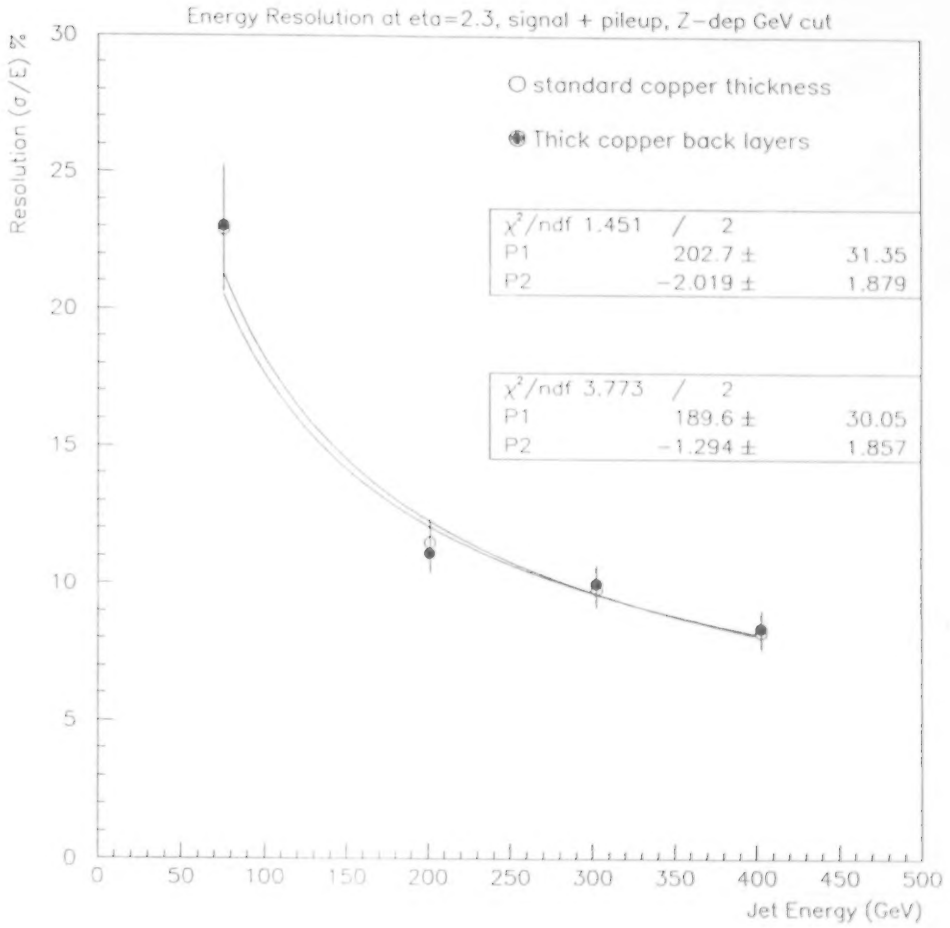

Figure 3.20: Energy resolution results for a Z-dependent E_t cut, thin plates in the last two segments are shown by the open circles and thick plates by the filled circles.

this study cannot be expected to agree exactly with the results of CAL-NOTE-083. However, despite these differences, the results should be similar and the conclusions of the two studies should be, and are found to be, the same.

3.5.3 Conclusions

The preceding study illustrates that a doubling of the plate thickness in the second wheel of the calorimeter will not have a significant effect on energy resolution whether or not pile-up effects are included. These results are in good agreement with the results of CAL-NOTE-083.

3.6 Conclusions - End-Cap Simulation and Optimization

In this chapter several design changes for the hadronic end-cap were examined in detail using computer simulations. The end-cap jet energy resolution was tested for different plate configurations, granularities, and plate thicknesses in the second wheel. These changes were considered with and without pile-up effects and it was concluded that any one of the changes could be made without significant loss of resolution. These results are in good agreement with previous studies [19] performed in earlier end-cap geometries without inclusion of pile-up effects.

CHAPTER 4

The Search for the Heavy Higgs Boson

4.1 Introduction

The strategy for detecting a Standard Model Higgs boson with mass larger than $2m_z$ is dependent upon the precise Higgs mass, the luminosity, detector hermeticity and the dominant Higgs production mechanism at that mass and accelerator energy [10]. For instance, for the entire Higgs mass range at the LHC, the dominant Higgs production mechanism is gluon fusion, however, at higher Higgs masses vector boson fusion also becomes important.

The "gold-plated" mode for Higgs detection at masses from 180 GeV/c^2 to 800 GeV/c^2 is the H $\rightarrow$ ZZ $\rightarrow$ 4l (l=e,μ) mode. This is the cleanest Higgs signal because it is unique and each Z can be fully reconstructed with little ambiguity [10]. The dominant background to this signal is continuum ZZ production but studies have shown that a cut requiring that one of the Z bosons have a transverse momentum greater than $m_h/2$ removes most of this background , resulting in a signal-to-background ratio of better than 20:1 for $m_h < 500$ GeV [1].

Another Higgs decay mode which has been studied for ATLAS is H $\rightarrow$ ZZ $\rightarrow$ $ll\nu\nu$. This channel has a six times larger rate than the gold-plated channel, but the decay cannot be completely reconstructed due to escaping neutrinos. It is also subject to many difficult backgrounds including the irreducible ZZ $\rightarrow$ $ll\nu\nu$ continuum

with other contributions from Z+jet, $t\bar{t}$ and WZ production. The Z+jet background dominates for $E_T^{miss} < 150$ GeV, due to jets which either escape detector acceptance or are mismeasured due to calorimeter cracks [1].

For the heavy Higgs, the final modes expected to be relevant are the mixed hadronic-leptonic decay modes of the WW and ZZ final states resulting from Higgs decay. The main reason for studying these channels is because the branching ratios are very large compared to the previously mentioned channels. In fact, the branching ratio for the H $\rightarrow$ WW $\rightarrow$ $l\nu jj$ signal is approximately 150 times that of the gold-plated channel. The fully reconstructible, H $\rightarrow$ ZZ $\rightarrow$ $lljj$ channel is also of interest, even though its cross-section is seven times smaller than in the WW case. It is this ZZ $\rightarrow$ $lljj$ signal that is the focus of the heavy Higgs search performed in this thesis and which will be the subject of the remainder of this section.

The production processes for this channel are $gg \rightarrow H \rightarrow ZZ$ and $qq \rightarrow H \rightarrow qqZZ$. The first of these processes is dominant up to $m_h = 1$ TeV, however, it has a large associated QCD background. In fact, even after stringent cuts, the QCD background is expected to be comparable to the signal, suggesting that the second process might therefore provide a better opportunity to observe a heavy Higgs signal. It has been shown [30] that the energetic forward jets in the $qq \rightarrow qqZZ$ process provide a means to enhance the signal-to-background ratio in this process. An incomplete set of tree level Feynman diagrams for the $qq \rightarrow qqZZ$ is given in Figure 4.1.

The goal in previous studies [30] was to isolate the signals in Figure 4.1,which include the Higgs resonance, from the $qq \rightarrow ZZ$ (continuum ZZ production) signals, by tagging a single high energy quark jet. The signals shown in Figure 4.1 each contain at least one final state quark jet which is very energetic and at a relatively

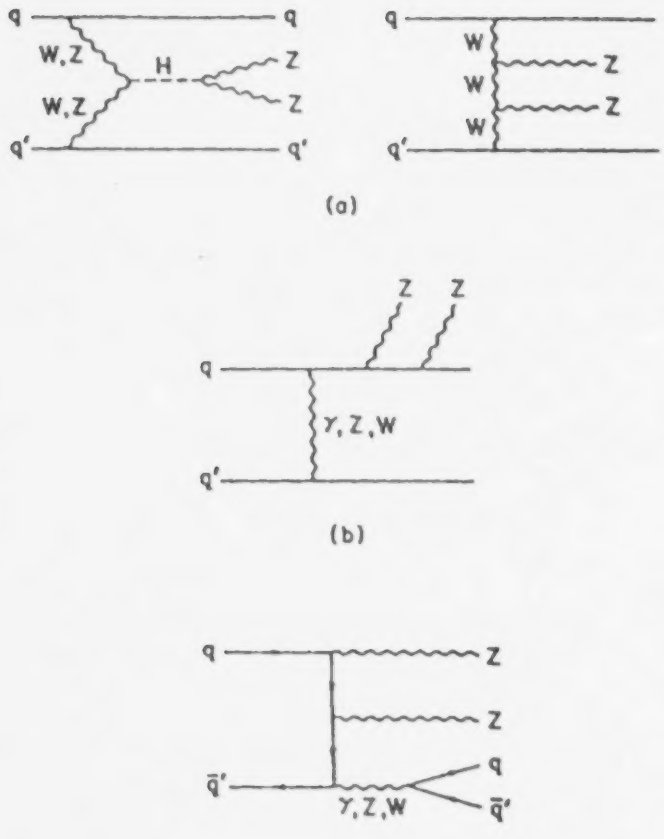

Figure 4.1: Feynman diagrams involved in $qq \rightarrow qqZZ$. Diagrams shown represent (a) vector-boson fusion, (b) t-channel photon, Z, or W exchange, and (c) s-channel electroweak-boson exchange.

large forward angle. The quark jets from ZZ continuum production have lower energy and are not generally at such large forward angles. This indicates that by tagging the energetic forward jet, the continuum background may be separated from the signals of interest. Another significant background to this signal is the Z+jets background. In fact, it is the dominant background (cross-section at least 1000 times higher than the next largest background) and is the one that this analysis will concentrate on. The process for producing this background is qq $\rightarrow$ Z+jets, which has a cross-section approximately 10^6 times that of the H $\rightarrow$ ZZ $\rightarrow$ *lljj* signal. The procedures undertaken to reduce this background are detailed in the following sections.

4.2 Jet Finding

In order to test the jet energy resolution of a calorimetry system or to reconstruct a Higgs boson decay involving jets, the first step is to identify jets. In this thesis, two distinctly different jet finding philosophies are invoked. The first is a traditional cone-based approach, the second is a novel approach for hadron colliders, known as K_t clustering [31].

First, a general introduction to cone finding techniques is presented, then the two techniques used in this Higgs analysis are described in detail. A method known as a jet profile analysis [32] is the first to be introduced. Then, an adaptation of Seymour's K_T clustering code [33] suitable for heavy Higgs searches within the structure of ATRECON is discussed. Both of these approaches have been adapted for use within ATGEN (particle-level reconstruction) as well as ATRECON (fully simulated reconstruction) in order to provide the means for a complete analysis of the H $\rightarrow$ ZZ $\rightarrow$ *lljj* signal at ATLAS.

4.2.1 Cones

Though there are many variations to cone-based algorithms, the basic principle is always the same. This principle is that a jet can be defined by a jet axis and a cone-shaped area surrounding that axis. The jet axis is determined, generally speaking, by choosing the centre of an area of particularly high energy content in the calorimeter, for instance the highest energy tower. For multi-jet events, several towers which posses an amount of energy exceeding a certain threshold can be chosen as jet centres. The exact location of the centre of the jet can be determined by a number of techniques, common ones are by simply choosing the physical centre of the highest energy tower in the jet or a more sophisticated energy weighted average centre. Once the centre has been determined a cone of radius defined by Equation 4.1

$$R = \sqrt{(\Delta\eta)^2 + (\Delta\phi)^2} \tag{4.1}$$

is drawn around this centre. The energy from every cell within this cone is then summed to give the jet energy.

Optimization of this algorithm often takes the form of adjusting the cone size or energy threshold that determines whether or not a particular energy deposit signals the presence of a jet. The adjustment of the cone radius to improve performance in the presence of pile-up effects or close-together jets is an oft-employed strategy to optimize this type of algorithm.

Although the principle of the cone-based approach is always the same, in practice the methods can be quite different. In this thesis, the cone-based method applied in this analysis is referred to as a profile analysis. It is so named due to the fact that it introduces measurable variables which allow the profile of the jet to be analyzed. The profile of the jet, in this case, refers to a measure of the lateral spread of the jet in the calorimeter.

Several regions must be defined for pairs of jets in order to reconstruct the Z boson from its decay to two jets in the profile-based coning technique. After defining a pair of jets, the jet-jet core, jet-jet centre, full jet pairs and jet-jet halo regions must be defined. The meaning of these variables is illustrated in Figure 4.9 and the exact definition of each quantity will be given in a later section (Table 4.1) along with a complete explanation of the technique and the cuts used in this analysis.

4.2.2 K_T Clustering

The second major jet finding technique applied in this analysis is K_T clustering. The K_T clustering algorithm described here is a significant departure from the usual, cone-based, approach to jet finding. This algorithm starts by assuming that every calorimeter energy tower is a jet. For each of these "jets", the quantities d_{ij}, R_{ij} and d_{iB}, as defined in Equations 4.2, 4.3, 4.4 are calculated.

$$d_{ij} = min(p_{Ti}, p_{Tj})^2 R_{ij}^2 / R^2 \tag{4.2}$$

$$R_{ij}^2 = (\Delta\eta)^2 + (\Delta\phi)^2 \tag{4.3}$$

$$d_{iB} = p_{Ti}^2 \tag{4.4}$$

These quantities can be thought of as a measure of "distance" of a jet from the beam (d_{iB}) and from the other jet in the pair (d_{ij}). This is not a true physical distance, but it is helpful to think of the quantities in his way. Once these quantities are defined for each "jet", the minimum of d_{iB} and d_{ij} is found. In a sense, the minimum of d_{iB} and d_{ij} can be thought of as determining whether each jet is "closer" to the beam or to the another jet. If it is closer to the other jet then the two jets are combined to form a single jet. If it's closer to the beam then it is folded into the "beam jet" and is effectively discarded from future clustering. This process is an

iterative one, so that after the each pass the number of jets being considered is reduced by one. This process is repeated until the number of jets remaining agrees with the number requested by the algorithm user. In this way, the algorithm is topology-driven, the user specifies the number of jets to look for based on the known topology of the signal of interest. Clearly, this approach requires that the user understands the physical process being looked for and set up the K_T clustering algorithm accordingly.

One of the key features of the K_T clustering technique is the recombination scheme that is used. The choice of recombination scheme determines how any two "jets" will be combined to form a single jet characterised by a combined four-momentum. It assigns momentum and direction to the new combined jet based on the momentum and direction of the two original jets. There are three main recombination schemes that will be considered here, the covariant E-scheme, the p_T weighted scheme and the monotonic p_t^2-weighted scheme.

The simplest recombination scheme is the covariant E-scheme. In this technique, the momentum of the new jet p_{ij} is simply defined as the sum of the four-momenta components of the two sub-jets p_i and p_j.

The p_T-weighted scheme recombines in the following way. Instead of adding the momenta, as in the covariant E-scheme, the p_T is added according to Equation 4.5.

$$p_{T(ij)} = p_{Ti} + p_{Tj} \tag{4.5}$$

where P_{Ti} and P_{Tj} are the transverse momenta of the jets being considered. The direction of the jet is then determined in a weighted fashion such that the higher p_T jet has more influence on the final jet direction than does the other jet in the pair being combined. This determination of direction is illustrated for pseudorapidity and azimuthal angle in Equations 4.6 and 4.7.

$$\eta_{(ij)} = \left(p_{Ti}\eta_i + p_{Tj}\eta_j\right) / p_{T(ij)} \tag{4.6}$$

$$\phi_{(ij)} = (p_{Ti}\phi_i + p_{Tj}\phi_j)/p_{T(ij)} \tag{4.7}$$

where η_{ij} is the pseudorapidity of the combined jet and η_i and η_j are the pseudorapidities of the two jets being considered.

The final recombination scheme discussed here is the monotonic p_T^2-weighted scheme. In this scheme, Equation 4.5 is again used to calculate the transverse momentum of the new jet. However, in this case, the R_{ij} defined in Equation 4.3 is replaced by the quantity $R_{(ij)k}$ defined in Equation 4.8

$$R^2_{(ij)k} = \frac{p^2_{Ti}R^2_{ik} + p^2_{Tj}R^2_{jk}}{p^2_{Ti} + p^2_{Tj}}, \tag{4.8}$$

where $R^2_{(ij)k}$ is the P_T-weighted radius from the jet formed from jets i and j to jet k, with subsequent values defined iteratively in the same manner. This gives still more weight than the other schemes to the harder jet when combining two jets of unequal transverse momentum and has been shown to offer some improvement for QCD reconstructions [34].

In the analysis performed here, only the first two of these recombination schemes are utilized. The third has not yet been implemented in the analysis code due to the non-standard sorting routines necessary for the monotonic weight scheme. A detailed description of the application of this technique in ATLAS is given in [33].

4.3 Muon Reconstruction

Although the emphasis of this analysis is jet reconstruction, in order to reconstruct a H $\rightarrow$ ZZ $\rightarrow \mu\mu\ jj$ decay it is also necessary to be able to reconstruct the Z that decays to muons. At particle-level (before detector simulation) the muon 4-momenta are known exactly and the leptonic Z reconstruction is simple. However, to reconstruct

muons (and hence the Z) in the full ATLAS simulation presented here requires more effort.

In order to reconstruct the Z which decays to two muons in both the signal and the background, the reconstruction package MUONBOX [35] was used. MUONBOX is a pattern recognition package that can be used to reconstruct muon tracks from hits in the detectors that make up the muon system in ATLAS and can be added-on to ATRECON (ATLAS reconstruction package), but is not a standard part of any ATLAS simulation package. The effectiveness of this package is illustrated in Figure 4.2, which shows the reconstructed Z mass from two muons in the $H \rightarrow ZZ \rightarrow \mu\mu jj$ system. The Gaussian fit to this peak yields $\sigma = 5.014$ GeV, giving a mass resolution of approximately 6%. To obtain this mass peak, all of the reconstructed muons in each event are considered as possible candidates for Z reconstruction. Then, the mass of all possible pairs of muons are calculated and the pair with mass closest to the Z mass is kept. Using this method, approximately 89% of events contained a muon pair with reconstructed mass within 20 GeV/c^2 of the Z mass. The fact that the Z reconstruction is of this high quality without any attempt to optimize the reconstruction (ie. no attempt was made to correct the events in the tails of the distribution) implies that the muon reconstruction provided by MUONBOX is very good. In fact, the efficiency for reconstructing a particular muon is $\sim$ 94%.

However, there is a serious drawback to using the MUONBOX package to reconstruct muons. The drawback is the time it takes to analyse events using full muon reconstruction. As an example, reconstructing 100 events using both the K_T clustering and jet-jet profile techniques takes approximately 20 minutes on a Hewlett-Packard 712/60 workstation. When MUONBOX is also turned on, the time for 100 events increases to about 5 hours! Nevertheless, this package was used for all full

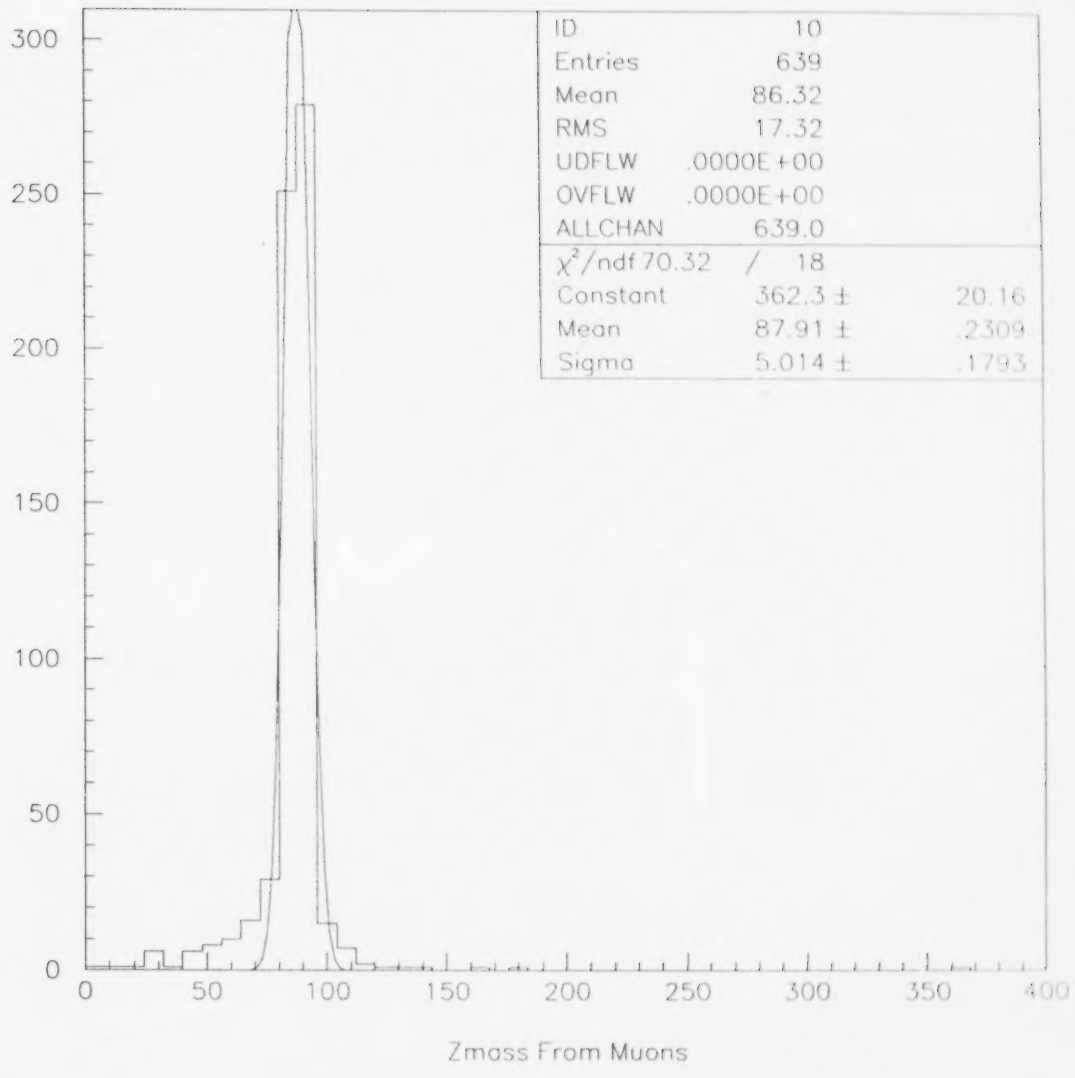

Figure 4.2: Z reconstruction from muons in the $H \rightarrow ZZ \rightarrow \mu\mu jj$ decay.

simulation muon reconstruction presented here due to the quality of the reconstruction. However, as will be presented in the next section, some muon cuts were made before full simulation (particle-level) in order to save time, based on the assumption that muons could be reconstructed 100% of the time using MUONBOX.

4.4 The Monte Carlo Production

4.4.1 Filter Selection Study

In order to understand the $H \rightarrow ZZ \rightarrow \mu\mu jj$ signal and its Z + jets background, a particle-level study of these processes was done. The study is termed "particle-level" because it is performed on the 4-vectors before they enter the simulated detector. In other words, the ATGEN/PYTHIA output was analyzed before it was passed into DICE. So, at this stage, it is still possible to access many variables which are not available in a real detector output. For instance, it is possible to find all of the daughter particles of a particular particle decay and determine the exact energy and momentum of each of the fragments without concern about detector effects. This type of study allows for a quick examination of the data before the detailed, time consuming DICE simulation is initiated.

In this analysis, a particle-level study was used to clarify many important issues before full simulation began. The first, most fundamental particle-level check, is to ensure that features of the events produced matched the requirements of the study. For instance, each signal event should contain a Higgs boson, which decays to two Z bosons, which, in turn, decay to two muons and two quark jets. Once the character of the event sample is verified, an examination of particular features of the data, for example the P_T distribution of the Z bosons and the pseudorapidity

distributions of the jets is done. This examination of particular analysis variables allows filtering cuts to be chosen.

Filtering cuts are imposed in order to limit the amount of full simulation required to acquire a significant sample of useful events. A filtering cut is a cut on the 4-vectors before they are passed through the DICE simulation. In the case of this particular signal and background, in order to get the correct ratio of signal to background without the use of filtering cuts it would be necessary to fully simulate on the order of 10^6 background events for every signal event. Clearly, time constraints would not allow a data sample of this size to be produced. So, at the particle-level, certain loose cuts are applied to the signal and the background in order to improve the signal/background ratio that needs to be fully simulated. For instance, by requiring that both the signal and the background events each contain a Z boson with a P_T of more than 120 GeV, the ratio of signal to background is improved by approximately a factor of 200.

To choose these cuts, P_T distributions of the Z bosons in the signal and the Z + jets background were obtained and are shown in Figures 4.3 and 4.4. From Figures 4.3 and 4.4, it can be seen that a cut at 120 GeV P_T is on the high energy tail of the distribution of the Z from the background (Z + jets), thereby cutting out the vast majority of the background events. However, in case of the signal, very few events are lost by performing a 120 GeV P_T cut on the Z. Since this cut greatly reduces the background and leaves the signal intact and because previous studies [36] have recommended final P_T cut of 200 GeV, the 120 GeV cut was felt to be an acceptable filter cut to be used in this study.

This filtering cut on the transverse momentum of the Z assumes good reconstruction of muon momenta will be available at the full simulation stage (to ensure

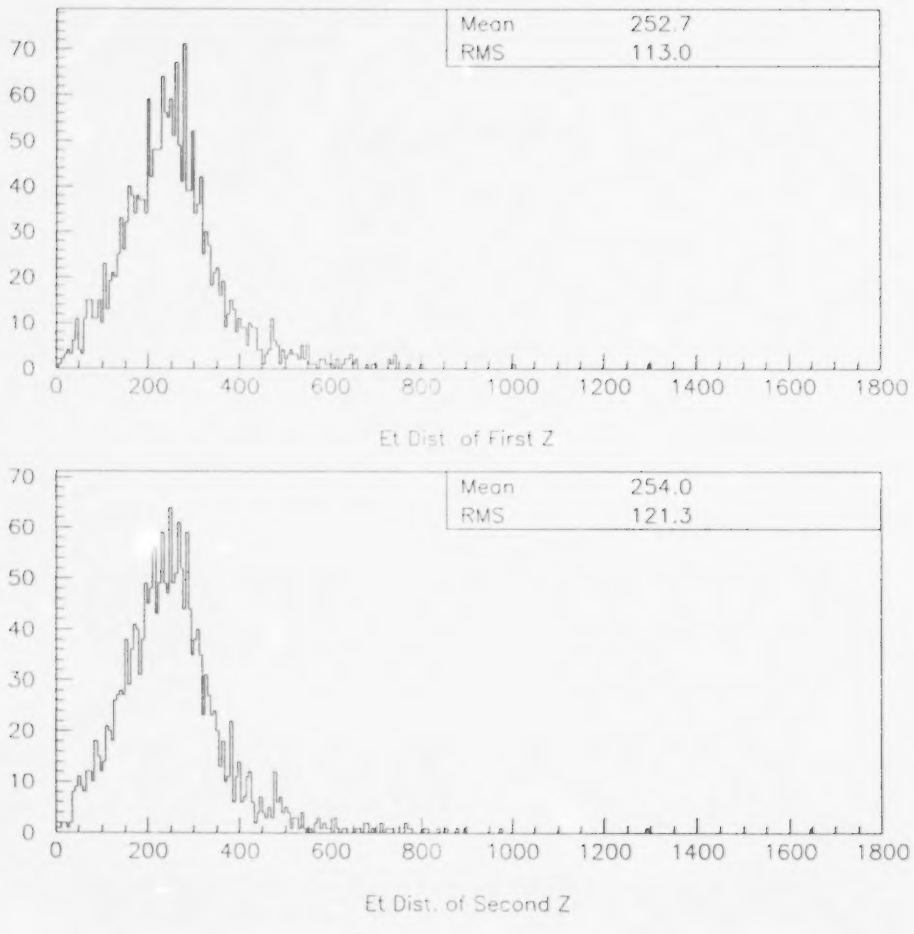

Figure 4.3: The top histogram shows the P_T distribution of one of the Z bosons from the Higgs decay in the $H \rightarrow ZZ \rightarrow lljj$ signal. The bottom histogram is the P_T distribution of the second Z from this decay.

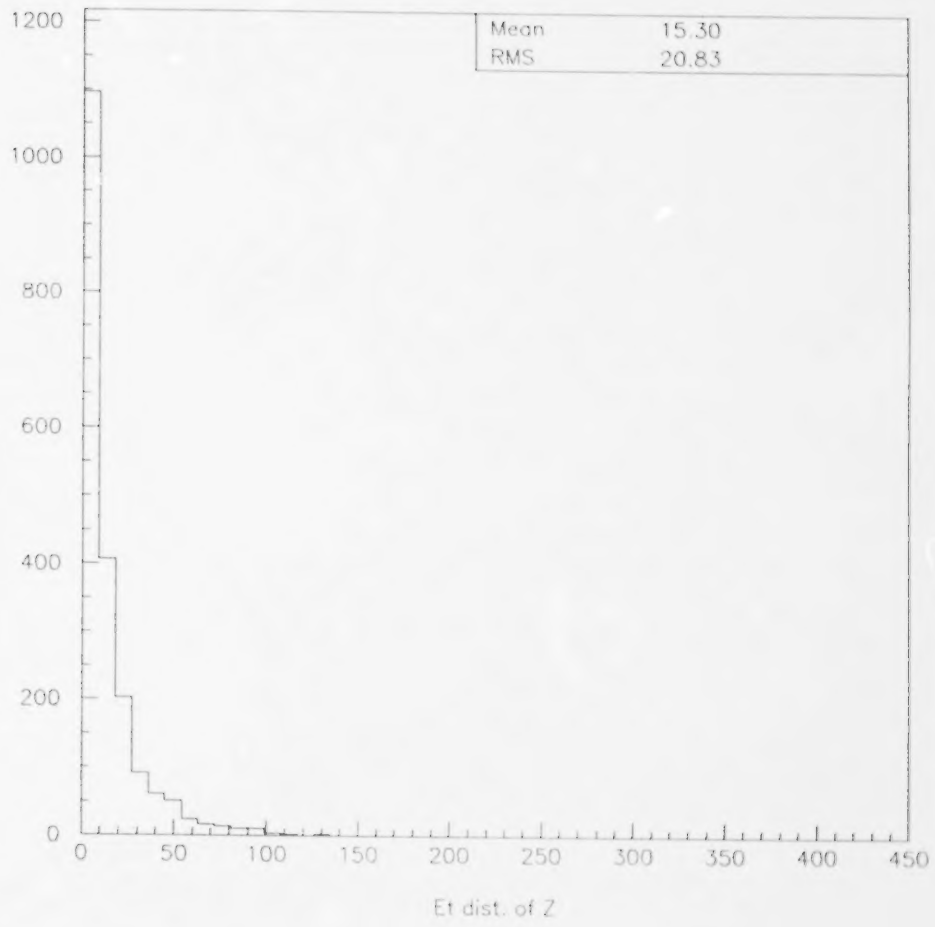

Figure 4.4: This histogram shows the P_T distribution of the Z boson in the Z + jets background

that the same cut could have been made instead after full simulation with little effect of the results), something that is supported by results from Section 4.3. After applying this cut, it was found that in 97% of the passed events, the muon pair satisfied the cut, while in the other 3% of events the transverse momentum of the quark pair alone caused the event to pass the filter. This means that, in the vast majority of of the events, this filtering cut only depends on good muon reconstruction.

In addition to the P_T of the Z bosons in the signal and background, there are several other quantities that can be used in filter cuts. In this study two other filtering cuts were used. The first of these additional filter cuts is a cut on the pseudorapidity distribution of the forward jet* Figure 4.5 shows the distributions in η of the forward jet candidates (quarks) from the $qq \rightarrow Hqq \rightarrow ZZqq$ signal. Figure 4.6 shows the same distributions for quarks or gluons which are jet candidates from the Z + jets background. These figures show that most signal events contain jet candidates in the forward region ($\eta > 1.5$). However, the candidates from the background are often at low η. For this reason, a filter cut was chosen which requires that each event (signal and background) contains a jet candidate in the pseudorapidity range $1.5 < \eta < 5.5$. The particular η values of 1.5 and 5.5 were chosen to define the forward region because the ATLAS end-cap calorimeter begins at $\eta = 1.5$ and the forward calorimeter extends to an η of 5. Therefore, no reconstruction will be possible above $\eta = 5$ in ATLAS, making this a very general, loose, cut.

The final filter cut placed on the four-vectors, based on the particle-level analysis, is a requirement that at least one of the jet candidates in the forward region has a P_T greater than 20 GeV. Figures 4.7 and 4.8 show the P_T distributions of forward jet candidates in the signal and background. These figures show that, once again,

*At this level (filtering study) the forward jet candidates are not found using a jet finder. Instead, their direction is determined by the direction of the energetic quarks or gluons coming from the event. For this reason, they are referred to here as "forward jet candidates" rather than forward jets.

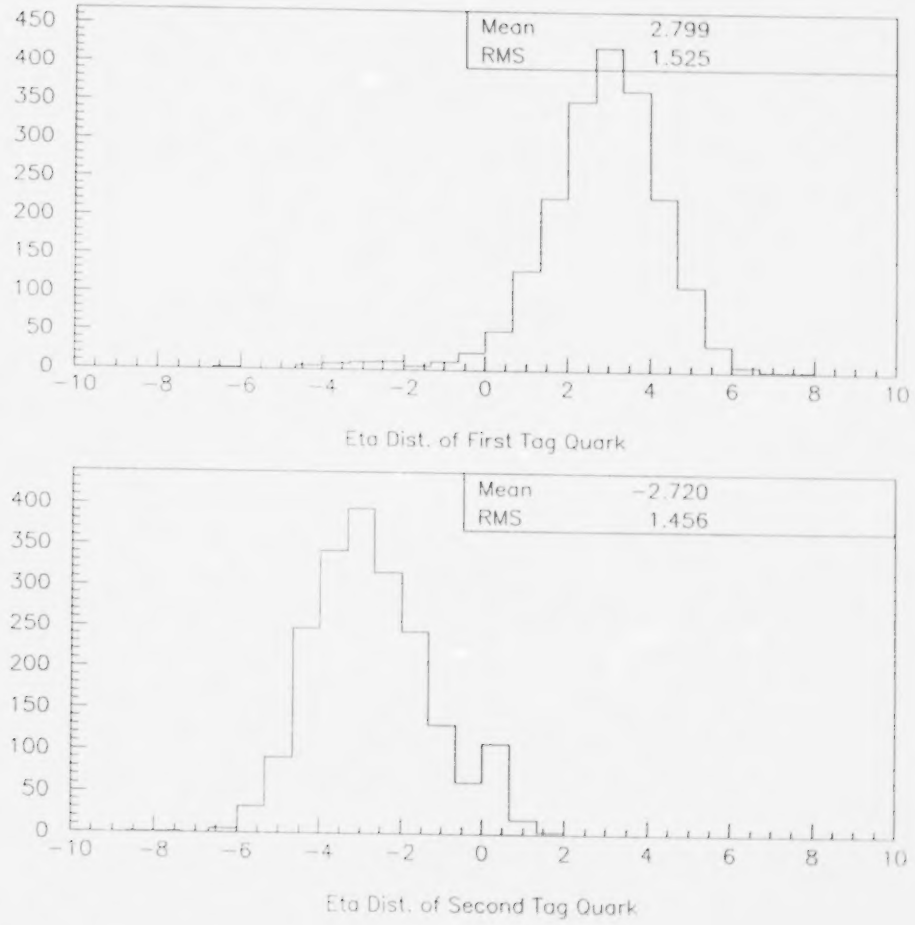

Figure 4.5: η distributions of forward tag quarks from $qq \to Hqq \to ZZqq$ signal

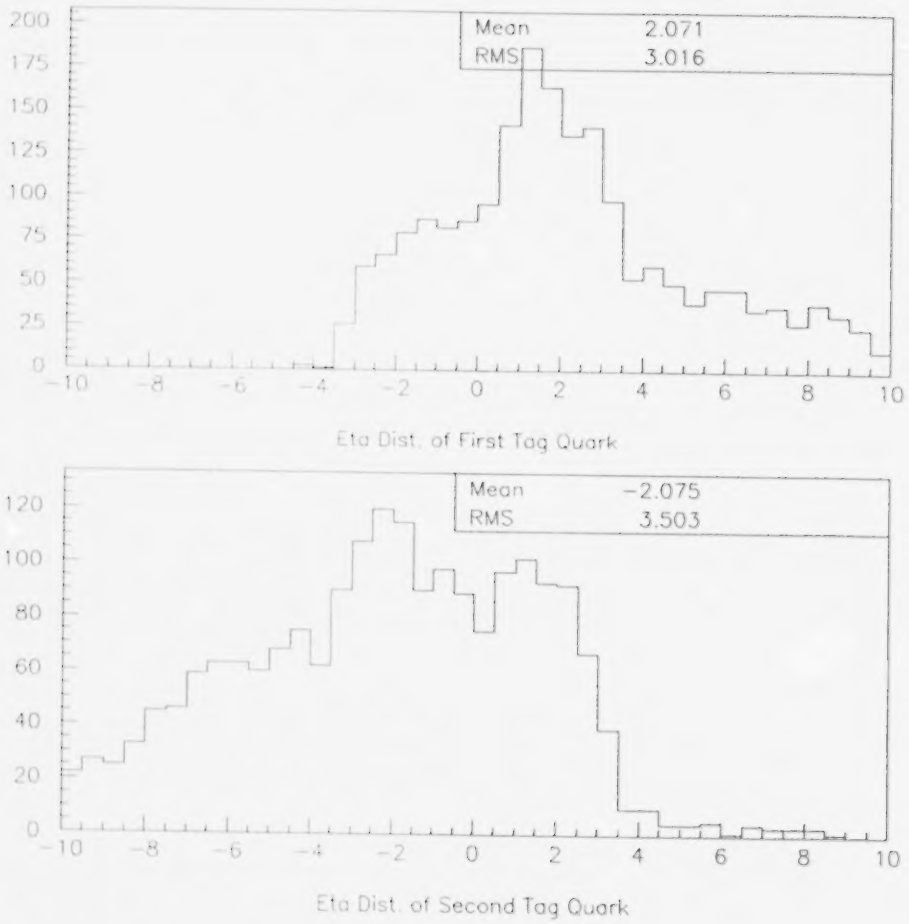

Figure 4.6: η distributions of quark or gluon jet candidates from Z + jets background

the filtering cut is made on the high P_T tail of the P_T distribution of the background events while it has a very small impact on the signal events. This is another very loose filtering cut. In reality, much harder jet P_T cuts will have to be made in the forward region to deal with the effects of pileup thereby making this a conservative cut.

The particle-level analysis of the Higgs signal and its background allows specific filtering cuts to be chosen and invoked for the remainder of this study. This allows a significant time saving to be realized in the full DICE simulation of heavy Higgs events. The filtering applied here cut 999/1000 background while only cutting 1/10 signal.

4.4.2 The Full-Simulation Production

After filtering, the four-vectors were passed through a full DICE simulation (version 1.0904). Approximately one thousand signal events at $M_h = 600$ GeV/c^2 were fully simulated along with approximately 1000 Z + jets background events in the same (TP0) geometry.

The signal was produced using a scalar version of DICE on a group of IBM RISC 6000 workstations using AIX 4.1 (IBM UNIX version). The Z + jets background events were produced using a parallel version of DICE on six nodes of an IBM SP2 (AIX 3.2) at the University of Alberta.

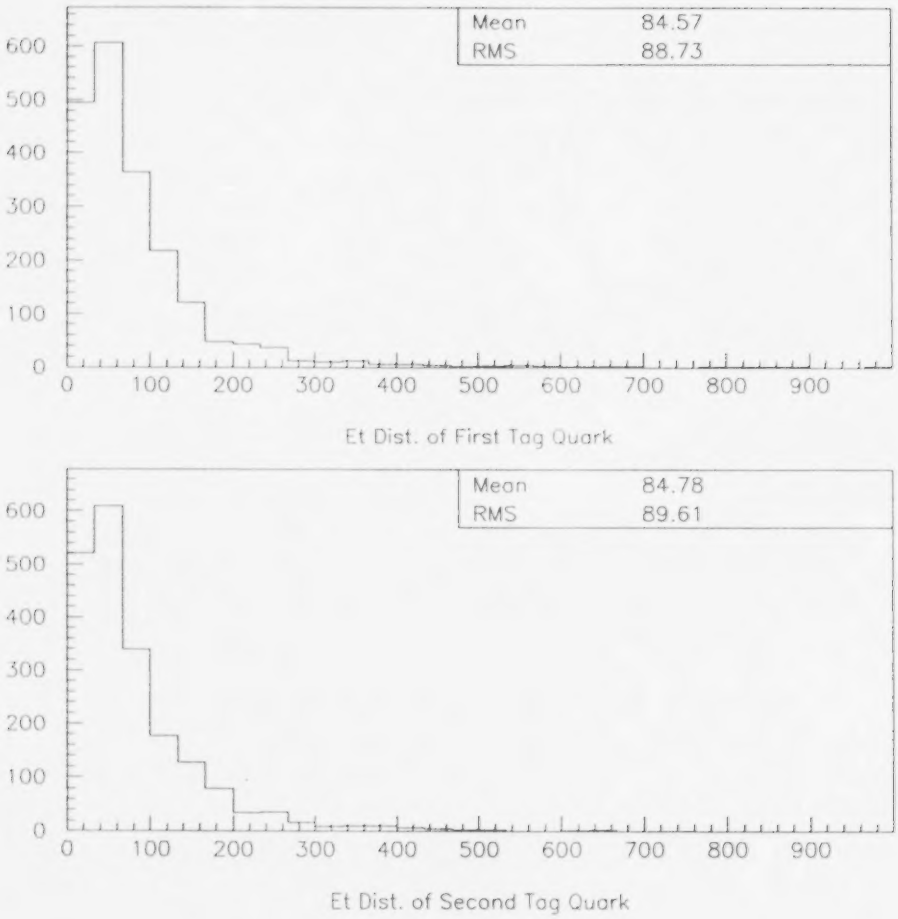

Figure 4.7: P_T distributions of forward jet candidates from signal events

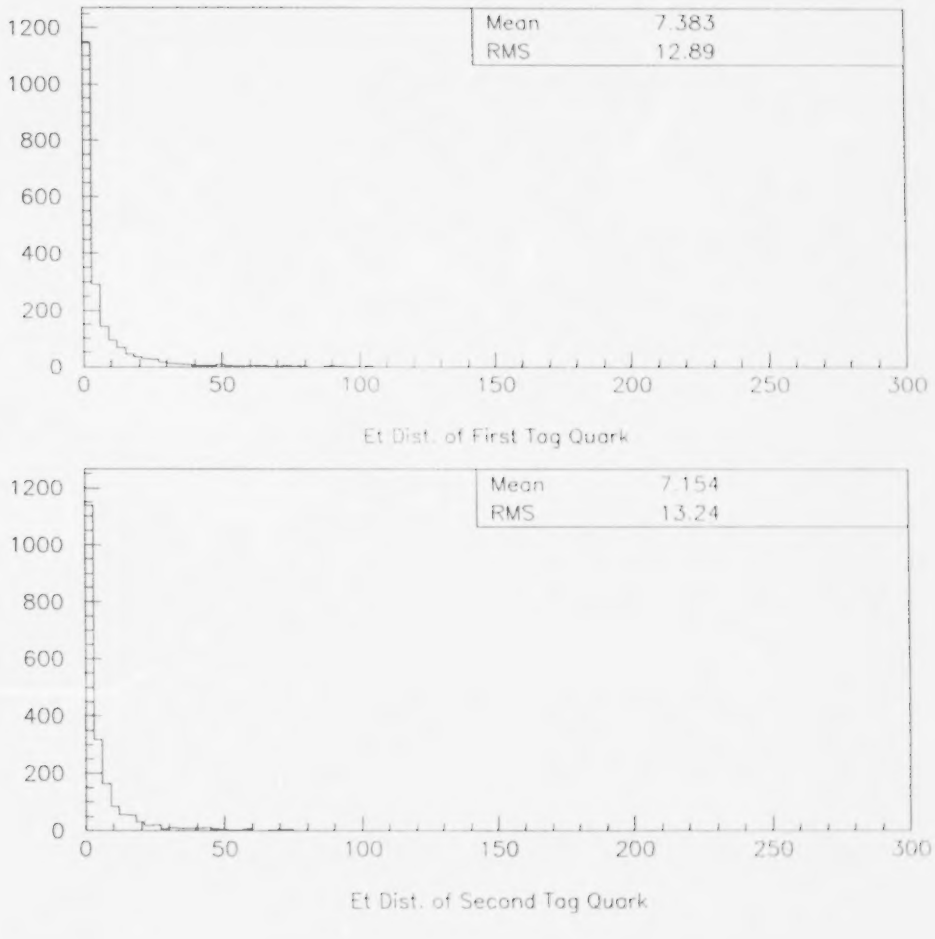

Figure 4.8: P_T distributions of forward jet candidates from background events

Jet Definitions	
Jet Core	Cells Within R(core)=0.2
Jet Centre	Cells Within R(centre)=0.35
Full Jet	Cells Within R(halo)=0.6
Jet Halo	Cells between R(centre) and R(halo)
Jet Pair Definitions	
Jet-Jet Core	Cells Within R(core) of either jet
Jet-Jet Centre	Cells Within R(centre) of either jet
Jet-Jet Pair	Cells Within R(halo) of either jet
Jet-Jet Halo	Cells Between R(centre) and R(halo) of either jet

Table 4.1: Jet Definitions.

4.5 Results - Full Simulation Reconstruction

4.5.1 Reconstruction of Higgs Using Profile Analysis

In order to reconstruct the Z boson from two jets using the profile-based coning technique, it is necessary to define many new quantities. The profile variables necessary for defining jets and jet-jet pairs are each defined in Table 4.1 and their meaning is illustrated in Figure 4.9.

In order to find jets and jet-jet pairs by the definitions given in Table 4.1, the centres of the jets must first be found. For this analysis, jet centres have been found in the following very simple way. All cells with $E_T > 5$ GeV are considered as possible centres. The 4 cells with the highest E_T and which are separated by more than an R ($\sqrt{\Delta\eta^2 + \Delta\phi^2}$) of 0.4 are chosen as jet centres.

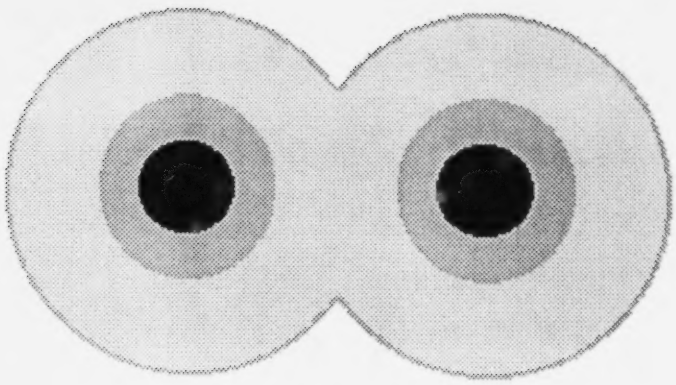

Figure 4.9: This drawing shows the regions defining a jet-jet pair in the profile technique. The darkest area represents the jet-jet core, the next darkest is the jet-jet centre region and the lightest is the jet-jet halo.

Once the centres have been chosen, jet pairs are formed by demanding that R < 0.1 between the two jet cores and that the P_T of the jet-jet core be greater than 150 GeV. If there is more than one jet pair that meets the P_T requirement, the pair with the highest P_T is chosen. The P_T cut is a strong background rejection cut, as most signal events will contain high P_T jet-pairs while Z + jets events will not. In the background sample, when a jet pair can be formed that meets this P_T cut it will most often be composed of two well-separated jets whereas the jets that form the jet pairs in signal events will be relatively close together in η/ϕ space. Therefore, the cut on jet separation (< 1.0) has the effect of further reducing the background while not severely cutting down on the efficiency.

After the jet pair is chosen, several other cuts can be applied. The first is a requirement that the azimuthal opening angle (ϕ) between the leading lepton pair

and the hadronic jet pair must 90°. This cut is expected to be effective because the signal events arise from the decay of a Higgs which decays isotropically (in its rest frame) emitting two Z bosons travelling back-to-back. Since the Higgs is in motion when it undergoes this decay, the Z's will be boosted in the direction of motion of the Higgs, reducing the angle between the two Z's. However, this boost is not expected to be large enough to close the azimuthal angle between the two Z's to less than 90°. Meanwhile, the background arises from a single Z boson and several jets that are not expected to be travelling preferentially in a direction opposite to the Z and so are not expected to show this gap in azimuthal angle. This cut is used to further improve the signal to background ratio.

Another important cut that can be used to distinguish this signal from its background is an invariant mass cut on the reconstructed Z mass. The Z-mass is reconstructed using the full jet-jet pair as defined in Table 4.1. Events with invariant mass within a certain mass window (eg. $M_Z \pm 10$ GeV) of the known Z mass are considered to be Higgs candidates, those events with reconstructed masses outside of this mass window are rejected. Since the two high P_T jets in the signal truly arise from a Z decay, the profile technique would be expected to reconstruct a large fraction of signal events in this mass window. However, the reconstructed background events, which do not contain a $Z \rightarrow jj$ decay would not be expected to fall within this mass window.

In addition to the use of these standard quantities for cutting the Z + jets background, new quantities which make use of jet profile information can be used. Two useful jet-jet profile variables which come out of this analysis technique are the fraction of the full jet pair E_t that occurs in the jet-jet halo region (F_{E_T}), and the invariant mass shift from the jet-jet cores to the full jet-jet pairs (ΔM). The definitions of these quantities are given below in Equations 4.9 and 4.10.

$$F_{E_T} = E_t(jet - jet\ halo)/E_t(full\ jet) \tag{4.9}$$

$$\Delta\ M = M(full\ jet - jet) - M(jet - jet\ cores) \tag{4.10}$$

The quantities F_{E_T} and ΔM can be used to distinguish signal from background because background jets are expected to have more debris in the halo area than the signal jets do. This difference occurs because the jets produced in the signal come from a much different source than do the jets in the background. The signal jets come from a Z (colour singlet) while the background jets come from high P_T recoil quarks which are not colour singlets and produce additional gluons via bremsstrahlung. These radiated gluons are responsible for the added halo debris in the background events.

In the original study of this technique [32], Field and Griffin found that, at a 40 TeV centre-of-mass energy (at particle-level, using the ISAJET generator), an enhancement (percent survival of signal / percent survival of background) factor of more than 300 could be obtained for an 800 GeV/c^2 Higgs decaying to two jets and two leptons via a pair of Z's.

The profile algorithm described in this section has been applied to 762 fully simulated Higgs events of mass 600 GeV/c^2 and 1092 Z + jets events. For the signal, this algorithm successfully reconstructs the Z and Higgs particle invariant mass, as shown in Figure 4.10. The true measure of the success of this technique, however, is how well it distinguishes the signal from its Z + jets background.

The effectiveness of the profile algorithm in distinguishing signal from background has been measured by using cuts on the quantities described in earlier: P_T, core separation, Z mass, Higgs mass, F_{E_T} (as defined in Equation 4.9), and $\Delta\ M$ (as defined in Equation 4.10)[†]. A summary of the efficiencies, rejections, enhancements

[†]The azimuthal angle cut on the leading lepton pair and the reconstructed jet pair, also described

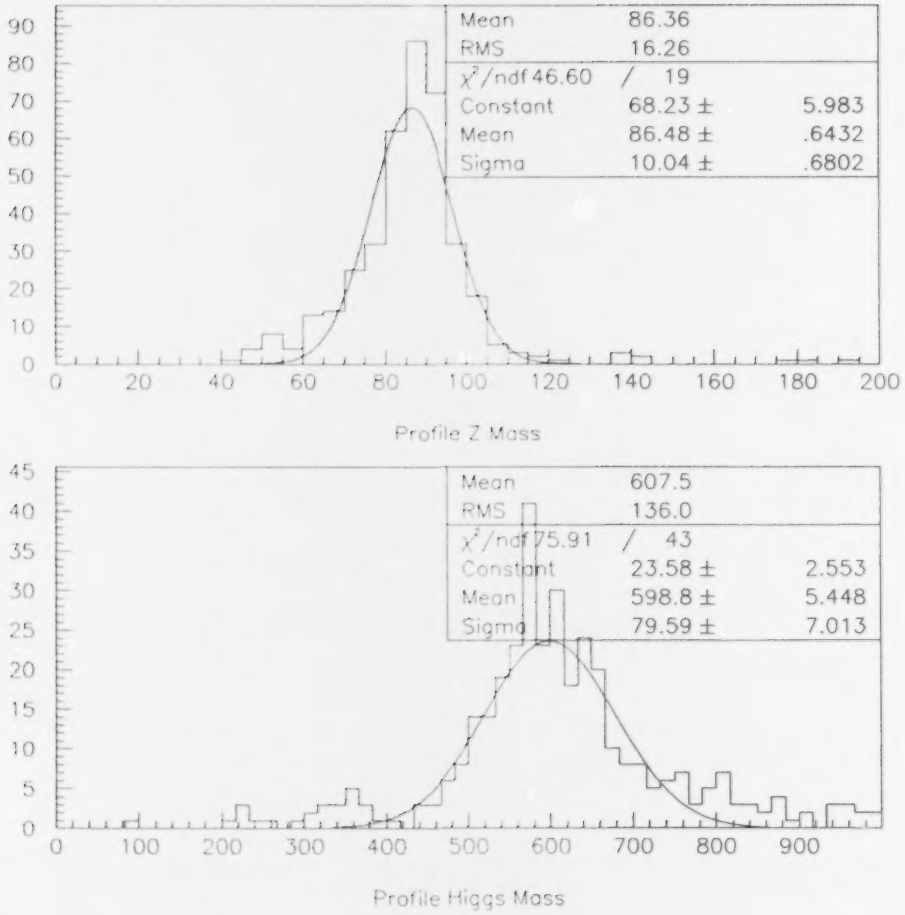

Figure 4.10: Invariant mass of the Z and Higgs particles as reconstructed from two jets using jet-jet profile technique.

and $S/\sqrt{B}$ obtained using these cuts is given in Table 4.2. The results presented in this table include a standard $P_T > 150\ GeV$ cut on the jet core and a requirement that the cores of the jet-jet pair be separated by no more than 1.0 in all instances, as described in the introduction to the jet profile analysis technique presented earlier.

These results show that, for the profile analysis of full simulation Higgs events, the best combination of cuts, in terms of signal enhancement, is a simple mass window cut on both the Z mass and the Higgs mass. The results also show that, on this small sample of events, the background events can be completely eliminated by making use of either of the jet profile variables F_{E_T} or ΔM. The signal enhancement seen in Table 4.2 indicates that the jet profile analysis technique employed here is a very promising one for distinguishing $H \rightarrow ZZ \rightarrow \mu\mu jj$ events from the Z + jets background.

4.5.2 Reconstruction of Higgs Using K_T Clustering Analysis

For the analysis of the $H \rightarrow ZZ \rightarrow lljj$ signal and its Z + jets background, several cuts have been tested on the K_T clustering output. In most cases, the cuts have been chosen to mirror the cuts of the profile analysis, for the purpose of comparison. However, an effort has also been made to discover new cuts which better take advantage of this innovative technique.

Three of the cuts described earlier for the profile analysis, an azimuthal angle cut of 90° between the leading lepton pair and the reconstructed Z jet, a P_T cut on the jet and a mass window cut can also be applied to the output of the K_T clustering analysis.

---

previously, was also applied but proved ineffective and so is not included in these results

762 signal 1092 backgrnd		No. Pass	Reject.	Eff.	Enhance	$S/\sqrt{B}$ PYTHIA	$S/\sqrt{B}$ ISAJET
Higgs mass window	S	382		50.1%			
	B	39	96.4%		14.0	3.8	5.3
Z and H mass windows	S	175		23.0%			
	B	3	99.7%		83.6	6.0	8.4
$P_{Tcore} > 200\ GeV$	S	118		15.5%			
Z, H mass windows	B	2	99.8%		56.4	4.9	6.9
$P_{Tmu} > 200\ GeV$	S	130		17.1%			
Z, H mass windows	B	2	99.8%		93.1	5.4	7.7
Z, H mass windows	S	15		2.0%	Insufficient		
$F_{E_T} < 1.5\%$	B	0	100%		Statistics		
Z, H mass windows	S	38		5.0%	for		
$\Delta M > 15$ GeV	B	0	100%		Calculation		

Table 4.2: Rejection, efficiencies enhancements and Signal/$\sqrt{background}$ (using each of PYTHIA and ISAJET to calculate background cross-sections)of the jet-profile-based Higgs (mass = 600 GeV/c^2) reconstruction are presented. Cuts on the P_T (>150 GeV) of the reconstructed jet pair core region and on core separation (<1.0) are implemented for all cases. The H mass window extends from 460 GeV to 740 GeV, the Z mass window extends from 81 GeV to 101 GeV, P_{Tcore} refers to the total transverse momentum of the jet-jet core region and P_{Tmu} is the transverse momentum of the muon pair.

However, these cuts are not necessarily good cuts in this type of analysis. Take, as an example, the mass window cut. This cut is not well suited for this analysis because of the way the Z mass is reconstructed in the K_T clustering algorithm. The mass is reconstructed by clustering to more jets (usually n + 3) than would normally be requested based on the topology of the event of interest. Then all possible combinations of at least two jets are tried to find the combination that gives a reconstructed mass closest to the Z mass. This technique has the advantage that it does not discard soft jets from the Z as often as if the clustering were done in the more standard way of requiring the precise number of jets expected. By stopping the clustering at a point when there are more jets left than expected a more accurate reconstruction can be obtained. However, the disadvantage of this technique is that it shapes the mass of the jets reconstructed from backround events to look like the Z mass. This makes the mass window cut ineffective for K_T clustering using the combinatorial approach to reconstruct the Z mass.

Though the mass window cut is not as effective for this approach as it was for the jet profile analysis, another quantity, the "effective cone radius" of the jet has the potential to make up for this discrepancy. The effective cone radius of a jet reconstructed using this technique is defined as half of the η/ϕ distance separating the two most widely separated "jets" of the reconstructed Z. In signal events, this radius is expected to be relatively small. This is because the jets combined to form the Z mass should actually arise from a single particle, the Z. In the background, however, the jets recombined to give the best Z mass will often be very well separated, as they mimic the Z mass by mere coincidence. This information allows for improved distinction of signal from background. Therefore, it is possible to utilize the K_T clustering technique to reconstruct a jet and still define cone-like quantities to aid in background rejection.

Using the above cuts, the K_T clustering algorithm described in Section 4.2.2 has been been applied to the 762 fully simulated Higgs events and 1092 Z + jets events. For the signal, this algorithm successfully reconstructs the Z and Higgs particle invariant mass, as shown in Figure 4.11. Again, the cuts, detailed above, have been applied in order to better distinguish signal from background. The results of these cuts are summarized in Table 4.3.

4.5.3 Conclusions - Full Simulation Reconstruction

The results of applying these two jet finding algorithms to the $H \rightarrow ZZ \rightarrow \mu\mu jj$ signal and its Z + jets background show that each algorithm provides significant signal enhancement and should allow a heavy Higgs signal to be observed in ATLAS. However, at this stage the jet-jet profile technique appears to have a significant advantage over K_T clustering for this signal (best $S/\sqrt{B} = 6$ as compared to an $S/\sqrt{B}$ of 2.2 for full simulation).

The advantage that the profile technique currently holds may be due to the fact that its use is better understood and the cuts are therefore better optimized for this signal. Since this is the first time that the K_T clustering technique has been applied to this type of signal, work still needs to be done to find the best variables to cut using this technique. Work in this area is continuing with the intent of producing a K_T clustering analysis with a performance which is competitive with the profile technique.

The largest source of error in this full-simulation analysis is statistical, the sample of events is not large enough. The low number of events makes it difficult to estimate precise values for $S/\sqrt{B}$ due to statistical fluctuations. For example, the statistical errors on each of the $S/\sqrt{B}$'s presented in the tables of this section can

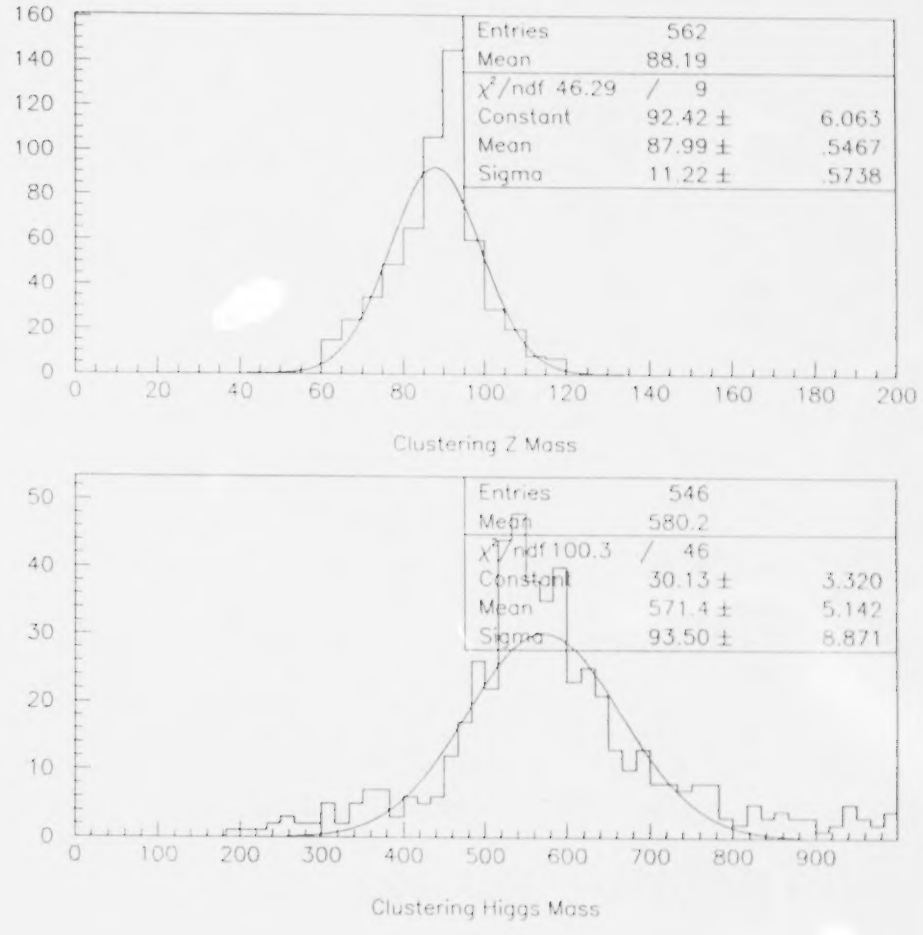

Figure 4.11: Invariant mass of Z and Higgs particles as reconstructed from two jets using K_T clustering technique.

762 signal 1092 backgrnd		No. Pass	Reject.	Eff.	Enhance	$S/\sqrt{B}$ PYTHIA	$S/\sqrt{B}$ ISAJET
H mass window	S	420		55.1%			
	B	140	87.2%		4.3	2.2	3.1
Z, H mass windows	S	272		35.7%			
	B	87	92.0%		4.5	1.8	2.5
Z, H mass windows	S	217		28.5%			
$P_{Tmu} > 200$ GeV	B	48	95.6%		6.5	1.9	2.7
Z, H mass windows	S	78		10.2%			
Jetcone > 0.5	B	7	99.4%		16.0	1.8	2.6
Z, H mass windows	S	60		7.9%			
$P_{Tmu} > 200$ GeV	B	5	99.5%		17.2	1.7	2.3
Jetcone < 0.5							

Table 4.3: Rejection, efficiencies, enhancements and Signal/$\sqrt{background}$ (using each of PYTHIA and ISAJET to calculate background cross-sections)of the K_T clustering-based Higgs (mass = 600 GeV/c^2) reconstruction are presented. A cut on the P_T (>150 GeV) of the reconstructed Z is implemented for all cases. The H mass window extends from 438 GeV to 762 GeV, the Z mass window extends from 81 GeV to 101 GeV and P_{Tmu} is the transverse momentum of the muon pair.

range as high as about 3, in the case when the cuts remove a very large fraction of background events. The low statistics also make it difficult to estimate the true effectiveness of the profile cuts because they completely eliminate the background for this small number of events.

The difficulty with obtaining enough fully simulated events to remedy this problem of low statistics is the length of time it takes to generate fully simulated events (approximately 2.5 hours of CPU time per event on one node of an IBM SP2). So, to obtain 10000 fully simulated background events would take approximately 3 years of CPU time (multiply by more than a factor of two to obtain real time on shared machines). Therefore, even with several machines, this is a very large time investment in simulating a detector geometry which is constantly evolving.

For this reason it is desirable to attempt these event and background reconstructions at the particle-level in order to increase speed and flexibility.

4.6 Results - Particle Level

The profile analysis algorithm and the K_T clustering analysis algorithm presented earlier in this chapter have been adapted for use in the ATGEN particle-level analysis routines. The reason for incorporating these algorithms into ATGEN is the speed advantage obtained by not performing a full detector simulation. The speed at which particle-level analyses can be performed allows for a thorough examination of the analysis algorithms with better statistics (ie. more events) than in full simulation. The ability to improve statistics is particularly relevant when studying events such H $\rightarrow$ ZZ $\rightarrow$ *lljj* which has a background (Z + jets) that will be produced, at ATLAS, with approximately one million times the frequency of the signal. The large number of

background events produced means that, even after filtering cuts have been applied, full simulation of enough background events to accurately model the experimental environment is extremely difficult.

If it can be shown that a particle-level reconstruction using a chosen algorithm is a good predictor of the full simulation performance of that algorithm, then either particle-level reconstruction can be done in place of fully simulated background reconstruction or additional studies which would be too time consuming to attempt with a full detector simulation can be performed. To illustrate this agreement of particle-level and full simulation results, consider the Z mass reconstruction produced by the profile-based coning as presented in Figure 4.12. This figure shows that for $100\%/\sqrt{E}$ energy smearing ("smearing" the energy in each η/ϕ bin by a Gaussian distribution) the agreement between particle level and full simulation results is very good. This agreement implies that the results of a particle-level study will be a good predictor of the full-simulation performance.

One effect which would be difficult to test using full simulation is the effect of detector energy resolution on the performance of each algorithm. In a full simulation, a particular detector is chosen to be simulated and its energy resolution is not an adjustable parameter. Therefore, testing several different resolutions is not an easy task, involving resimulation of events with several different detector geometries or, alternatively, simulating the same geometry with several different hadronization packages. At the particle-level, however, it is possible to "smear" the energy in a particular η/ϕ bin by a Gaussian distribution, with the width of the Gaussian as an easily alterable parameter. In this way, the effect of changing detector resolution can be estimated by reconstructing events at the particle-level with several different smearings.

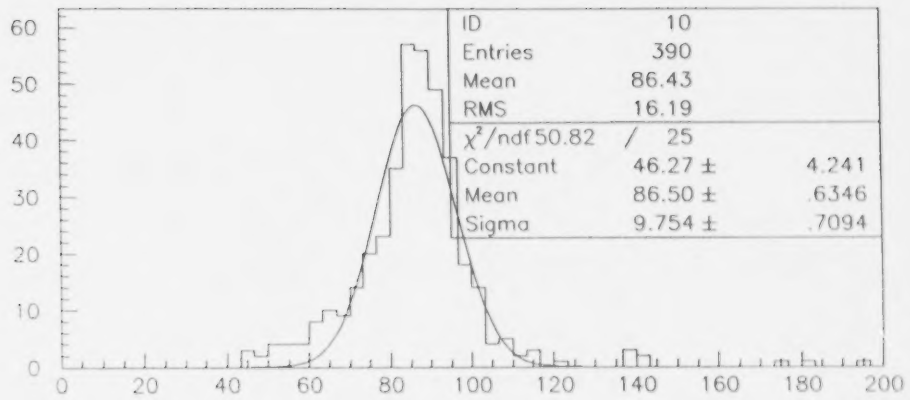

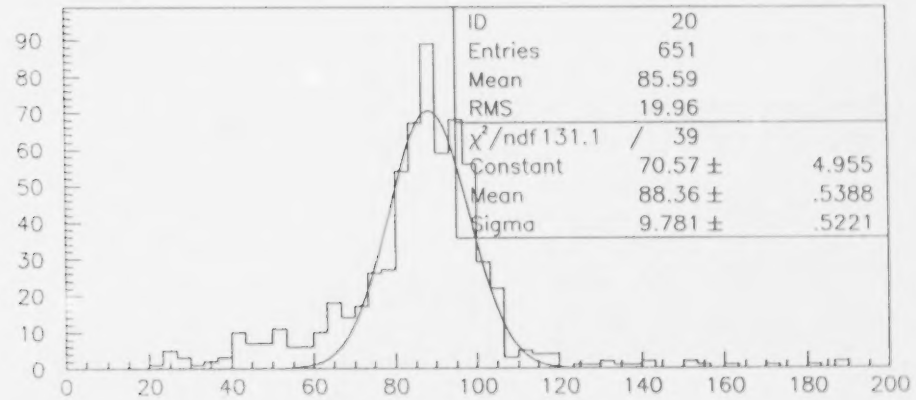

Figure 4.12: Full simulation and particle-level Z mass reconstructions are compared for a particle-level resolution of $100\%/\sqrt{E}$.

A study of the performance of the profile and clustering algorithms is presented here for many different detector resolutions corresponding to a range of resolutions from a perfect detector, to a detector with a $150\%/\sqrt{E}$ resolution. Since this smearing only takes into account a "sampling term" (dependent on $1/\sqrt{E}$) without regard to a constant or noise term in the energy resolution, this test would not be expected to fully take into account the effects of pile-up. In fact, pileup is not treated in the Higgs analysis presented here, though it is a planned study for the future.

It should be noted that neither of these algorithms is the default methods used in this ATLAS jet finding. So far, the only jet finders built-in to ATLAS reconstruction (particle-level and full simulation) have been based on single, simple cones.

4.6.1 Profile Analysis, Including Effects of Energy Resolution

The profile analysis technique described previously has been applied to 10000 Z + jets events and 1000 $H \rightarrow ZZ \rightarrow lljj$ events for each different smearing (detector resolution). Figure 4.14 shows the effect of worsening energy resolution on the signal efficiency of the algorithm (using F_{E_T} cut described earlier). Summaries of the results for three of these smearings are shown in Table 4.4 for the case in which no smearing was applied, Table 4.5 for smearing which emulates a $50\%/\sqrt{E}$ resolution and Table 4.6 for smearing which emulates a $150\%/\sqrt{E}$ detector energy resolution.

In the tables of results presented here, the "enhancement factor" refers to the ratio of the percentage of signal that survives a cut to the percentage background that survives that same cut. The $S/\sqrt{B}$, where S refers to signal and B refers to background, values in the last two columns in these tables are calculated using a

predicted LHC luminosity of 10^5 pb^{-1} (integrated over one year), a Higgs production cross-section calculated by PYTHIA (physics generator) and a Z + jets cross-section calculated from either PYTHIA (first column of values), or ISAJET (second column of $S/\sqrt{B}$) . The reason that two different generator codes are compared for the calculation of the Z + jets cross-section is to minimize the danger of generator-specific inaccuracy in cross-section estimation. So, the cross-sections calculated from two widely used generators (PYTHIA and ISAJET) were each used to calculate the expected background rates in ATLAS, however, only PYTHIA was used to generate 4-vectors. A third generator, specifically written to simulate vector boson production, which can also be compared to PYTHIA is VECBOS. However, at the time this study was performed, W + jets generation was possible in the ATLAS version of VECBOS, but Z + jets generation was not. When VECBOS is capable of Z +jets production, it should also be used to calculate the expected cross-sections.

In addition to the results presented in Tables 4.4 through 4.6, the performance of the algorithm as a function of worsening energy resolution is shown in Figure 4.13 for the signal efficiency and Figure 4.14 for Z mass reconstruction. These results show that the performance of the profile algorithm in distinguishing signal from background degrades with worsening detector resolution. While the difference in performance between the perfect calorimeter (no smearing) and the smearing which emulates a $50\%/\sqrt{E}$ detector resolution is relatively small, if the smearing is increased further, to $100\%/\sqrt{E}$, for example, performance begins to degrade. This can be seen in Figure 4.14, in which the Z mass resolution worsens significantly between $70\%/\sqrt{E}$ and $100\%/\sqrt{E}$. Also, the PYTHIA-calculated $S/\sqrt{B}$ (for the best case) drops from 9.0 to 6.0 when energy resolution is changed from $50\%/\sqrt{E}$ to $150\%/\sqrt{E}$. The ATLAS design goal for the end-cap calorimetry is a sampling term of $50\%/\sqrt{E}$, an acceptable number based on these results. However, if the design goal is not met,

1000 signal 10000 backgrnd		No. Pass	Reject.	Eff.	Enhance	$S/\sqrt{B}$ PYTHIA	$S/\sqrt{B}$ ISAJET
H mass window	S	505		50.5%			
	B	583	94.17%		8.7	3.0	4.2
Z, H mass windows	S	340		34.0%			
	B	62	99.38%		54.8	6.1	8.6
Z, H mass windows	S	282		28.2%			
$P_{Tcore} > 200$ GeV	B	41	99.59%		68.8	6.3	8.6
Z, H mass windows	S	252		25.2%			
P_{Tmu} ¿ 200 GeV	B	43	99.57%		58.6	5.5	7.7
Z, H mass windows	S	169		16.9%			
$F_{E_T} < 1.5\%$	B	6	99.94%		281.7	9.8	13.8
Z, H mass windows	S	224		22.4%			
$\Delta M > 15$ GeV	B	19	99.81%		117.9	7.3	10.3

Table 4.4: Rejection, efficiencies, enhancements and Signal/$\sqrt{background}$ (for background cross-sections calculated for each of PYTHIA and ISAJET, Luminosity = $10^5 pb^{-1}$ over one year) results of the particle-level jet-profile-based Z reconstruction with no smearing are presented. Cuts on the P_T (>150 GeV) of the reconstructed jet pair core region and on core separation (<1.0) are implemented for all cases. The Higgs mass window extends from 460 to 740 GeV/c^2, the Z mass window extends from 81 to 101 GeV/c^2, P_{Tcore} and P_{Tmu} refer to the transverse momenta of the jet-jet core and the muon pair respectively.

1000 signal 10000 backgrnd		No. Pass	Reject.	Eff.	Enhance	S/$\sqrt{B}$ PYTHIA	S/$\sqrt{B}$ ISAJET
H mass window	S	503		50.3%			
	B	572	94.28%		8.8	3.0	4.2
Z, H mass windows	S	338		33.8%			
	B	63	99.37%		53.7	6.1	8.5
Z, H mass windows	S	278		27.8%			
$P_{Tcore} > 200$ GeV	B	39	99.61%		71.3	6.3	8.9
Z, H mass windows	S	252		25.2%			
P_{Tmu} ¿ 200 GeV	B	46	99.54%		54.8	5.3	7.4
Z, H mass windows	S	167		16.7%			
$F_{E_T} < 1.5\%$	B	7	99.93%		238.6	9.0	12.6
Z, H mass windows	S	219		21.9%			
$\Delta M > 15$ GeV	B	21	99.79%		104.3	6.8	9.6

Table 4.5: Rejection, efficiencies, enhancements and Signal/$\sqrt{background}$ (for background cross-sections calculated for each of PYTHIA and ISAJET, Luminosity = $10^5 pb^{-1}$ over one year) results of the particle-level jet-profile-based Z reconstruction with 50% smearing are presented. Cuts on the P_T (>150 GeV) of the reconstructed jet pair core region and on core separation (<1.0) are implemented for all cases. The Higgs mass window extends from 460 to 740 GeV/c^2, the Z mass window extends from 81 to 101 GeV/c^2, P_{Tcore} and P_{Tmu} refer to the transverse momenta of the jet-jet core and the muon pair respectively.

1000 signal 10000 backgrnd		No. Pass	Reject.	Eff.	Enhance	$S/\sqrt{B}$ PYTHIA	$S/\sqrt{B}$ ISAJET
H mass window	S	498		49.8%			
	B	590	94.1%		8.4	2.9	4.1
Z, H mass windows	S	260		26.0%			
	B	65	99.35%		40	4.6	6.5
Z, H mass windows	S	209		20.9%			
$P_{Tcore} > 200$ GeV	B	36	99.64%		58.1	5.0	7.0
Z, H mass windows	S	191		19.1%			
P_{Tmu} ¿ 200 GeV	B	47	99.53%		40.6	4.0	5.6
Z, H mass windows	S	127		12.7%			
$F_{E_T} < 1.5\%$	B	9	99.91%		141.1	6.0	8.5
Z, H mass windows	S	172		17.2%			
$\Delta M > 15$ GeV	B	23	99.77%		74.8	5.1	7.2

Table 4.6: Rejection, efficiencies, enhancements and Signal/$\sqrt{background}$ (for background cross-sections calculated for each of PYTHIA and ISAJET, Luminosity = $10^5 pb^{-1}$ over one year) results of the particle-level jet-profile-based Z reconstruction with 150% smearing are presented. Cuts on the P_T (>150 GeV) of the reconstructed jet pair core region and on core separation (<1.0) are implemented for all cases. The Higgs mass window extends from 460 to 740 GeV/c^2, the Z mass window extends from 81 to 101 GeV/c^2, P_{Tcore} and P_{Tmu} refer to the transverse momenta of the jet-jet core and the muon pair respectively.

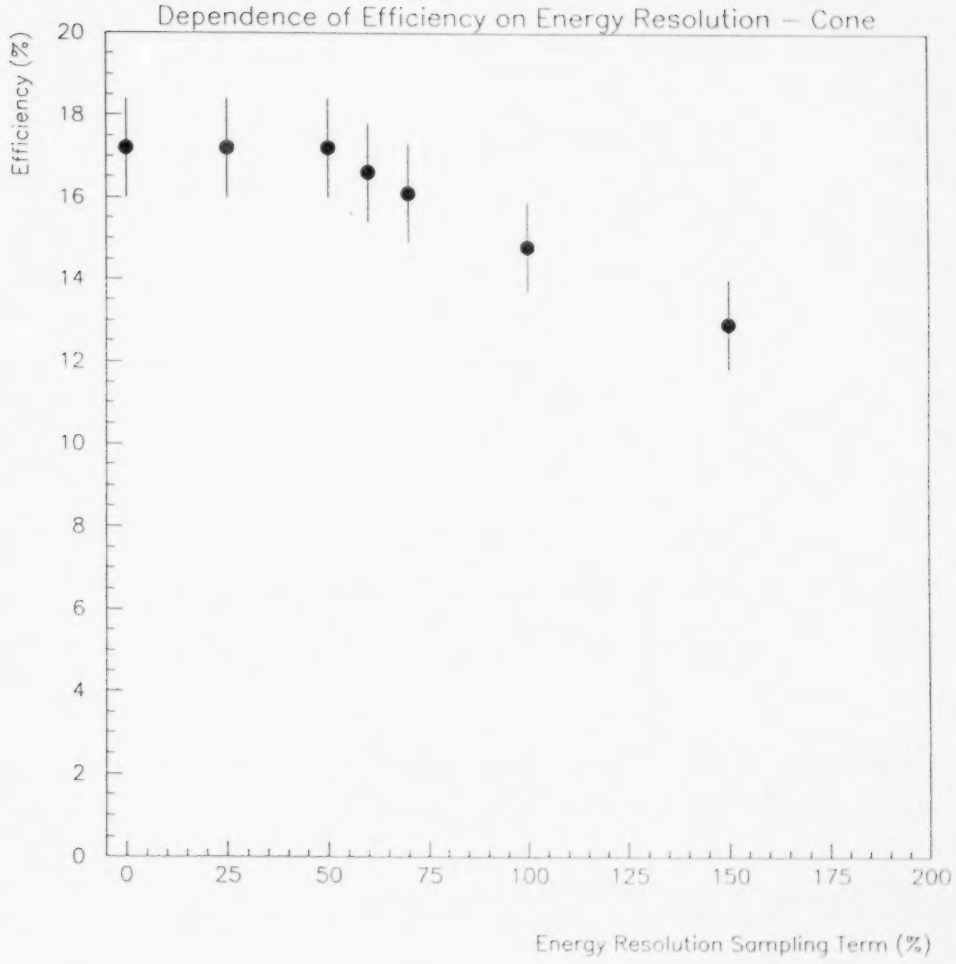

Figure 4.13: Efficiency vs. detector energy resolution for Higgs particles as reconstructed from two jets using jet-jet profile technique.

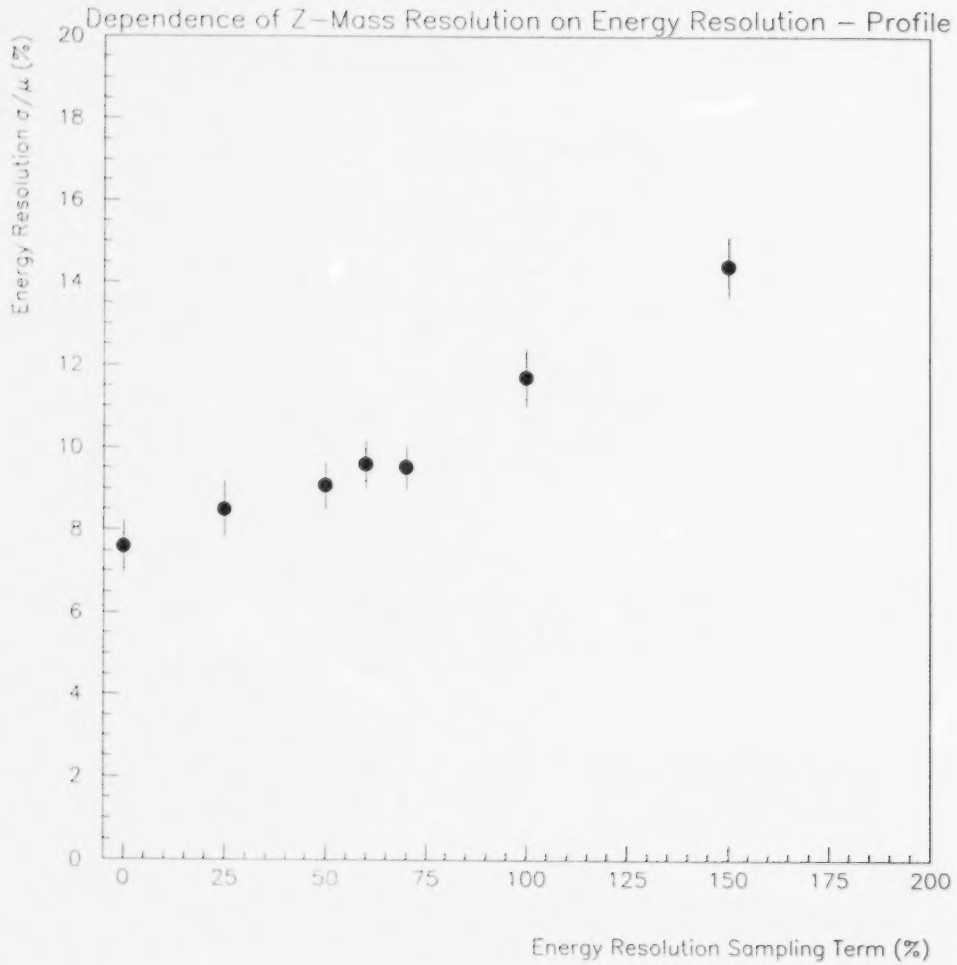

Figure 4.14: Z mass resolution vs. detector energy resolution for jet-jet profile technique.

these results show that, although the profile algorithm still provides a significant improvement in signal identification, its performance suffers noticeably. It should be noted, however, that this smearing study does not take into account a constant or noise term in the calorimeter energy resolution.

It is also interesting to check the performance of this algorithm for different Higgs boson masses. The range of masses in which this type of analysis (on this particular signal) would be used is about 600 GeV/c^2 to 1 TeV/c^2. With this is mind, the signal efficiency performance of this analysis technique is plotted versus Higgs mass in Figure 4.15 for the case in which no smearing is added. The results show that the efficiency for signal detection increases with increasing Higgs mass. A possible explanation for this improvement is that the Z produced from a heavier Higgs particle will produce a more collimated jet than will a Z from a low mass Higgs particle. This means that more events would pass the cut requiring a low transverse momentum fraction in the jet halo region. However, it is expected that, due to a lower cross-section at high mass (almost a factor of 4 between 600 GeV/c^2 and 1 TeV/c^2), the significance of the signal will worsen with increasing Higgs mass, despite this improvement in efficiency.

4.6.2 K_T Clustering Analysis, Including Effects of Energy Resolution

The K_T clustering algorithm was applied to the same 10000 background and 1000 signal events as for the profile analysis for each of the three energy resolutions. The results are summarized in Table 4.7 for the case with no smearing, Table 4.8 for a $50\%/\sqrt{E}$ resolution and Table 4.9 for a $150\%/\sqrt{E}$ resolution.

Again the evolution of algorithm performance with worsening detector energy

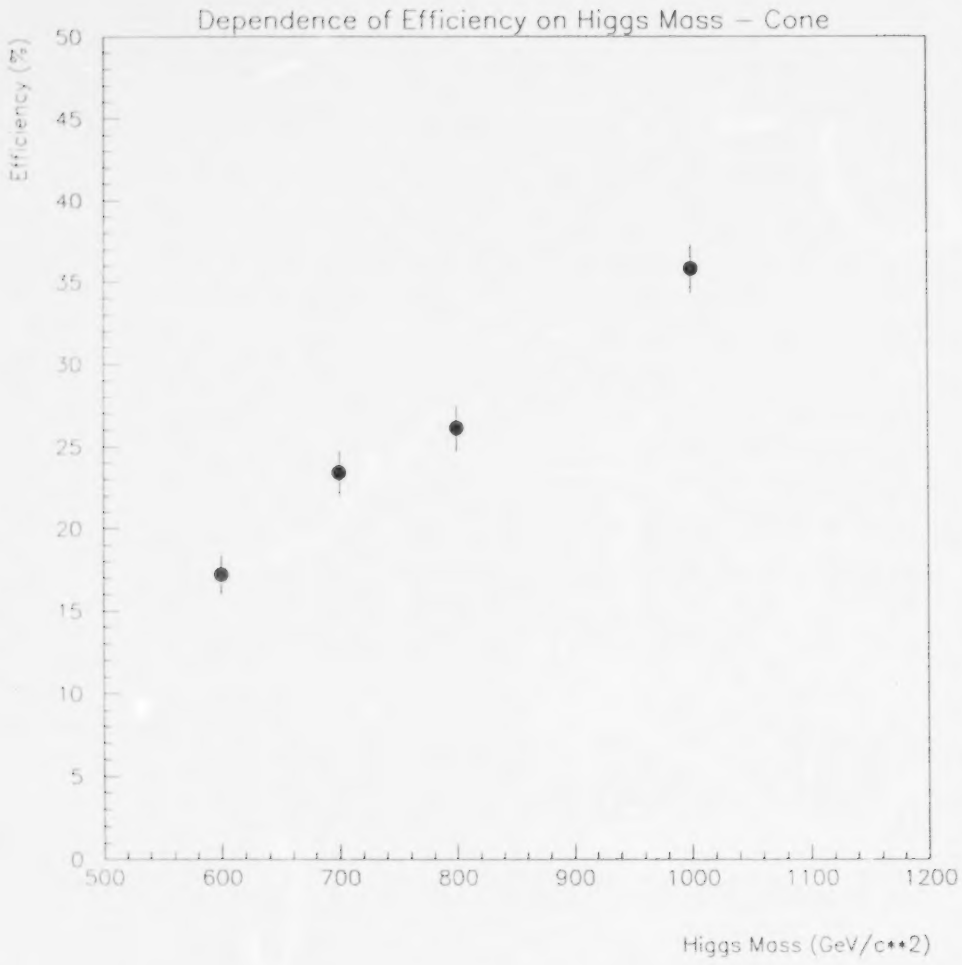

Figure 4.15: Algorithm performance versus Higgs mass for the case in which no smearing was applied. The error bars reflect statistical errors.

1000 signal 10000 backgrnd		No. Pass	Reject.	Eff.	Enhance	$S/\sqrt{B}$ PYTHIA	$S/\sqrt{B}$ ISAJET
H mass window	S	725		72.5%			
	B	2394	76.1%		3.0	2.1	3.0
Z, H mass windows	S	609		60.9%			
	B	1583	84.17%		3.8	2.2	3.1
Z, H mass windows	S	457		45.7%			
$P_{Tmu} > 200$ GeV	B	646	93.54%		7.1	2.6	3.6
Z, H mass windows	S	334		33.4%			
Jetcone > 0.5	B	171	98.29%		19.5	3.6	5.1
Z, H mass windows	S	241		24.1%			
Jetcone >0.5	B	75	99.25%		32.1	4.0	5.6
$P_{Tmu} >200$ GeV							

Table 4.7: Rejection, efficiencies, enhancements and Signal/$\sqrt{background}$ (for background cross-sections calculated for each of PYTHIA and ISAJET, Luminosity = $10^5 pb^{-1}$ over one year) results of the particle-level K_T clustering-based Z reconstruction with no smearing are presented. A cut on the P_T (>150 GeV) of the reconstructed Z jet is implemented for all cases. The Higgs mass window extends from 438 to 762 GeV/c^2, the Z mass window extends from 81 to 101 GeV/c^2, P_{Tmu} refers to the transverse momenta of the the muon pair.

1000 signal 10000 backgrnd		No. Pass	Reject.	Eff.	Enhance	$S/\sqrt{B}$ PYTHIA	$S/\sqrt{B}$ ISAJET
H mass window	S	719		71.9%			
	B	2458	75.4%		2.9	2.1	2.9
Z, H mass windows	S	604		60.4%			
	B	1621	83.8%		3.7	2.1	3.0
Z, H mass windows	S	453		45.3%			
$P_{Tmu} > 200$ GeV	B	650	93.5%		7.0	2.5	3.6
Z, H mass windows	S	334		33.4%			
Jetcone > 0.5	B	187	98.1%		17.9	3.4	4.9
Z, H mass windows	S	244		24.4%			
Jetcone >0.5	B	100	99.0%		24.4	3.5	4.9
P_{Tmu} >200 GeV							

Table 4.8: Rejection, efficiencies, enhancements and Signal/$\sqrt{background}$ (for background cross-sections calculated for each of PYTHIA and ISAJET, Luminosity = $10^5 pb^{-1}$ over one year) results of the particle-level K_T clustering-based Z reconstruction with 50% smearing are presented. A cut on the P_T (>150 GeV) of the reconstructed Z jet is implemented for all cases. The Higgs mass window extends from 438 to 762 GeV/c^2, the Z mass window extends from 81 to 101 GeV/c^2, P_{Tmu} refers to the transverse momenta of the the muon pair.

1000 signal 10000 backgrnd		No. Pass	Reject.	Eff.	Enhance	$S/\sqrt{B}$ PYTHIA	$S/\sqrt{B}$ ISAJET
H mass window	S	717		73.1%			
	B	2689	71.7%		2.7	2.0	2.8
Z, H mass windows	S	556		55.6%			
	B	1748	82.52%		3.2	1.9	2.7
Z, H mass windows	S	415		41.5%			
$P_{Tmu} > 200$ GeV	B	632	93.7%		2.4	2.4	3.3
Z, H mass windows	S	274		27.4%			
Jetcone > 0.5	B	228	97.3%		12.0	2.4	3.3
Z, H mass windows	S	210		21.0%			
Jetcone >0.5	B	95	97.9%		22.1	2.1	2.9
$P_{Tmu} >200$ GeV							

Table 4.9: Rejection, efficiencies, enhancements and Signal/$\sqrt{background}$ (for background cross-sections calculated for each of PYTHIA and ISAJET, Luminosity = $10^5 pb^{-1}$ over one year) results of the particle-level K_T clustering-based Z reconstruction with 150% smearing are presented. A cut on the P_T (>150 GeV) of the reconstructed Z jet is implemented for all cases. The Higgs mass window extends from 438 to 762 GeV/c^2, the Z mass window extends from 81 to 101 GeV/c^2, P_{Tmu} refers to the transverse momenta of the the muon pair.

resolution is examined via plots of efficiency and z mass resolution versus detector energy resolution. These results are shown in Figures 4.17 and 4.16. These results show that the performance of the K_T clustering algorithm in distinguishing signal from background remains basically unchanged with moderate smearing, but then degrades significantly when the smearing is increased above about 70%. Also, as in the case of the profile algorithm, with 150% resolution, the PYTHIA-calculated $S/\sqrt{B}$ drops to about 2/3 of its value at 50% energy resolution (3.5 to 2.1).

As in the profile study, the results of the clustering analysis imply that the ATLAS design goal of a 50% sampling term is acceptable with regards to the performance of this algorithm. Again, however, if this design goal is not met the performance of the algorithm suffers considerably.

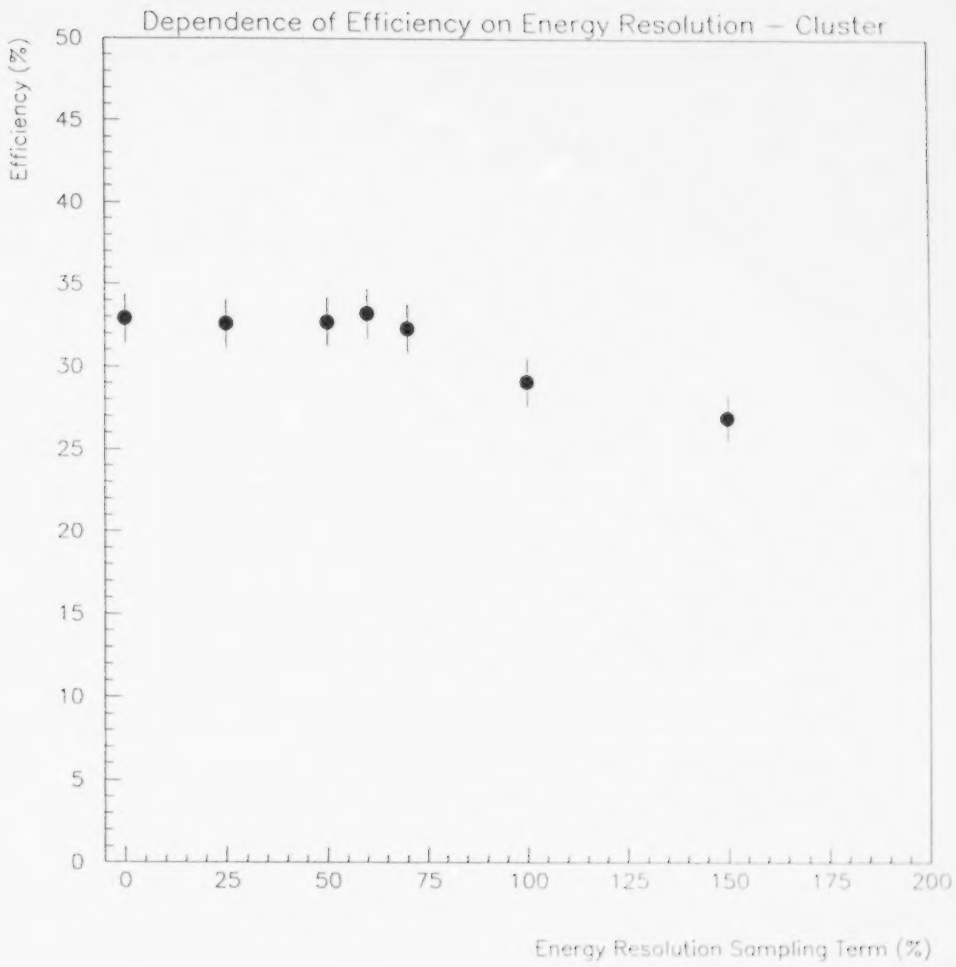

Figure 4.16: Efficiency vs. detector energy resolution for Higgs particles as reconstructed from two jets using the jet clustering technique.

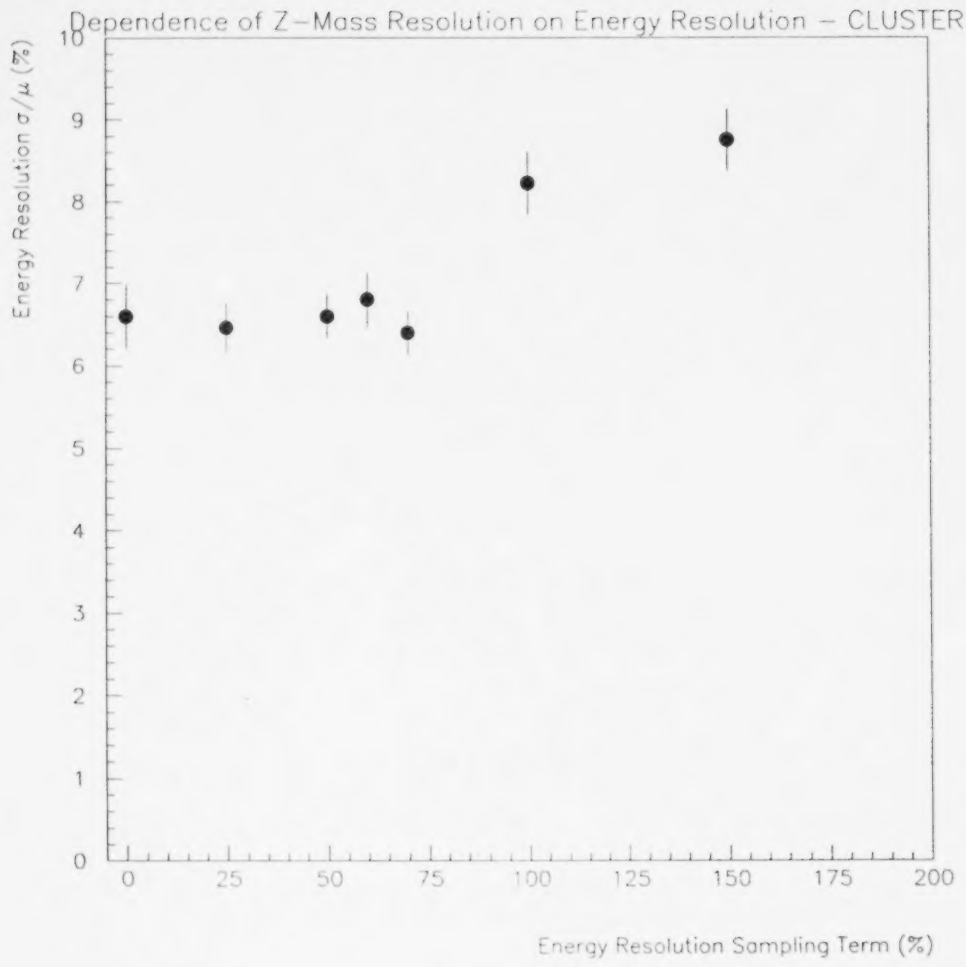

Figure 4.17: Z mass reconstruction resolution vs. detector energy resolution for Higgs decays as reconstructed from jets using the K_T clustering technique.

CHAPTER 5

General Conclusions

In this thesis, two major types of detector simulation tests have been performed for the ATLAS detector. The first involves a series of tests of the performance of the end-cap detector in the presence of pile-up effects. The second is the simulation of a heavy Higgs signal and its dominant background in ATLAS.

In the first type of test, three separate simulation studies have been performed. The first is a study of the effects on energy resolution of varying the longitudinal segmentation of the end-cap in the presence of pile-up effects. The second study again analyzes energy resolution in the presence of pile-up, this time with a varying detector granularity. The final study is similar to the previous two, except that the geometrical property that is varied is the copper absorber thickness in the back wheel of the hadronic end-cap. In all three of these studies, it was found that the variation of these geometrical properties had little effect on energy resolution in the presence of pile-up.

In the study of the $H \rightarrow ZZ \rightarrow \mu\mu jj$ signal (and its Z + jets background) in ATLAS, two different jet finding techniques are applied and compared. The analysis based on the jet-jet profile technique was found to give superior performance on this signal ($S/\sqrt{B} = 6.0$) when compared to the analysis based on the K_T clustering technique ($S/\sqrt{B} = 2.2$). However, with further optimization, it is hoped that K_T clustering can produce results competitive with the jet-jet profile analysis. A comparison of full-simulation and particle-level results for each of these techniques shows

that the particle-level results are good predictors of full simulation performance. A study of algorithm performance as a function of calorimeter energy resolution shows that a resolution of approximately 50-70% is the maximum acceptable to maintain the best performance of these algorithms.

The performance of these algorithms would be expected to degrade in the presence of pile-up (not considered here), however, in this analysis, only Z reconstruction techniques were used to distinguish Higgs signals from background, no other information has been used. For example, the use of a forward jet tag in conjunction with these techniques would be expected to further improve the results. The next stage in this analysis is to include pile-up effects and forward jet tagging in the study in order to better estimate the performances of the algorithms under more realistic conditions.

In summary, the performance of the ATLAS hadronic end-cap in the presence of pile-up effects is not significantly effected by altering any of the design parameters considered here. Since this is true and it has been shown in previous [19] [20] studies that the technical proposal design meets the stated ATLAS calorimetry design goals, the first type of detector design requirement is successfully tested. Also, it is possible to get an acceptable signal/background in a potentially important physics channel (heavy Higgs), meeting the second detector requirement. So, although extensive simulation work in these areas will, of course, continue, the performance of the ATLAS hadronic end-cap is satisfactory in both major elements of design.

Bibliography

[1] Hall, Nina, A Supercollider for Europe,*New Scientist* v.131, p. 35-9, July 27, 1991.

[2] Glashow, S.L., Nucl. Phys. 22, 579 (1961).

[3] Weinberg, S., Phys. Rev. Lett. 19, 1264 (1967);

[4] Salam, A., *Elementary Particle Theory*, N. Svartholm, ed. (Stockholm: Almquist and Wiksell, 1968).

[5] Coughlan, G.D. and Dodd, J.E., *The Ideas of Particle Physics: An Introduction for Scientists*, Cambridge University Press, Cambridge, 1991.

[6] Quigg, Chris, *Gauge Theories of the Strong, weak, and Electromagnetic Interactions*, Addison-Wesley, Reading, Massachusetts, 1993.

[7] Jenni, P. and White, J., Physics and Experimental Challenge of Future Hadron Colliders, *Proceedings of a lecture series given at Eigth Lake Louise Winter Institute*, Lake Louise, Alberta, Canada, February, 1993.

[8] Gelmini, G., Beyond the Standard Model, *Proceedings of the Eigth Lake Louise Winter Institute*, Lake Louise, Alberta, Canada, February, 1993.

[9] Macpherson, A., *Issues in Symmetry Breaking in Superunification*, Phd. Thesis, University of Alberta, 1996.

[10] Gunion, J. et al., *The Higgs Hunter's Guide*, Addison-Wesley, Redwood City, California, 1990.

[11] Pinfold, J. and Sinervo, P., The TeV Physics Frontier: Probing the Microcosm, *Physics in Canada*, v.50, no.2, p. 175-189, march/april, 1994.

[12] LHC Yellow Book 1995.

[13] ATLAS Collaboration, *ATLAS Technical Proposal for a General-Purpose pp Experiment at the Large Hadron Collider at CERN*, December 15, 1994.

[14] Rolnick, N.B., The Fundamental Particles and their Interactions, Addison-Wesley, 1994.

[15] Collins, P.D.B. and Martin, A.D., *Hadron Interactions (Graduate Student Series in Particle Physics*, AdaM Hilger Ltd., Technohouse, Redcliff Way, Bristol BS1 6NX, 1984.

[16] Perkins, D.H., *Introduction to High Energy Physics*, Addison-Wesley, Menlo Park, California, 1987.

[17] Gingrich, D. et al., ATLAS Collaboration, *ATLAS Letter of Intent for a General-Purpose pp Experiment at the Large Hadron Collider at CERN*, CERN/LHCC/92-4.

[18] Colas, J. et al., The Electrostatic Transformer, *Nuclear Instruments and Methods in Physics Research*, A294, p.583-590, 1990.

[19] Kiryunin, A., Optimization of the Hadronic End-Cap Calorimeter from the Point of View of Jet Energy Measurement, *ATLAS Internal Note, CAL-NO-083*, March 10, 1996.

[20] Davis, R.A, O'Neil, D.C., Savard, P., Energy Resolution of Jets in the Presence of Pileup Noise in the End-Cap Calorimetry, *ATLAS Internal Note, Calorimetry Note* Submitted July 30, 1996 (Appendix A).

[21] Amorim, A., *Monte Carlo Interface Using GENZ*, ATLAS software group, CERN, Geneva.

[22] Sjostrand, T., *Pythia 5.7 and Jetset 7.4 Physics and Manual*, CERN-TH.7112/93, December 1993 (Revised February 1994).

[23] Giele, Walter, *VECBOS Homepage*, http:// fnth02.fnal.gov /people /giele /vecbos.html .

[24] DESY 91-048, Cavendish HEP 90/26, Comput. Phys. Commun. 67, (1992), 465.

[25] Giele, Walter, *NJETS Homepage*, http: / / fnth02.fnal.gov /people /giele /njets.html .

[26] Paige, F.E. and Protopopescu, S.D., *A Monte Carlo Event Generator for PP and PBAR-P Reactions*, Brookhaven National Laboratory, Upton, NY 11973, USA.

[27] CERN Application Software Group, *Detector Description and Simulation Tool*, CERN program library, Q123, 1993.

[28] ATLAS Offline Software Group, *DICE Manual*, http: / /atlasinfo.cern.ch /Atlas /GROUPS /SOFTWARE /DOCUMENTS /DICE_MANUAL_old /dice_manual /dice_manual.html, February 1, 1995.

[29] Dewolf, R. and Nevski, P., Geometry Saving and User Input in Slug, *ATLAS Software Note 001*, CERN.

[30] Barger, V. et al., Comparative Study of the Benefits of Forward Jet Tagging in Heavy Higgs Production at the Superconducting Super Collider, *Physics Review D*, v.44, no.5, p. 1426-1437, September 1, 1991.

[31] Seymour, M., Searches for New Particles Using Cone and Cluster Jet Algorithms: A Comparative Study, *Lund Note*, June 1993.

[32] Field, D. and Griffin, P.A., Enhancing the Heavy Higgs Signal with Jet-Jet Profile Cuts, *Physical Review D*, v.48, no.7, p. 3167-3173., October 1, 1993.

[33] Macpherson, A.L., O'Neil, D.C., Pinfold, J.L, ATLAS Note in Progress.

[34] Ellis, S.D. and Soper, D.E., Successive Combination Jet Algorithm for Hadron Collisions, *CERN Theory Note*, CERN-TH.6860/93, April 1993.

[35] Visser, E.J., The New Pattern Recognition (MUONBOX), *World Wide Web Document at http://atlasinfo.cern.ch /Atlas /GROUPS /SOFTWARE /DOCUMENTS /MUONBOX /newPatRec.html*, September 29, 1995.

[36] Zmushko, V. et al., Study of $H \rightarrow WW \rightarrow l\nu jj$ and $H \rightarrow ZZ \rightarrow lljj$ Decays for $m_h = 1$ TeV, *ATLAS Internal Note*, PHYS-No-008, November 3, 1992.

Appendix A

Jet Simulation Study

ATLAS Internal Note
CAL-NO-XXX
30 July 1996

Energy Resolution of Jets in the Presence of Pileup Noise in the Endcap Calorimetry

FINAL DRAFT

R.A. Davis and D. O'Neil
Centre for Subatomic Research
University of Alberta
Edmonton, Alberta
Canada
T6G 2N5

P. Savard
Laboratoire de Physique Nucléaire
Université de Montréal
Montréal, Québec
Canada
H3C 3J7

July 30, 1996

A.1 abstract

The energy resolution of jets in the endcap liquid argon calorimeters is studied. Energy resolution results are obtained using two different hadronic transport codes, GCALOR and GEANT-FLUKA. The combined effects on the resolution of the magnetic field, inner detector material, cone size used in reconstruction, and the effect of jet to jet shower evolution differences are discussed. Finally, the effect of minimum bias pileup noise on the jet energy resolution in the endcap is investigated and a series of cuts designed to reduce the impact of pileup noise are introduced.

A.2 Introduction

The energy resolution achieved for jets in the ATLAS calorimetry system will be affected by many factors including the amount of material in front of the calorimeters, minimum bias pileup noise, the algorithms and cuts used in the reconstruction, and the quality of the calibration. While neglecting these effects can be useful when designing a calorimeter, the "intrinsic jet resolution" thus obtained will be very different than the resolution attained by the actual system used to make physics measurements. Previous notes [2] [3] [7] [8] have reported results in which many, if not all, of the above effects were neglected. The study presented in this note attempts to obtain a more realistic estimate of the actual jet resolution of the ATLAS endcap calorimeters by including some of the detector effects mentioned above.

In this study, fully simulated $d\bar{d}$ dijet events were used to measure the energy resolution of the calorimeters. The generation method used for these jets is described in section A.3 of this note. In section A.4, the calibration and reconstruction methods which were used to define and compare the energy of the jets at the vertex to the energy seen in the calorimeter are described.

The results of the energy resolution analysis are presented in section A.5. The effects of the material and magnetic field on the resolution are evaluated as well as the contribution due to jet to jet differences which include fluctuations in the shape, particle content, and energy spectrum of the jets. The energy resolution of jets when all of the above effects are included is then presented for various reconstruction cone sizes. The behaviour of the calibration weighting constants is also discussed. In order to better understand the results for jets, single particle energy resolutions as well as e/π and e/h ratios are given.

Section A.6 presents the study of the energy resolution in the presence of minimum bias pileup noise. The section begins with a description of the pileup inclusion method and of the cuts applied. The jet scale and energy resolution with pileup noise is then evaluated for different cone sizes and cell level energy cuts. Following the presentation of the results a discussion of their implications for physics analysis is presented in section A.7.

A.3 Generation of the Data Sample

For the purposes of this study, $d\bar{d}$ dijet events were generated using ATGEN/PYTHIA version 5.7 at transverse energies of 15, 40, 60, 80, 100, 120 and 180 GeV. For each of these energies, 500 dijets were produced at each of η=2.1, η=2.3, and η=2.5. Dijets were selected for this study due to their more realistic angular energy distribution and particle multiplicity when compared to single jets as reported by Cozzi and Perini [3]. Single jets, which have been commonly used for calibration of the calorimeters in the simulation, are unrealistically narrow in angular scope and can be misleading when used for studies which take into account jet cone size.

The minimum bias four vectors used to generate fully simulated pileup events were also generated with ATGEN/PYTHIA version 5.7. A total of 5000 minimum bias events were prepared using the datacards shown in table A.1.

Both the dijet and minimum bias four vectors were passed through the detector simulation using DICE version 2.04 and GEANT version 3.2130. The GEANT default energy threshold cuts were applied during the full simulation of the dijets. A modified version of the ATL-TP3 datacard which removed the endcap preshower and moved the electromagnetic and hadronic calorimeters 7 cm closer to the interaction point in

MSEL=1	Jet production $2 \rightarrow 2$ processes.
MSTP(2)=2	2^{nd} Order running α_s.
MSTP(33)=3	K-factor.
MSTP(81)=1 MSTP(82)=4	Multiple interactions with varying impact point.
MSTJ(22)=2	Particle decays only if $\tau \geq$ 10nm.

Table A.1: Data cards used in the production of minimum bias events using ATGEN/Pythia.

z was used. This endcap configuration corresponded to the design specification of the ATLAS Technical Proposal [1]. All detector components in the simulation conformed to the standard ATL-TP3 geometries except for a new hadronic endcap module. This geometry included all inter-plate gaps as well as the copper/kapton electrodes inside the liquid argon. The definition of individual detector elements in the hadronic endcap geometry allowed the use of real calorimeter cells and not the perfectly projective (η,ϕ) bins present in the standard TP3 geometry. The granularity of the electromagnetic calorimeter was $\Delta\eta \times \Delta\phi = 0.025 \times 0.025$ with three longitudinal segments. The hadronic calorimeter had four longitudinal segments and a granularity of $\Delta\eta \times \Delta\phi = 0.05 \times 0.1$ from η=1.5 to η=1.8 and 0.1×0.1 from η=1.8 to η=3.2. The hadronic endcap geometry followed the specifications of the engineering diagram shown in figureA.1.

For the study involving single particles, the γ threshold was set at 100 KeV and the hadronic threshold was set at 1 MeV. The geometry used was a standalone version of GEANT which included the detailed description of the hadronic calorimeter

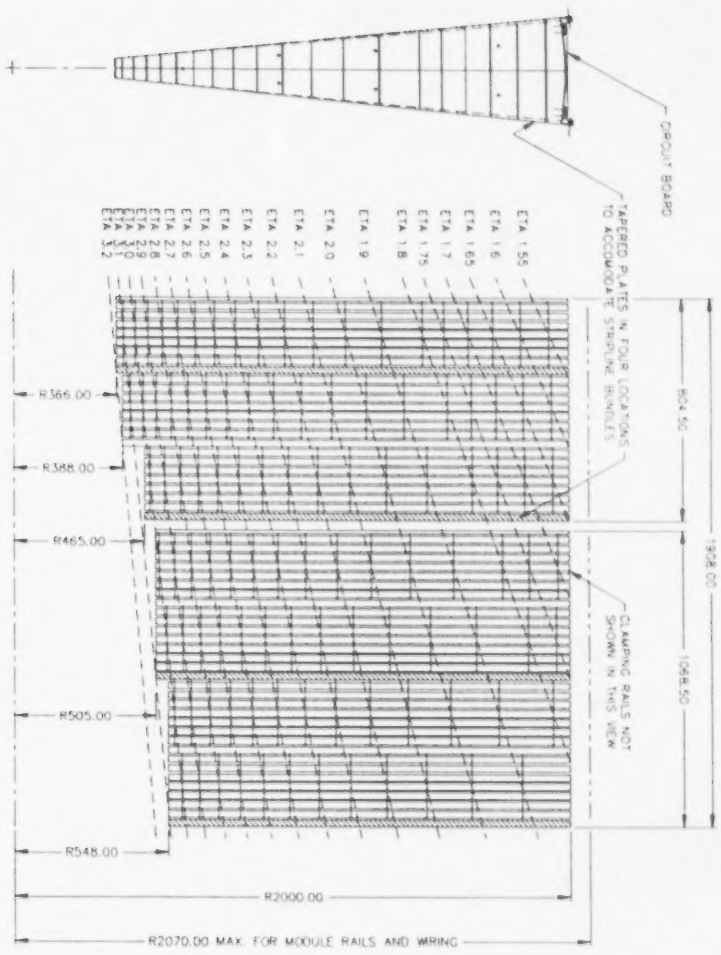

Figure A.1: A cross section of the hadronic endcap geometry which was simulated for the production of data used in this note. This geometry included all inter-plate gaps and Cu/Kapton electrodes.

described previously without any other material present. The material of the rest of the ATLAS detector was excluded from the single particle study in order to extract the intrinsic parameters of the hadronic endcap calorimeter.

As previously reported by the authors [4], important differences have been found between jet energy resolutions measured using different hadronic transport codes. In order to investigate these differences, the jet production (but not the minimum bias production) was duplicated for each of two hadronic transport packages: GEANT-FLUKA and GCALOR. The default hadronic transport code used in DICE, GHEISHA, was not used in the jet simulation.

A.4 Jet Reconstruction and Calibration Procedure

The "true" energy, E^{true}, of the jets was defined at the particle level as the energy of the particles at the vertex contained in a cone of given $\Delta R = \sqrt{\Delta\eta^2 + \Delta\phi^2}$ centred around the initial parton's direction. Thus, E^{true} has a maximum of the original parton energy if all of the initial jet particles are contained within the cone. A true jet finding algorithm was not used as the goal of the study was to measure the jet energy resolution around a specific η centre. The value of E^{true} was used as the target energy of the jet in the calibration procedure. The deposited energy in each longitudinal segment of the electromagnetic (ENDE) and hadronic (ENDH) endcap calorimeters was summed over all cells in a cone of given $\Delta R = \sqrt{\Delta\eta^2 + \Delta\phi^2}$ centred around the direction of the original parton. Near the boundary of the cone, a cell was included in the sum if the position of its centre fell within the required radius.

The total reconstructed energy, E_j^{recon}, of the j^{th} jet in the sample was determined by the equation:

$$E_j^{recon} = \sum_{i=1}^{7} a_i E_i^{raw}$$

where E_i^{raw} is the raw energy deposited in the i^{th} longitudinal segment of the calorimeter, and a_i is the calibration constant of the i^{th} longitudinal segment. The endcap calorimeter was divided into seven longitudinal segments with segments 1-3 belonging to the electromagnetic endcap calorimeter and segments 4-7 belonging to the hadronic endcap calorimeter.

The calibration constants a_i were determined through minimization of the function:

$$F = \sum_{j=1}^{M} (E_j^{recon} - E_j^{true})^2$$

where there were M jets in the sample and E_j^{true} was the "true" energy of the jet in the cone at the vertex as explained above.

The minimization procedure was applied in an iterative manner. For the first iteration, the calibration constants were set at an initial guess, and the recontructed energy E_j^{recon} was calculated for each jet. A gaussian distribution was then fit to the spectrum of $E_j^{recon} - E_j^{true}$ giving a standard deviation σ. Events with $|E_j^{recon} - E_j^{true}| < 3\sigma$ were then transferred to the minimization procedure in order to find new calibration constants.

After this initial minimization, the values of E_j^{recon} were recalculated using the new calibration constants and the distribution of $E_j^{recon} - E_j^{true}$ was again fit with a gaussian in order to obtain a new width σ. Events with $|E_j^{recon} - E_j^{true}| < 3\sigma$ were again selected and resubmitted to the minimization procedure in order to generate better calibration constants. This procedure was repeated until the σ obtained from

the fit to the $E_j^{recon} - E_j^{true}$ distribution changed by less than 1% between iterations. The calibration program typically repeated this procedure four times in order to arrive at a stable value of σ. These final calibration constants were then applied to the entire data sample less those events for which E^{recon} was less than 80% of E^{true}. Typically this final set consisted of 90% of the original number of jets. Those jets which had E^{recon} less than 80% of E^{true} were due to emission of a hard gluon such that a cone centered on the original parton direction was missed by most of the particles.

Due to the presence of tails in the energy distributions for small cone sizes, the final σ for the energy resolution calculation was given by a gaussian fit in the range of -1.5σ to $+3\sigma$ to the final $E_j^{recon} - E_j^{true}$ distribution. The energy resolution for a given jet energy and cone size was then calculated as this σ divided by the nominal generation energy of the jets.

A.5 Energy Resolution Results

A.5.1 Exterior Contributions to the Energy Resolution

In the following section, an attempt is made to isolate and measure various contributions to the energy resolution of the jets at the particle level. The effects of the jet shape and particle content as well as the detector material preceeding the calorimeter and magnetic field are studied.

In order to compare the energy in the jet cone at the vertex with the energy in the same cone after the particles of the jet had passed through the detector material preceeding the calorimeters, the subroutine GUSTEP of the DICE program was modified. Using a simulation which included only the inner tracker, the

solenoid coil, the endcap cryostat, and with the full magnetic field, the jet particles were stopped at the interface between the cryostat and the electromagnetic endcap calorimeter. The stopped particles were then binned in an array with a granularity of $\Delta\eta \times \Delta\phi = 0.1 \times 0.1$ for further analysis.

Contribution of Muon and Neutrino Content

Previous authors [2] removed the energy contribution of the muons and neutrinos present in the jet when calculating the intrinsic energy resolution of the calorimetry. In this study, the energy deposition due to muons and neutrinos was measured by stopping them as described in the preceeding paragraph. The measurement of the muon and neutrino energy contribution was performed both at the vertex and the endcap calorimeter face in an attempt to take into account the decay of pions in the detector preceeding the calorimetery. The contribution of neutrinos and muons to the total jet energy is small, on average less than 1%. The rms of the neutrino and muon energy distribution was measured to be 2 GeV for a 75 GeV jet.

Contribution of Inner Tracking, Dead Material, and Magnetic Field

The effect of the tracking and dead material preceding the calorimeter was measured for five dijet transverse energies: 15, 40, 60, 100, and 120 GeV E_{T}. The measurements were repeated for two cones sizes, ΔR= 0.5 and 0.7, both centred at $\eta = 2.3$. The average value of the energy lost in the inner tracking and cryostat, including energy that exits the cone, is shown in figure A.2 for these five energy points. The rms of the difference between the energy of the jet at the vertex and at the calorimeter face is also plotted in figure A.2 for the five energy points. The rise of the rms as a function of the jet energy demonstrates that for jets, the contribution of the material to the

energy resolution cannot be included solely in the noise or material term (c/E). This is due to fluctuations in the number of particles and the specific particle content of each jet as well as to the increase in the average number of particles in a jet as a function of energy. Although the use of single particles would allow the material term to be measured more precisely, pileup and electronic noise will dominate this term in the resolution even at low luminosity as is shown in section A.6. Figure A.3 shows the contribution of energy loss in the inner detector material and energy leakage from the cone to the energy resolution. The resolution plot is fit with the following equation:

$$\frac{\sigma}{E} = \frac{a}{\sqrt{E}} \oplus b \oplus \frac{c}{E}$$

where a corresponds to the sampling term, b the constant term, and c the material term. The results of this fit are also shown in figure A.3. The near zero constant term is expected since the exact energy of the particles in the jet are extracted from GEANT before they enter the calorimeter. What is shown are the fluctuations of the energy exiting the cone or lost in the material. The fit also shows the important contributions of the inner detector material and the cone energy leakage to the sampling term in the case of jets. The effect of the magnetic field alone on the jet energy resolution was found to be negligible.

Jet to Jet Fluctuations

The effects of fluctuations in the multiplicity, energy distribution, and angular scope of the particles comprising a jet on the energy resolution were also considered. In order to measure these effects, the same dijet (formed from the same initial particles) was passed through the detector simulation 500 times with different initial random seeds. This procedure was used to provide two sets of 500 "identical" jets at each of four

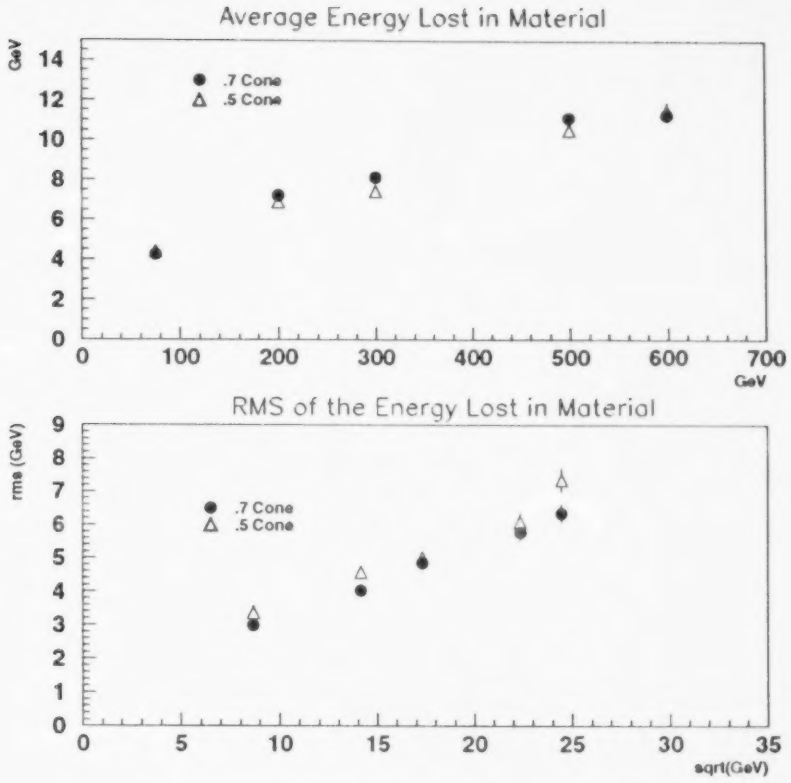

Figure A.2: The top plot shows the average energy lost in the inner tracking and dead material preceeding the calorimeter as a function of jet energy. This average also includes energy lost due to particles leaving the cone radius. The triangles show results for a cone size of ΔR=0.5 while the circles show results for ΔR=0.7. The rms of the energy lost in the inner tracking and dead material preceeding the calorimeter as a function of the square root of the jet energy is shown in the bottom plot. The rms also includes energy lost due to particles leaving the cone radius. Again, the triangles show results for a cone size of ΔR=0.5 while the circles show results for ΔR=0.7. All cones are centred at $\eta = 2.3$.

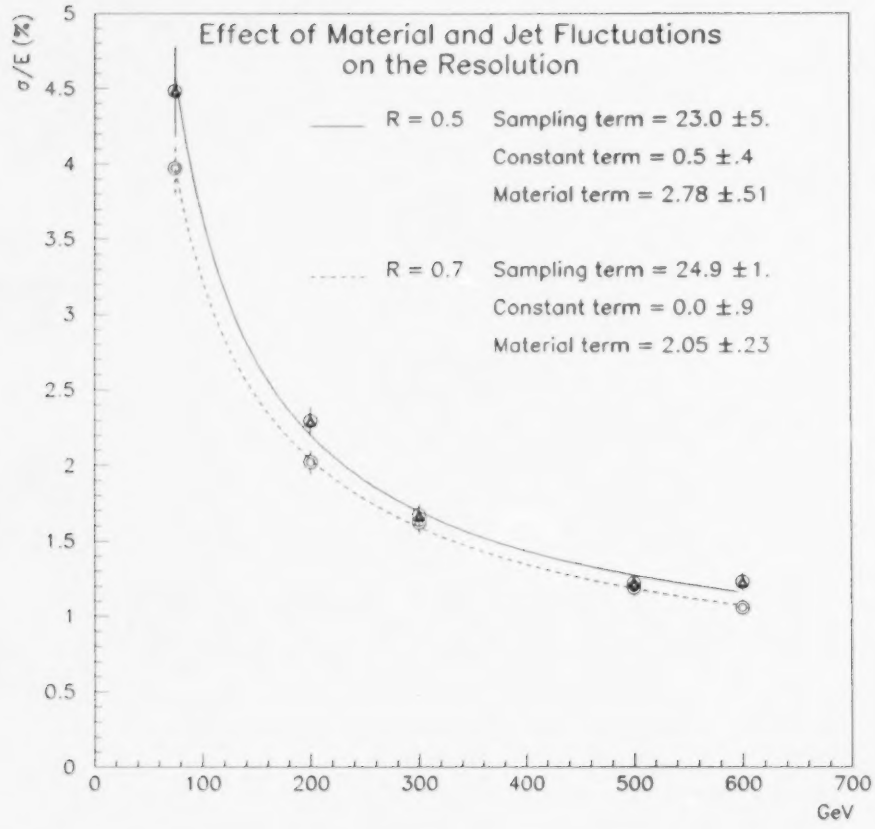

Figure A.3: The contribution of energy loss in the inner tracking and energy leakage from the cone to the energy resolution of the endcap calorimeter. The solid line shows results for a cone size of ΔR=0.5 while the dashed line shows results for ΔR=0.7. Both cones are centred at $\eta = 2.3$.

transverse energies: 15, 40, 60, and 120GeV E_T at $\eta = 2.3$ using GEANT-FLUKA. The calibration and reconstruction of these jets followed the method of section A.4. In order to simulate a "typical" jet at each of the above transverse energies, three different "identical" dijets were passed through the detector simulation 500 times each and the final energy resolution taken to be the mean of the three σ/E values obtained from these distributions. Figure A.4 shows the average energy resolution of these "identical" jets as compared to the resolution for a set of 500 jets each with different initial particle content. The fit is made using the material term shown in figure A.3 for a ΔR=0.7 cone. The results of the fit show that the sampling term receives contributions from the jet fluctuations. It must be kept in mind, however, that both of the curves in figure A.4 contain contributions from both material effects and jet to jet fluctuations, and hence the difference in sampling terms between the curves in this figure is not due entirely to jet to jet differences.

A.5.2 Jet Energy Resolution of the Endcap Calorimeter

In order to facilitate a comparison of the energy resolution results obtained from this study with those of previous studies, the energy resolution of the entire endcap was measured using all energy deposited in the calorimeters between $\eta = 1.5$ and $\eta = 3.2$ in the reconstruction procedure. The "true" jet energy was determined accordingly as the total generator energy at the vertex directed between these two η values. The results of the reconstruction, which followed the procedure of section A.4 taking into account three segments of the ENDE and four segments of the ENDH, is shown in figure A.5 for GEANT-FLUKA (circles) and for GCALOR (squares). The sampling and constant terms for the whole calorimeter are determined by a fit to the following equation:

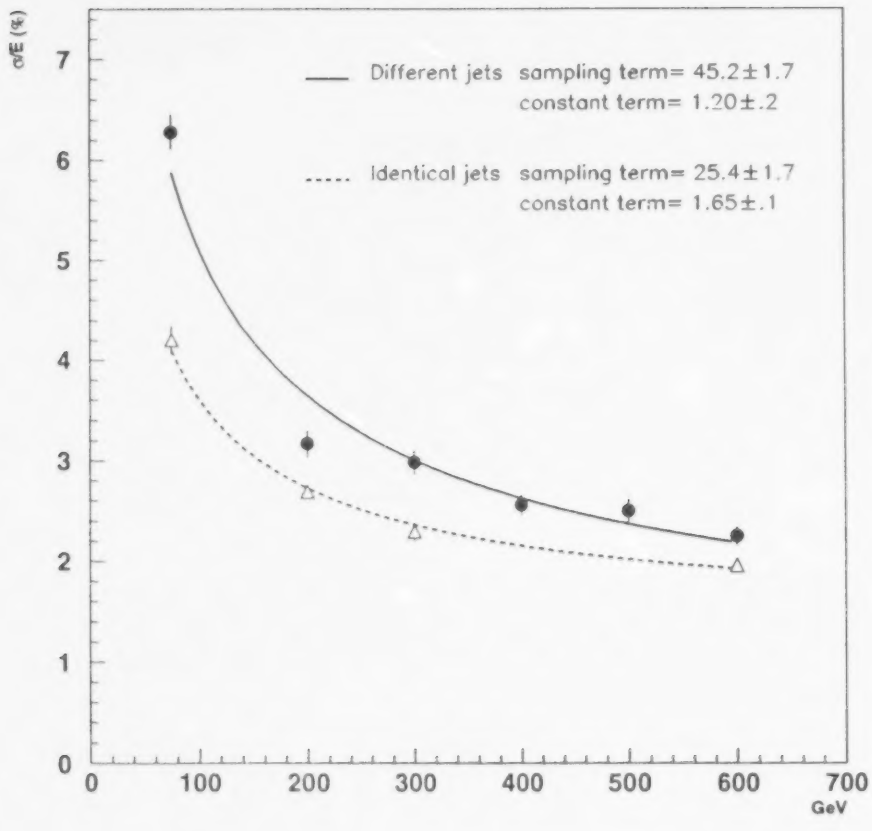

Figure A.4: A comparision of the energy resolution for jets with identical initial particle content (dashed line) and different initial particle content (solid line). The energy resolutions shown are for a ΔR=0.7 cone at $\eta = 2.3$.

Parameter	This Note	CAL-083
Fluka Sampling Term (% $\sqrt{E}$)	39.16 ± 1.04	48.6 ± 0.9
Fluka Constant Term (GeV)	1.27 ± 0.09	0.78 ± 0.08
GCALOR Sampling Term (% $\sqrt{E}$)	61.55 ± 1.75	n/a
GCALOR Constant Term (GeV)	2.73 ± 0.13	n/a

Table A.2: Sampling and constant terms measured by fitting the energy resolution of jets in the whole endcap calorimeter with a two term equation in this note and CAL-083.

$$\frac{\sigma}{E} = \frac{a}{\sqrt{E}} \oplus b$$

where a is the sampling term and b is the constant term. A summary of the whole calorimeter sampling and constant terms as compared to a previous analysis [8] is given in table A.2. Energy resolution curves for cones of size ΔR= 0.3, 0.5, and 0.7 are shown in figure A.6 for GEANT-FLUKA and GCALOR. The differences in energy resolution observed between jets centered at η = 2.1, 2.3, and 2.5 is negligible.

In order to test the effects of different particle energy cutoffs during the generation on the jet energy resolution, the 40 GeV E_T jets at η = 2.3 were regenerated using the energy threshold cuts suggested by the H1 collaboration [6]. These cuts lowered the γ threshold energy from 1 MeV to 0.2 MeV and the hadronic threshold from 10 MeV to 1 MeV. When the analysis method described in section A.4 was applied, very little difference in jet energy resolution was observed between the jets generated with the H1 cuts and the jets generated with the GEANT default cuts as can be seen in table A.3.

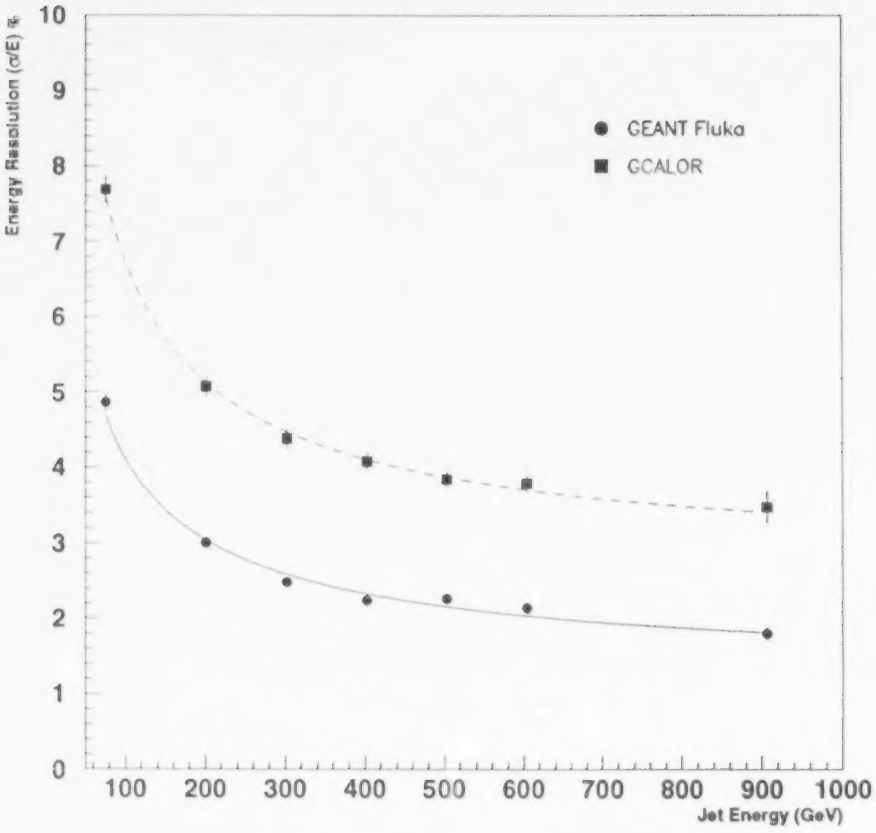

Figure A.5: The energy resolution of the entire endcap calorimeter between $\eta = 1.5$ and $\eta = 3.2$ for jets centred at $\eta = 2.3$. The circles are the results of using GEANT-FLUKA while the squares are the results of GCALOR.

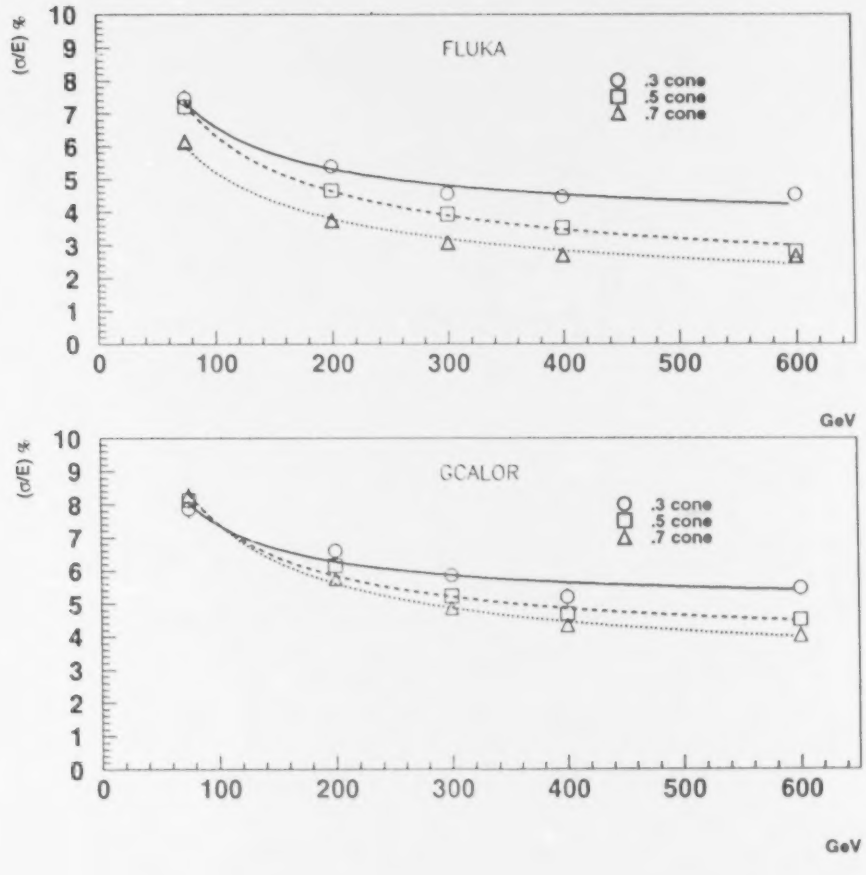

Figure A.6: Energy resolution curves for dijets reconstructed in three different cone sizes using GEANT-FLUKA (top) and GCALOR (bottom).

GEANT Cuts	FLUKA σ/E (%)	GCALOR σ/E (%)
GEANT Default	5.67 ± 0.18	9.63 ± 0.33
H1 Cuts	5.62 ± 0.19	9.96 ± 0.38

Table A.3: A comparison of the energy resolution results for 40 GeV E_T jets centered at $\eta = 2.3$ reconstructed in the whole endcap calorimeter volume for two different sets of GEANT cuts. The cuts are described in the text.

A.5.3 Behaviour of the Calibration Constants

The behaviour of the calibration constants as functions of energy and jet cone size is studied is this section. Figure A.7 compares the calibration constants obtained for the first electromagnetic calorimeter layer and the first hadronic calorimeter layer using GEANT-FLUKA and GCALOR. As was shown in the previous sections for the energy resolution of jets, a discrepency is observed between the two hadronic transport codes. The variation of the constants as a function of energy is small for both hadronic transport codes.

Figure A.8 displays the average calibration constant for both the electromagnetic and hadronic endcaps for different jet cone sizes. As the cone size increases, the average calibration constant in both the electromagnetic and hadronic calorimeters decreases due to the fact that less energy escapes from the larger cone.

Figure A.9 shows the spectrum of $E^{true} - E^{recon}$ for 80 GeV E_T jets for different cone sizes. For this plot, E^{true} was taken to be the energy at the vertex directed within the same cone size as was used in the reconstruction. Figure A.10 shows the spectra of the same jets but this time E^{true} is taken to be the energy at the vertex directed within a cone of size $\Delta R = 0.7$ for all reconstruction cone sizes. The change

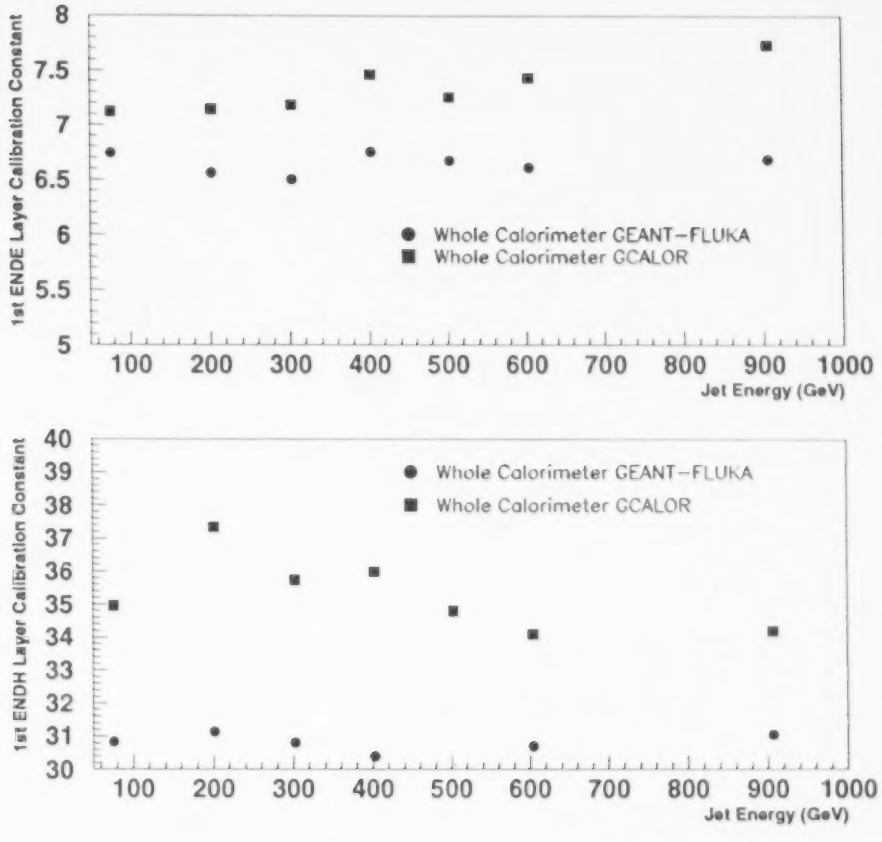

Figure A.7: The calibration constant obtained for the first electromagnetic endcap layer (top) and the first hadronic endcap layer (bottom) versus jet energy using the energy deposited in whole calorimeter during the calibration. The results using GEANT-FLUKA are shown by the circles while the results using GCALOR are denoted by the squares. In all cases, the error in the minimization as given by MINUIT is smaller than the data points.

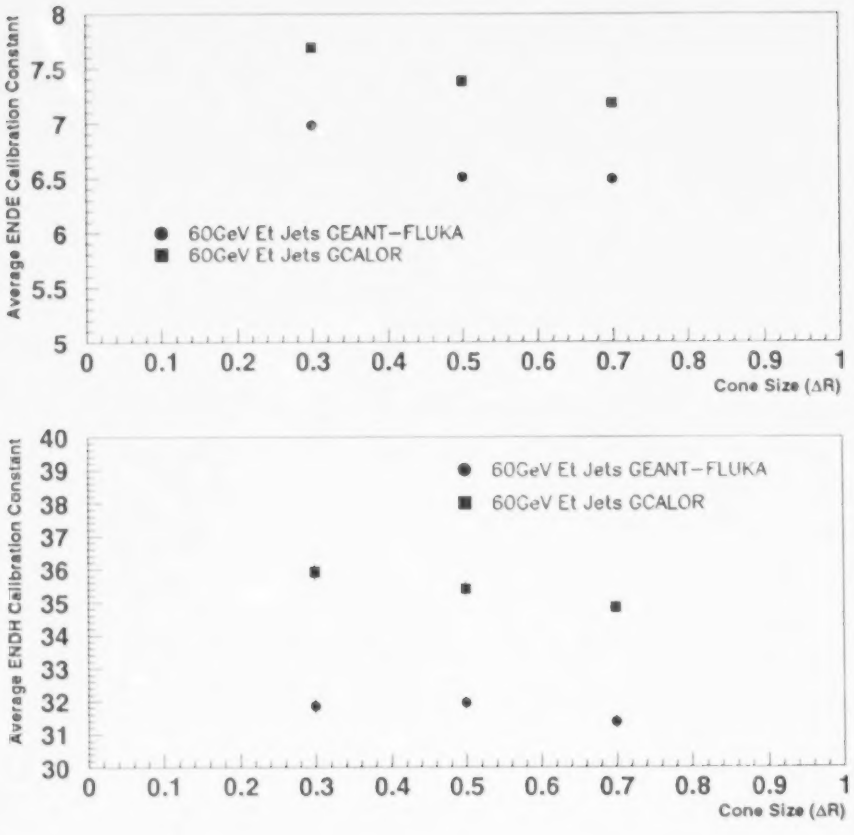

Figure A.8: The average electromagnetic calorimeter calibration constant (top) and average hadronic calorimeter calibration constant (bottom) obtained for three different jet cone sizes: ΔR= 0.3, 0.5, and 0.7. The energy deposited in the whole calorimeter was used in the calibration. The results for GEANT-FLUKA are shown by the circles and the results for GCALOR by the squares. Again, the MINUIT fitting error is smaller than the data points.

in the energy scale as a function of the reconstruction cone size is seen by comparing figures A.9 and A.10.

The amount of energy in the tails of $E^{true} - E^{recon}$ distributions when E^{true} is taken to be the energy at the vertex directed within a ΔR= 0.7 cone are shown in figure A.11. The fit used to isolate the tails was again an asymmetric gaussian from -1.5σ to $+3\sigma$. As a reference, a perfect gaussian distribution would have 6.7% of the energy outside of the fitted region.

A.5.4 Investigation of Hadronic Code Differences

In order to better understand the observed differences in energy resolution between GCALOR and GEANT-FLUKA, simulations using single particles were performed. Figure A.12 shows the energy resolution of pions for GEANT-FLUKA and GCALOR as well as for GHEISHA. By simulating electrons at the same energies as the pions, e/π ratios were obtained at several energies as shown in figure A.13. From the information in this figure, it is possible to extract the approximate values of e/h by using the following formula [9]:

$$\frac{e}{\pi} = \frac{e/h}{1 - < F_{em} > (1 - e/h)}$$

where

$$< F_{em} >= C \log(E)$$

This formula gives an approximate e/h ratio of 1.7 for GHEISHA, 1.35 for GCALOR and 1.1 for GEANT-FLUKA. As expected, the package that generates the lowest e/h ratio gives rise to the best constant term in the energy resolution measurement.

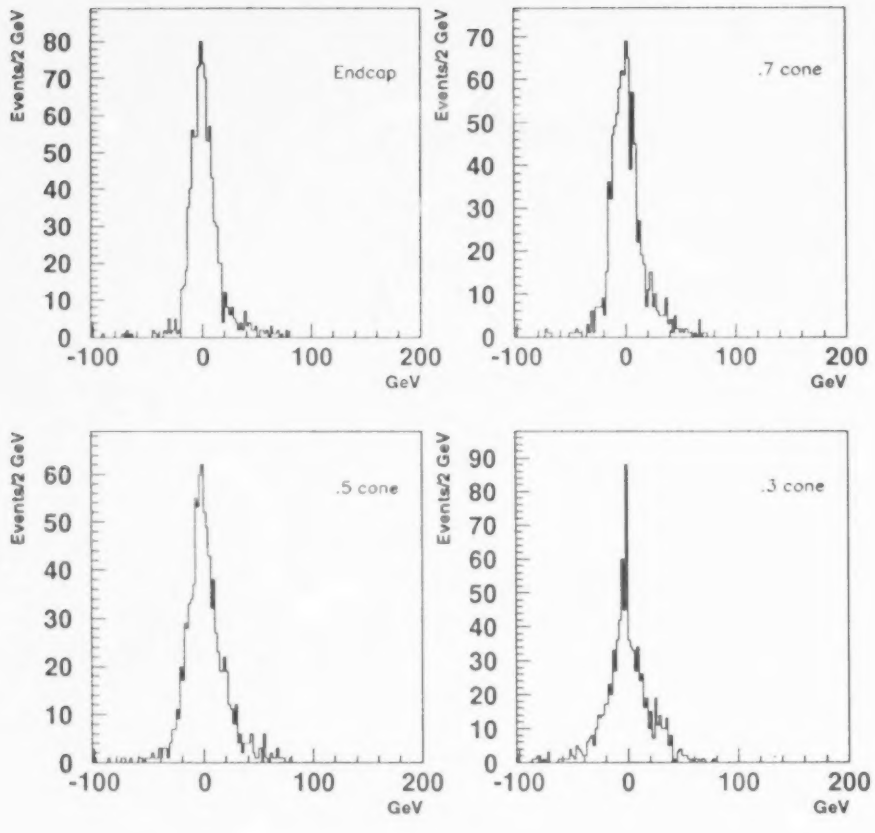

Figure A.9: Spectra of $E^{true} - E^{recon}$ for 80 GeV E_T jets using the whole endcap calorimeter and three different cone sizes. The value for E^{true} used was taken to be the vertex energy directed within the same cone size that was used in the reconstruction.

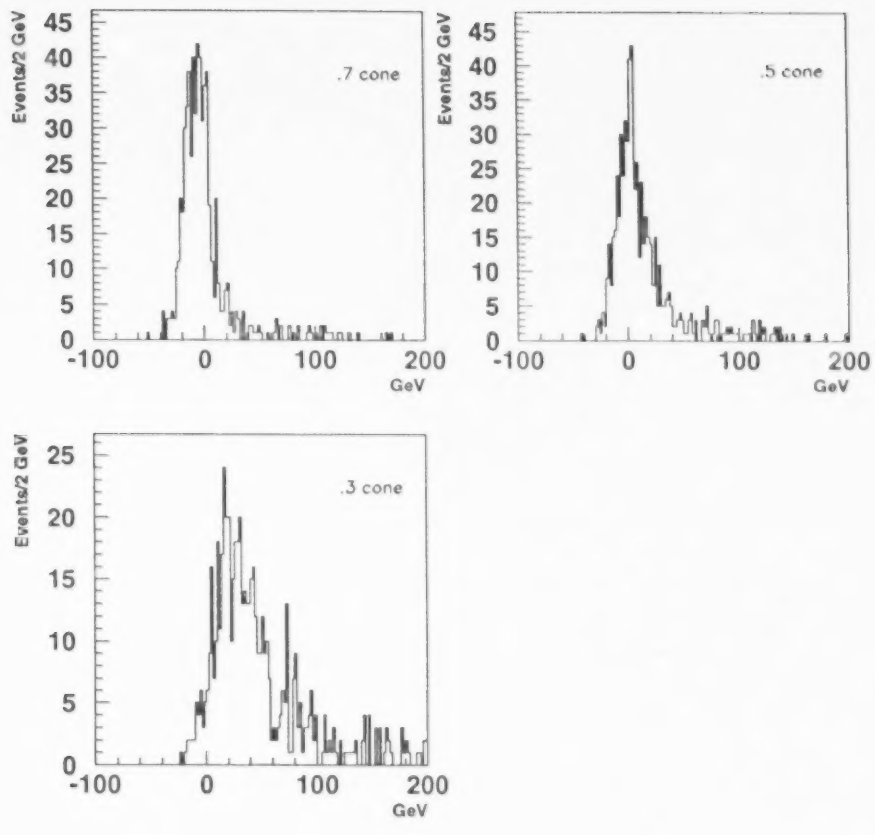

Figure A.10: Spectra of $E^{true} - E^{recon}$ for 80 GeV E_T jets using the whole endcap calorimeter and three different cone sizes. The value for E^{true} used was taken to be the vertex energy directed within a cone of size $\Delta R = 0.7$ for all reconstruction cone sizes.

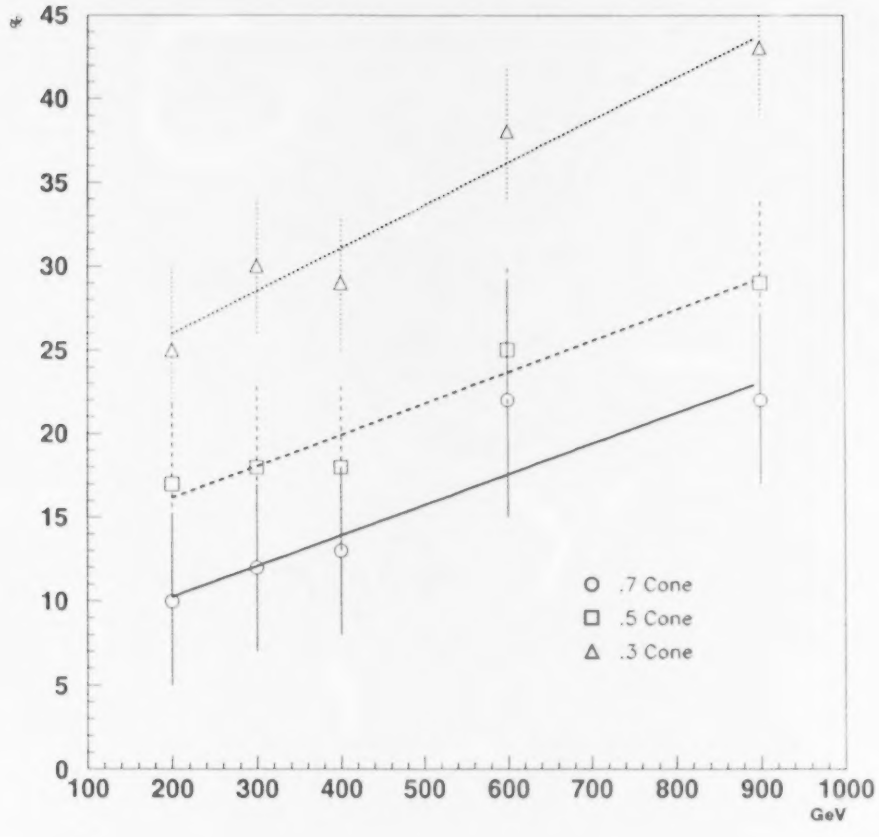

Figure A.11: Percentage of energy in the tails of the $E^{true} - E^{recon}$ distributions for five jet energies and three cone sizes when E^{true} is taken to be the energy at the vertex directed with a cone of size ΔR= 0.7. A perfect gaussian would have 6.7% of its area in the tails as defined in this plot.

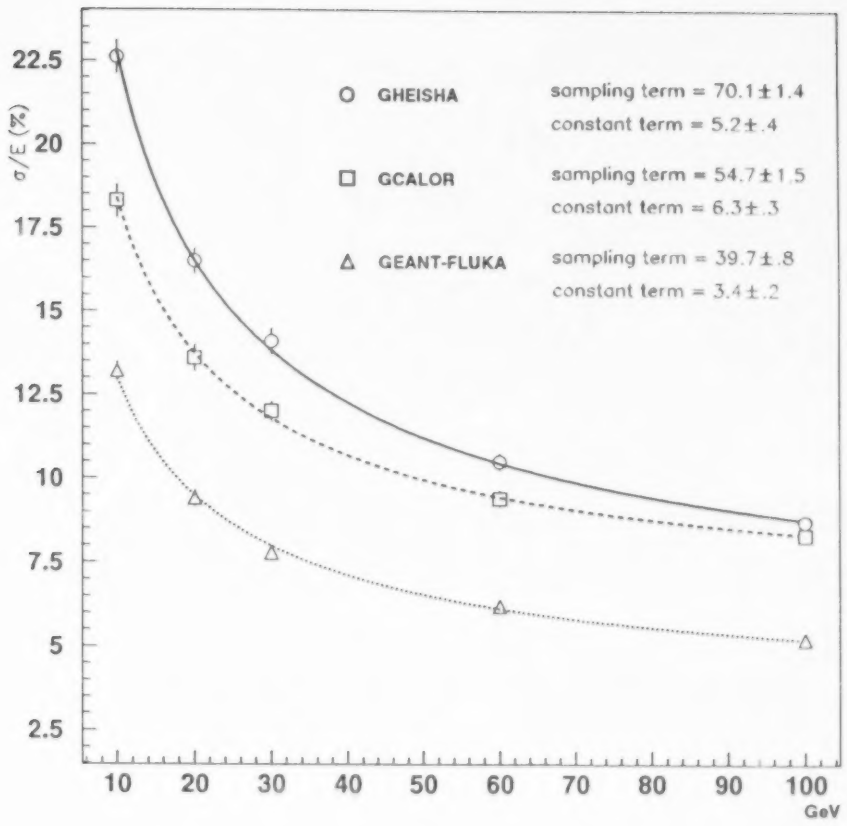

Figure A.12: Energy resolution for pions in the endcap calorimeter using Gheisha (circles), GCALOR (squares), and GEANT-FLUKA (triangles).

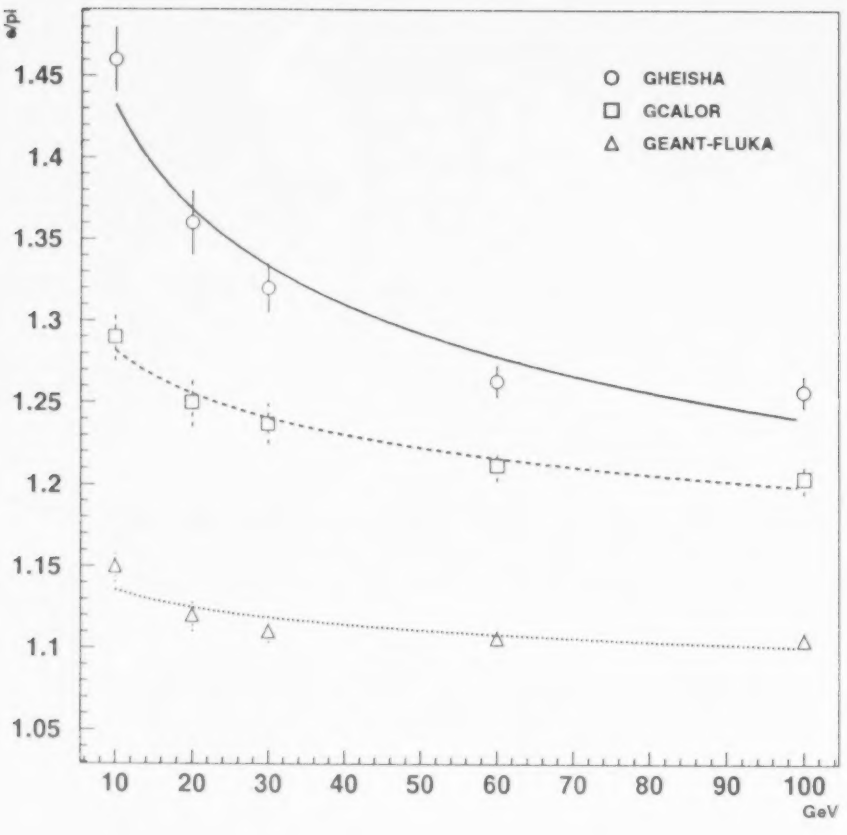

Figure A.13: e/π ratios for the endcap calorimeter using Gheisha (circles), GCALOR (squares), and GEANT-FLUKA (triangles).

A.6 Energy Resolution of Jets in the Presence of Pileup Noise

The effect of minimum bias pileup noise on the energy resolution of jets is considered in this section. For the shaping function used by the liquid argon calorimeters, it has been shown [5] that the rms of the pileup noise distribution does not vary with the square root of the area but scales as $A^{0.84}$. Furthermore, it was also shown that there are important longitudinal correlations in the energy deposited by minimum bias events in the calorimetry. A realistic simulation of the effect of pileup noise is therefore particularily important in determining the actual energy resolution of jets and obtaining the best parameters for jet finding algorithms. As was the case with different cone sizes, the jet energy scale will vary depending on the magnitude of the cell level E_T cuts used to remove the pileup noise. The optimization of such cuts must take into account the jet energy, the cone size and, of course, the operating luminosity.

The cell level E_T cuts used in this note were applied using two methods. The first method, referred to in this note as a *tower* cut, applied a cut to the sum of the energy deposited in all longitudinal samplings contained in a common $\Delta\eta \times \Delta\phi = 0.1 \times 0.1$ bin. The second method applied a separate E_T cut to each longitudinal sampling in a tower and is refered to as a *layer* cut. In the layer cut method, the results of [5] regarding the amount of pileup noise in each longitudinal sampling were used to scale the E_T cut applied to each longitudinal sample. For each 1 GeV E_T of integrated layer cut, the individual layer cuts are of magnitude 0.345 GeV, 0.210 GeV, 0.115 GeV, 0.175 GeV, 0.105 GeV, 0.035 GeV, and 0.015 GeV E_T respectively for each of the seven longitudinal layers of the endcap calorimeter.

A.6.1 Pileup Inclusion Method

For the liquid argon calorimeters, the reponse of the shaping electronics to a triangular input pulse lasts for over 500 ns which means that the energy deposition of over 20 bunchcrossings in the calorimetry must be considered for each signal event. For the purposes of this study, the shaping response time was taken to span 24 bunchcrossings. The pileup events used consisted of fully simulated minimum bias events convoluted with the bipolar shaping functions of both endcap calorimeters. Both high and low luminosity pileup events were added to the signal events in order to test the resolution degradation for different luminosity regimes. The high luminosity pileup was generated using a Poisson mean of 23 minimum bias events per bunch crossing (corresponding to a luminosity of 10^{34} cm^{-2} s^{-1} with a cross section of 70 mb) while the low luminosity pileup used a mean of 2.3 minimum bias events per bunch crossing (corresponding to a luminosity of 10^{33} cm^{-2} s^{-1}). A detailed study of pileup events in the ATLAS calorimetry may be found in [5]. The pileup study presented in this note used only GEANT-FLUKA for both signal and pileup generation.

The pileup noise energy was merged with the jet energy at the readout cell level. The aggregate merged energy of the jets plus pileup noise was then reconstructed using the calibration constants obtained without pileup by the method described in section A.4. The final energy resolution in the presence of pileup noise was obtained using the same asymmetrical gaussian fit as for the signal alone. Note that all results with pileup used GEANT-FLUKA for both the jet signal and the minimum bias production.

A.6.2 Energy Resolution in the Presence of Pileup Noise

The presence of minimum bias pileup noise will severely degrade the energy resolution of the calorimetry in ATLAS. In order to reduce the importance of this noise, cell level transverse energy cuts must be applied. The effect of the cell level cuts on the combined signal and pileup and on the pileup alone may be seen in figure A.14. The cut applied in this figure is a 2 GeV E_T integrated layer cut. The pileup after the cut is only shown if the combined energy of the signal plus pileup in that cell passed the cut. It can be seen that most of the pileup contribution is cut while the large core of signal energy in the combined plot remains intact.

Figure A.15 shows the energy resolution versus jet energy for signal alone and for signal plus high luminosity pileup using two different values of integrated layer cut in a ΔR=0.5 cone. As can be seen from the plot, the higher E_T cut makes a marked improvement in the energy resolution in the presence of pileup noise.

To obtain the optimal cuts and cones sizes needed to reduce the effects of pileup noise, the 40 and 120 GeV E_T jets centered at $\eta = 2.3$ were used. The 40 GeV E_T jets were reconstructed in ΔR= 0.3 and 0.5 cones and the 120 GeV E_T jets were reconstructed in ΔR= 0.5 and 0.7 cones. Figure A.16 shows the energy resolution for these jet energies and cone sizes versus the integrated E_T of layer cut (circles) or E_T of tower cut (squares) which was applied. The best resolution for both the layer cut and tower cut methods occurs for an E_T value of about 1.5 GeV for both jet energies.

For low luminosity pileup noise, the cuts applied to reduce the pileup contribution to the energy resolution need not be so severe. Figure A.17 shows the energy resolution of jets alone (circles) and in the presence of low luminosity pileup with a weak layer cut (triangles). As can be seen, the degradation of the resolution is not nearly as important as in the high luminosity case.

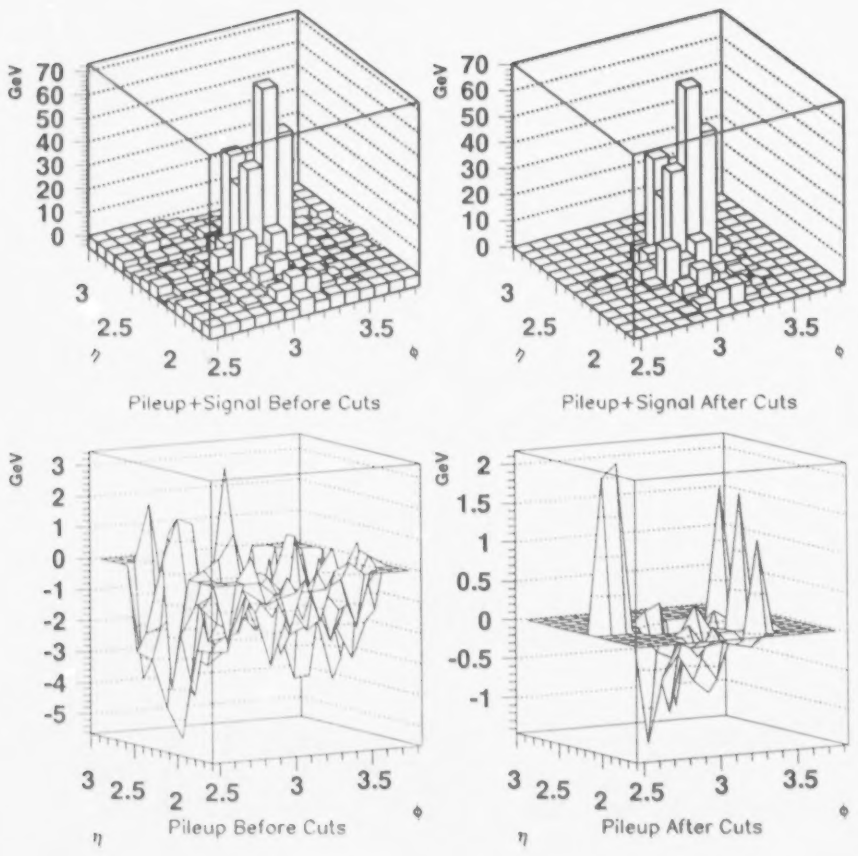

Figure A.14: The top row of plots shows the combined energy of 60 GeV E_T jets plus high luminosity pileup in each calorimeter tower before and after a 2 GeV E_T integrated layer cut. The bottom row shows the pileup per tower before the cut on the left and the pileup remaining in cells which passed the layer cut on the right.

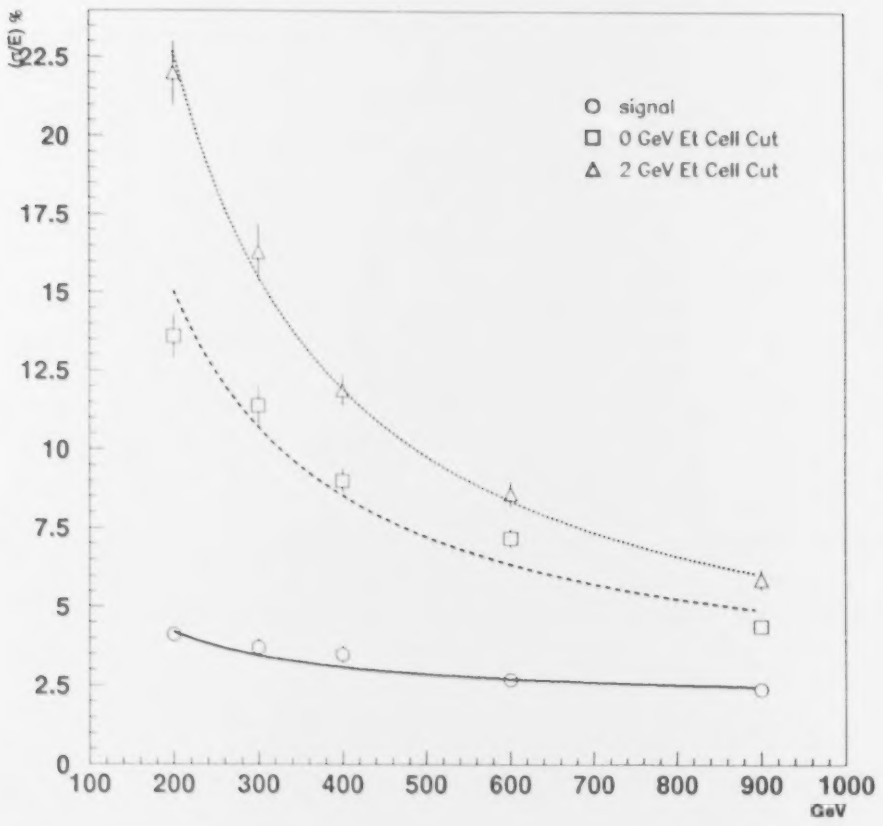

Figure A.15: Energy resolution of jets alone (circles) and jets plus high luminosity pileup using two different values of integrated layer cut (squares and triangles). The jets were reconstructed in a $\Delta R = 0.5$ cone.

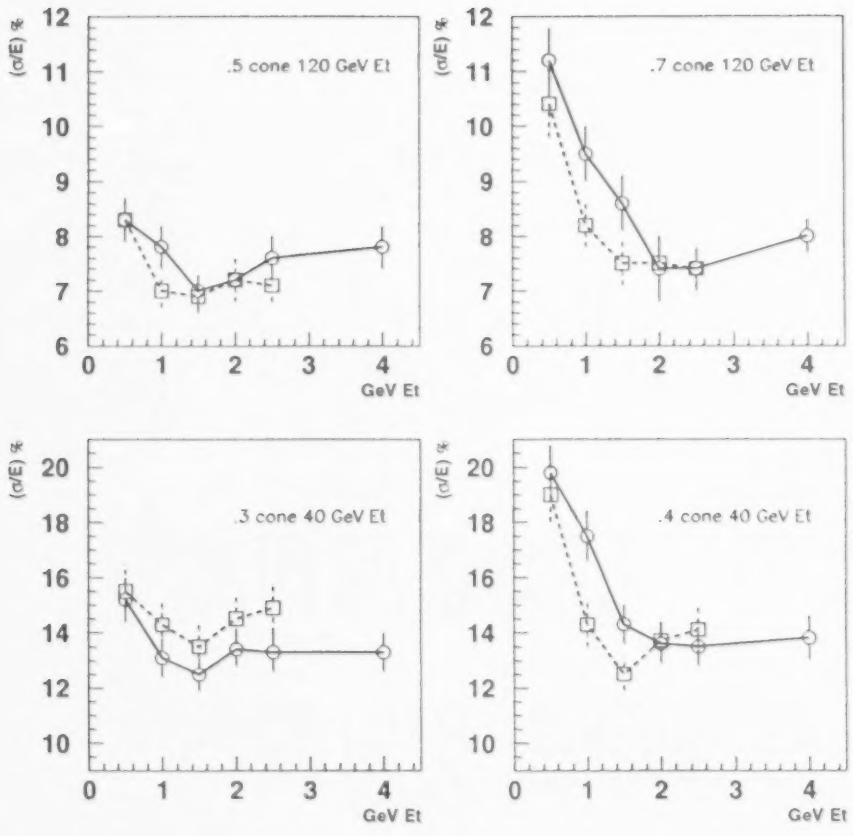

Figure A.16: The energy resolution of 40 GeV and 120 GeV E_{T} jets in various cone sizes versus the magnitude of integrated layer cut (circles) or tower cut (squares).

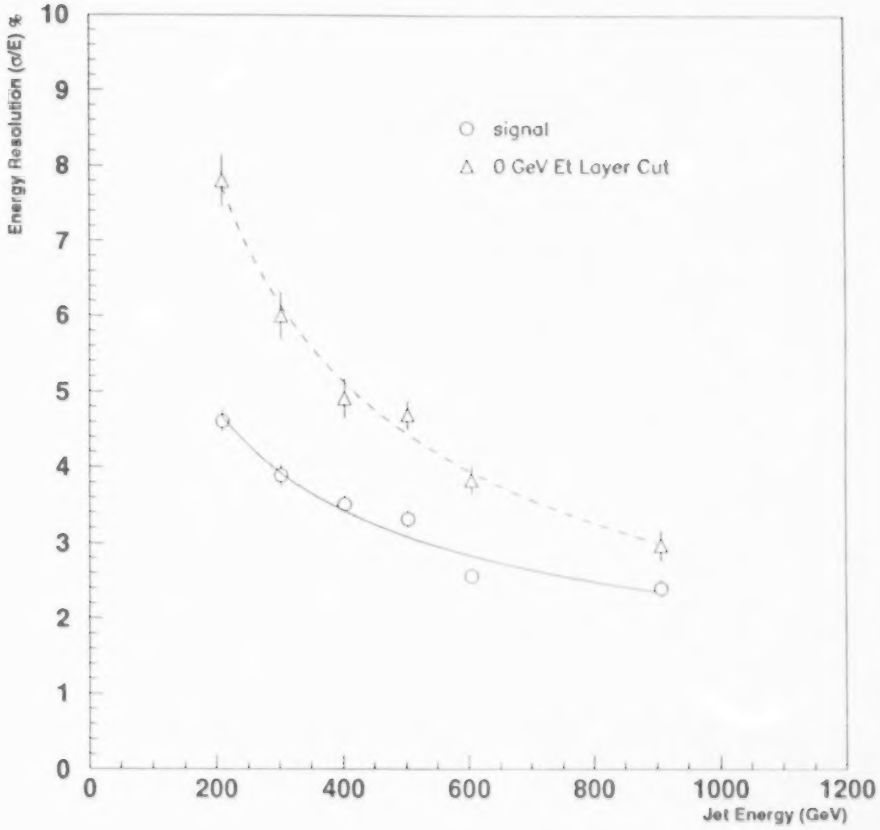

Figure A.17: Energy resolution of signal alone (circles) and signal plus low luminosity pileup using a 0 GeV E_T integrated layer cut (triangles). The jets were reconstructed in a ΔR= 0.5 cone.

In order to test the effect of a change in calorimeter granularity on the jet energy resolution, a new DICE geometry for the hadronic endcap with the granularity changed to $\Delta\eta \times \Delta\phi = 0.2 \times 0.2$ at $\eta > 2.4$ was used. This geometry was motivated by plans for the descoping of the hadronic endcap calorimeter. Jets were generated at $\eta = 2.5$ at transverse energies of 40, 60, 80, 100, 120, and 180 GeV E_T and at $\eta = 2.8$ at energies of 100, 200, 500, and 800 GeV. The method of reconstruction and calibration was identical to that of section A.4. High luminosity pileup was then added to the reconstructed jets in the same manner as in section A.6.1. A comparison of the resulting energy resolutions with pileup for the original and modified granularities is shown in figure A.18 for different cell level cuts. It can be seen that for a given value of cut, there is very little difference in energy resolution between the two different granularities.

A.6.3 Jet Scale in the Presence of Pileup Noise

To illustrate how the cuts affect the resolution and scale of the jet signal combined with pileup noise, the spectrum of $E^{true} - E^{recon}$ for 40 GeV E_T (201.5 GeV) jets combined with high luminosity pileup are shown for various tower cuts in figure A.19 for a ΔR=0.5 cone. The cuts not only affect the width of the distribution, but also the energy scale. The *energy scale factor* is defined as the nominal generation energy of the jet divided by the peak reconstructed energy.

Figure A.20 shows the evolution of the jet energy scale as a function of the jet energy in a ΔR= 0.5 cone for the signal alone, and for signal combined with high luminosity pileup for different integrated layer cuts. The jet energy scale obtained when pileup is added but no cut is applied is identical to the case without pileup since the bipolar shaping used in the liquid argon calorimeters gives an average pileup

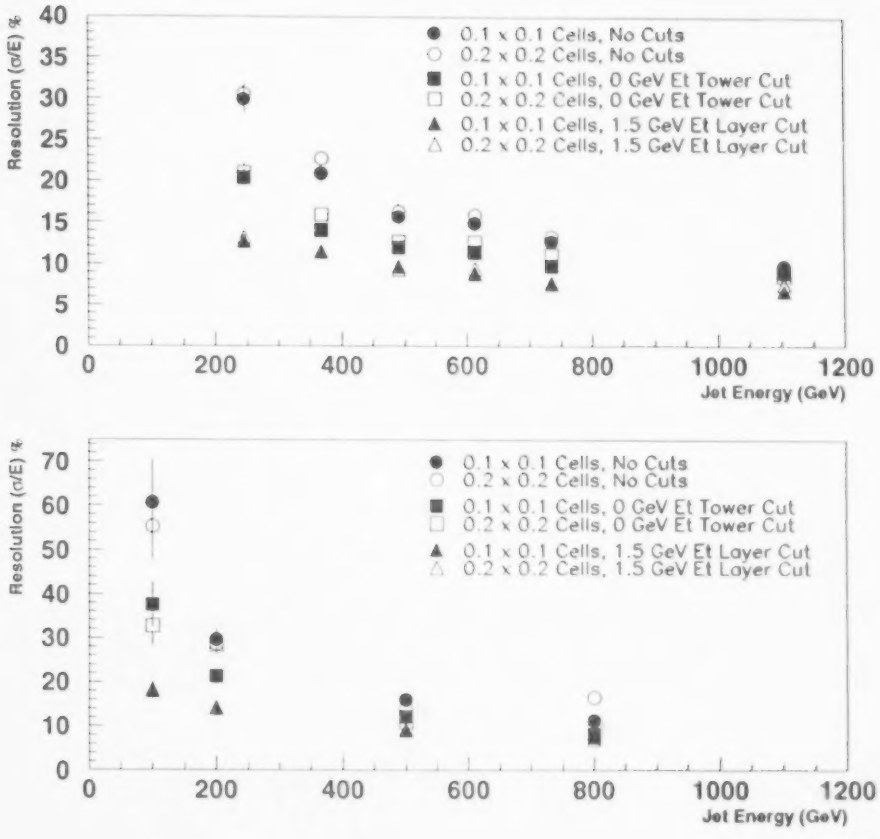
Resolution (σ/E) %
Jet Energy (GeV)
0.1 x 0.1 Cells, No Cuts
0.2 x 0.2 Cells, No Cuts
0.1 x 0.1 Cells, 0 GeV Et Tower Cut
0.2 x 0.2 Cells, 0 GeV Et Tower Cut
0.1 x 0.1 Cells, 1.5 GeV Et Layer Cut
0.2 x 0.2 Cells, 1.5 GeV Et Layer Cut
Resolution (σ/E) %
Jet Energy (GeV)
0.1 x 0.1 Cells, No Cuts
0.2 x 0.2 Cells, No Cuts
0.1 x 0.1 Cells, 0 GeV Et Tower Cut
0.2 x 0.2 Cells, 0 GeV Et Tower Cut
0.1 x 0.1 Cells, 1.5 GeV Et Layer Cut
0.2 x 0.2 Cells, 1.5 GeV Et Layer Cut

Figure A.18: Energy resolution for jets with high luminosity pileup reconstructed in a ΔR= 0.5 cone. Results for the nominal granularity (0.1×0.1) and a modified hadronic endcap granularity (0.2×0.2) are shown. Different tower cuts and integrated layer cuts are applied. The top plot shows the results for jets centered at $\eta = 2.5$ while the bottom plot shows the results for jets centered at $\eta = 2.8$.

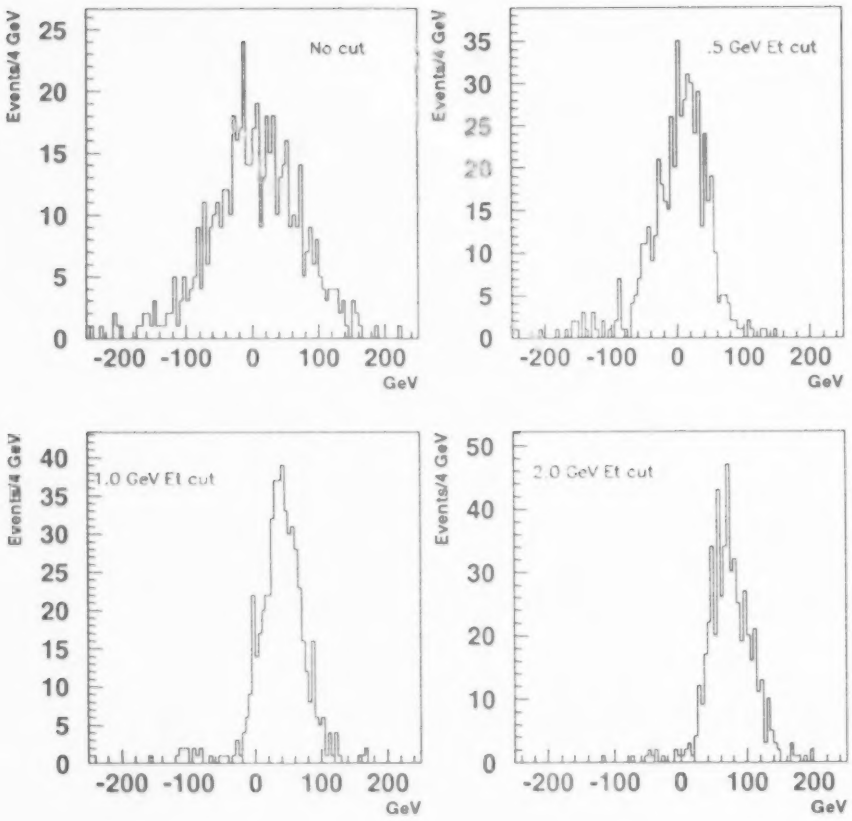

Figure A.19: Spectra of $E^{true} - E^{recon}$ in a ΔR= 0.5 cone for 40 GeV $E_{\rm T}$ (201.5 GeV) jets combined with high luminosity pileup. The spectra after several different values of transverse energy tower cuts are shown.

energy contribution of zero. When the 1 GeV E_T integrated layer cut shown in figure A.20 is applied, only cells with a mimimum value of "positive energy" are retained and hence the average pileup energy is no longer zero. This causes the reconstructed energy of the jets combined with pileup to go up and hence gives rise to a scale factor lower than one. As the magnitude of the cuts increase, however, more cells containing signal are removed and the reconstructed jet energy begins to go down again, eventually giving jet scale factors higher than one as can be seen for the 2 GeV E_T integrated layer cut in figure A.20.

The effect of different cone sizes on the jet scale when pileup noise is added was studied using 40 and 120 GeV E_T jets. The reconstruction cone sizes used were $\Delta R = 0.3$ and 0.5 for the 40 GeV E_T jets and $\Delta R = 0.5$ and 0.7 for the 120 GeV E_T jets. Figure A.21 shows the resulting jet scale factors versus the integrated E_T value of the layer cut. The jet energy scale shows less variation for smaller cones because the average energy of the cells within the small cones is higher than for the big cones. For an integrated layer cut of 4 GeV E_T (or 2 GeV E_T for the tower cut), the two scale factors for different cone sizes are the same since almost all the peripheral cells which are included in the larger cone but not in the smaller cone are removed by the cut.

A.7 Discussion

The results presented in this note used PYTHIA dijets exclusively. Some of the conclusions might have been different if other types of jets had been considered, especially concerning the jet cone size. In particular, the very high energy forward jets produced in qq $\rightarrow$qqH are very collimated and for this case the use of a smaller cone size than proved optimal in this note may be advisable given their relatively low

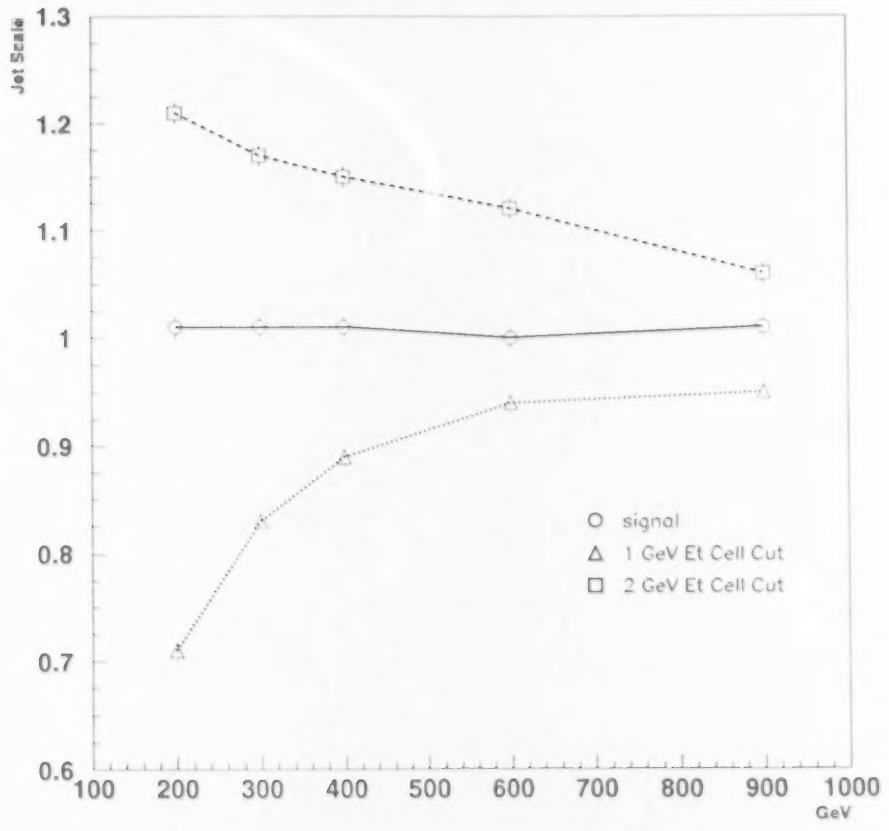

Figure A.20: The jet scale factor for the signal alone and for the signal plus high luminosity pileup with two different values of integrated layer cuts reconstructed in a $\Delta R = 0.5$ cone. The jet scale factor is defined as the nominal generation energy of the jets divided by their peak reconstructed energy.

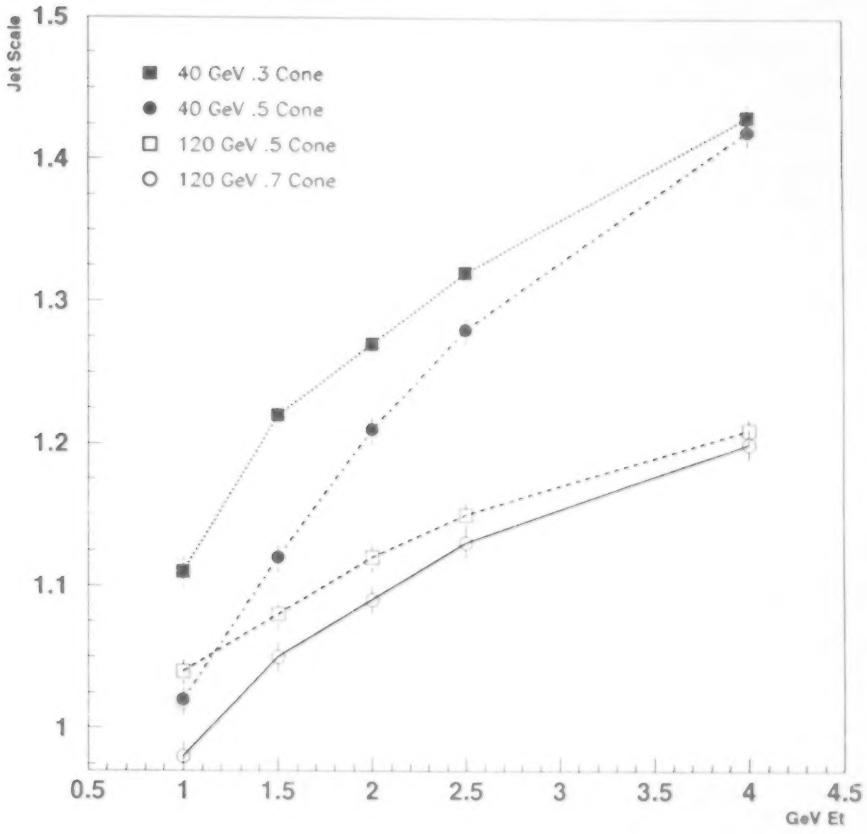

Figure A.21: The jet scale factor for the signal alone and for the signal plus high luminosity pileup for 40 and 120 GeV E_T jets using several cone sizes versus the integrated E_T value of the layer cut applied.

transverse energy.

For the calibration of DICE, earlier work by the authors [4] shows that single jets give nearly the same results as dijets as long as the cone size is very large. Therefore, because it is easier to define the nominal energy of single jets, they should be considered for calibration purposes.

Electronic noise was not included in this note since pileup noise dominates at high luminosity. However, this is not the case for low luminosity so the results given here for the latter regime are optimistic.

The jets studied in this note were directed far away from the η=1.5 crack and the η=3.2 crack. Clearly, the energy resolution will be lower in those regions and although work has been done in these areas before, few if any of the effects studied in this note were included.

An important deterioration of the jet energy resolution due to pileup noise has been observed at high luminosity. Here, to reduce the influence of pileup, smaller jet cones and strong cell E_T cuts were used. Other strategies to recover some of the lost resolution might come from the use of zero supression or optimal filtering [10] in hardware and more sophisticated jet algorithms in software.

The deterioration of the energy resolution due to pileup noise must be taken into account when performing particle level simulations. Also, the choice of a cone size for jet reconstruction must to be made by considering both the cell cuts that will be needed to obtain an optimal energy resolution and the proportion of energy in the tails of the reconstructed energy distributions for that cone size.

A.8 Conclusions

In this note, an effort was made to obtain a more realistic estimate of the jet energy resolution of the endcap calorimeters through studying detector effects, estimating the effect of pileup noise, and investigating methods of dealing with the associated loss of resolution.

First, the effect of the material in front of the calorimeter and the fluctuations in the jet event shape were studied. It was shown that the parameterization of the calorimeter resolution for jets receives contributions from both of these effects, especially jet to jet fluctuations which are purely physical and not of instrumental origin.

Second, important differences observed between GCALOR and GEANT-FLUKA were measured for both single particles and jets. The issue of which package to use for the hadronic endcap must be resolved with the analysis of test beam data which should be available at the end of 1996.

Third, an important deterioration of the energy resolution was observed when high luminosity pileup was added to the jets. The use of cell E_T cuts was found to improve the energy resolution. The use of longitudinally changing layer cuts did not appear to reduce pileup noise any better than the more simple tower cuts. This could be due to the existence of longitudinal correlations in the pileup noise as reported in [5]. Finally, the jet energy scale * in the presence of pileup noise was found to depend on reconstruction cone size, the magnitude of the cell cut, and the jet energy.

Future studies using the new DICE geometry must address the issue of providing accurate energy resolution smearing factors for use in particle level and fast

*The jet energy scale is defined as the nominal generation energy of the jets divided by their peak reconstructed energy.

simulation studies. The results of this note indicate that important contributions to these smearing factors come from the presence of pileup noise and fluctuations in the particle multiplicity and angular scope of the jets.

Acknowledgements

The authors would like to thank:

- G. Azuelos for his generous help in reading and commenting on this note.
- B. Lorazo for his authorship of the detailed hadronic endcap geometry used in this work.
- M. Lefebvre and J. Pinfold for their assistance and useful comments.

Bibliography

[1] ATLAS Collaboration, ATLAS Technical Proposal, CERN/LHCC/94-43 (1994).

[2] A. Artamonov, ATLAS Internal Note CAL-NO-065 (1994).

[3] L. Cozzi and L. Perini, ATLAS Internal Note CAL-NO-026 (1993).

[4] R.A. Davis and P. Savard, ATLAS Combined Calorimetry Meeting Transparency Number 7, 1994.

[5] R.A. Davis and P. Savard, ATLAS Internal Note CAL-NO-084 (1996).

[6] H1 Calorimeter Group, DESY 93-047 (1993).

[7] A.E. Kiryunin, ATLAS Internal Note CAL-NO-063 (1994).

[8] A.E. Kiryunin, ATLAS Internal Note CAL-NO-083 (1996).

[9] R. Wigmans, Nuclear Instruments and Methods **A265** (1988) 273.

[10] I. Wingerter-Seez, ATLAS Internal Note LARG-NO-19.